Stability and Power Coupling in Dynamic Screw Pinch Plasmas

by

Paul C. Campbell

A dissertation submitted in partial fulfillment
of the requirements for the degree of
Doctor of Philosophy
(Nuclear Engineering and Radiological Sciences)
in the University of Michigan
2020

Doctoral Committee:

Associate Professor Ryan McBride, Chair
Professor Ronald Gilgenbach
Associate Research Scientist Nicholas Jordan
Associate Professor Carolyn Kuranz
Professor Y.Y. Lau
Assistant Professor Louise Willingale

Paul C. Campbell

pccamp@umich.edu

ORCID iD: 0000-0002-6457-2177

Acknowledgments

This work was supported by the National Science Foundation under Grant No. PHY-1705418 of the NSF-DOE Partnership in Basic Plasma Science and Engineering. Facility support for COBRA was provided by the NNSA Stewardship Sciences Academic Programs under DOE Cooperative Agreement DE-NA-0003764. Sandia National Laboratories is a multi-mission laboratory managed and operated by National Technology and Engineering Solutions of Sandia, LLC., a wholly owned subsidiary of Honeywell International, Inc., for the U.S. Department of Energy's National Nuclear Security Administration under contract DE-NA-0003525..

TABLE OF CONTENTS

LIST OF FIGURES

FIGURE

LIST OF TABLES

TABLE

LIST OF APPENDICES

ABSTRACT

Fast z-pinches are formed when large axial currents run through cylindrical metal shells, or liners, to produce a Lorentz force that implodes the system. This implosion process is susceptible to magnetohydrodynamic instabilities, such as the magneto-Rayleigh-Taylor instability (MRTI). These instabilities are undesirable since many experiments rely on a sufficiently symmetric implosion. The study of MRTI is of particular relevance to magnetized fusion concepts like magnetized liner inertial fusion (MagLIF), which are degraded by this instability.

To reduce MRTI growth in solid-metal liner implosions, the use of a dynamic screw pinch (DSP) has been proposed [P. F. Schmit *et al.*, Phys. Rev. Lett. **117**, 205001 (2016)]. In a DSP configuration, a helical return-current structure surrounds the liner, resulting in a helical magnetic field that drives the implosion. In this dissertation, the first experimental tests of a solid-metal liner implosion driven by a DSP are presented [P. C. Campbell *et al.*, Phys. Rev. Lett. **125**, 035001 (2020)]. Using the 1-MA, 100–200-ns COBRA pulsed-power driver, three DSP cases were tested (with peak axial magnetic fields of 2 T, 14 T, and 20 T) along with a standard z-pinch (SZP) case (with a straight return-current structure and thus zero axial field).

These experiments demonstrated enhanced stability in thin-foil liner implosions. When compared to theory [A.L. Velikovich *et al.*, Phys. Plasmas **22**, 122711 (2015)], these results agree reasonably well. The strongest DSP case tested showed a factor of three reduction in instability amplitude at stagnation. Specifically, at a convergence ratio of 2, the MRTI amplitudes for the SZP case and for the 14-T and 20-T DSP cases were, respectively, 1.1 ± 0.3 mm, 0.7 ± 0.2 mm, and 0.3 ± 0.1 mm. While the convergence ratio of the experiments was low, relative to other imploding liner experiments, the trends in the data were clear; when the DSP generates stronger axial magnetic fields, the instability amplitude decreases.

Measurements using micro B-dot probes showed that the return current structures in the DSP cases generated axial magnetic field values in line with the values predicted by electromagnetic simulations. Measurements taken inside the imploding liners showed a significant amount of flux injection and subsequent flux compression.

Throughout the short-pulse experiments on COBRA, the 14-T and 20-T DSP cases

stagnated 10–40 ns earlier than the SZP cases, which is most likely due to the added magnetic pressure from the axial field that is present in the DSP case.

The load current on COBRA was measured with a Rogowski coil in the power feed. After peak current, the Rogowski measurement would often terminate during the falling edge of the current pulse in the SZP experiments, while in the 14-T DSP experiments, it would often continue well after the current pulse had returned to zero. Preliminary particle-in-cell (PIC) simulations suggest that, after peak current, electrons sourced near the liner are directed down into the power feed towards the Rogowski coil in the SZP configuration, while simulations of the 14-T DSP configuration suggest these electrons are ejected radially outward through the gaps between the DSP return-current posts and thus away from the Rogowski coil. The lack of electron interaction with the Rogowski coil may explain why the load current measurements persist for longer in the DSP experiments. This observation could have important implications for power delivery in magnetically driven implosions in general.

CHAPTER 1

Introduction

1.1 A Brief Overview of Pulsed Power

Marx banks, or Marx generators, are electrical systems designed to generate high voltage pulses from from low voltage supplies. They were invented in the early 20th century by Erwin Otto Marx [9] and are still the primary driving device in many pulsed-power based experiments today. Marx-based pulsed power machines can be quite large in scale. For example, the world's largest pulsed power device, the 30-MA Z machine (see Fig. 1.1) at Sandia National Laboratories, is 33 meters in diameter [10, 11, 12]. It is made of of 36 Marx generators arranged in an outer ring connected to a central vacuum chamber via pulse compressing transmission lines. The pulse compression lines on Z shorten the rise time of the current pulse from approximately 2 µs at the output of the Marx generators to approximately 100 ns at the experimental load (or "target") placed in the center of the machine.

The energy stored by the Z machine is an astounding 23 MJ, when charged to ±90 kV. This can be calculated using $E = \frac{1}{2}CV^2$, where C is the capacitance of the pulsed power machine, and V is voltage the capacitors are charged to. Knowing the energy stored in a pulsed power system is great, but what then is the current (and voltage) that ends up getting sent to the experiment? How fast will that current rise, and how long will the current pulse be? To answer these and other questions about pulsed power machines, we will use a simple LC circuit model of a pulsed-power device [13], as seen in Fig. 1.2.

For this circuit, the time $t = 0$ corresponds to the start of current, when the switch closes. At times $t < 0$, the capacitor C is charged to a voltage V_0. At times $t > 0$, the capacitor can discharge into the inductor L. This system is a simple harmonic oscillator with a resonant frequency given by $\omega = 1/\sqrt{LC}$. This means that the current and voltage in the system will oscillate as $\sin(\omega t)$ and $\cos(\omega t)$. Just these two parameters, L and C, provide us with a key characteristic of our system, the rise time: $\tau = \pi/2\sqrt{LC}$. From the initial conditions $V = V_0 > 0$ and $I = I_0 = 0$, the equations $V = L\dot{I}$ and $I = -C\dot{V}$ can be solved and the peak current $I_{peak} = V_0\sqrt{C/L}$ can be obtained. Since this circuit model has no dissipating effects,

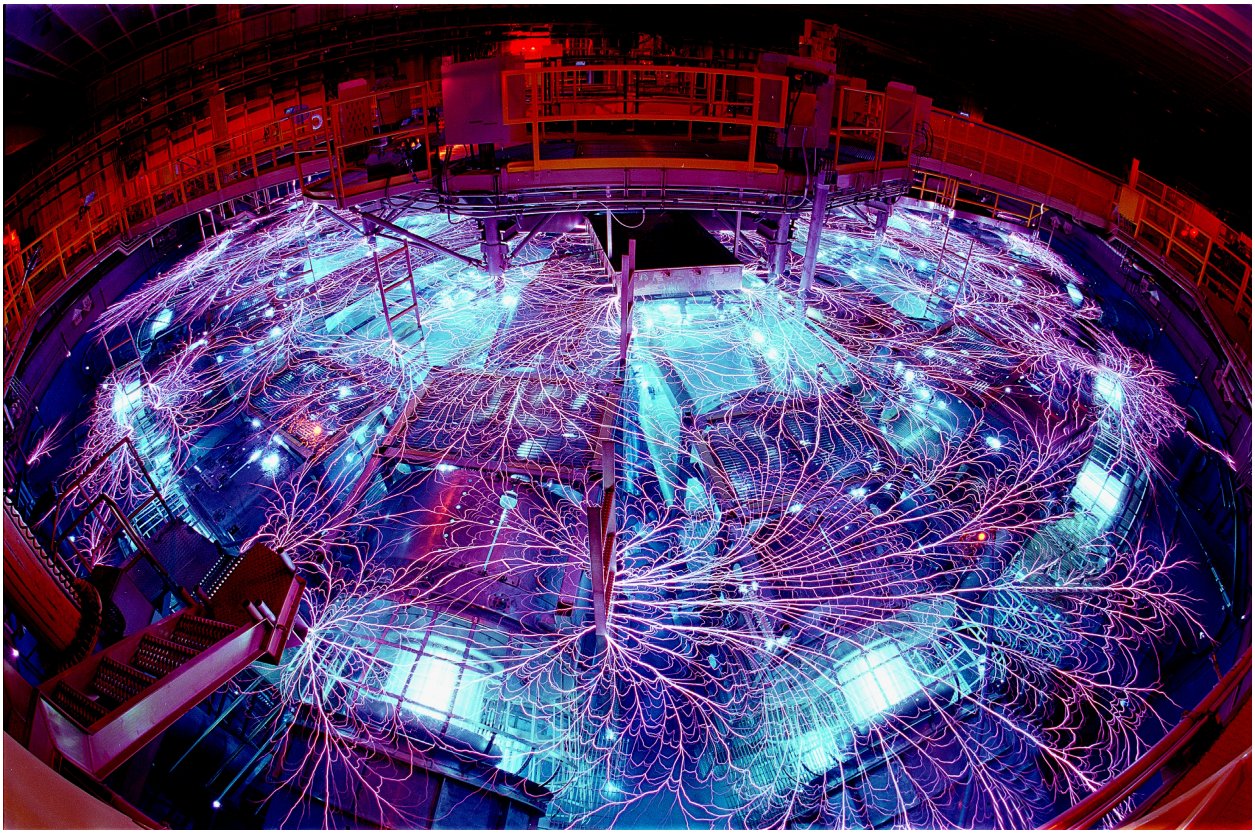

Figure 1.1: A picture of Sandia's Z machine firing. Photo by Randy Montoya and may be found at `https://www.flickr.com/photos/sandialabs/6288961527`.

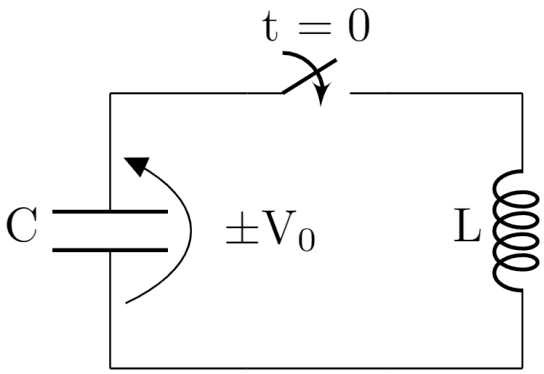

Figure 1.2: A simple circuit model of a pulsed power machine, with capacitance C and inductance L, where neither quantity varies in time. At time $t = 0$, the switch closes, and the capacitor begins to discharge into the circuit. This simple model does not account for dissipative effects like resistances or time-varying inductances, so the current and voltage will oscillate forever.

the voltage and current to the circuit equations would oscillate forever. A more complete circuit model and discussion of the machine used in the experiments of this dissertation is given in Chapter 3 and Appendix B.

This circuit model can be applied to any pulsed power machine, not just Marx generators. In general, all pulsed power machines will charge many high voltage capacitors and discharge them through some load. In z-pinch driver design is maximizing current delivery while minimizing rise times. Marx generators are a mature, well-studied technology. More recently, linear transformer drivers (LTDs) have been developed as a potentially more compact alternative. LTD's were designed at the Institute of High Current Electronics (IHCE) in Tomsk, Russia during the 1990's [14, 15]. In comparison to the traditional Marx bank, LTDs are smaller, but can still be quite large, with individual cavities ranging from 2 to 3 meters in diameter [16]. In addition to their potentially smaller footprint, LTDs often do not require the pulse compression stages that Marx generators often do, since LTDs are capable of providing rise times on the order of 100 ns directly from the prime power capacitors, when driving reasonably matched load impedances (i.e., loads with low inductances). The trade-off, however, is that a low-impedance, single-stage LTD system (consisting of a single LTD cavity) is not as "stiff" as a traditional Marx-based system that consists of several, physically larger, high-impedance, multi-stage Marx generators. By "stiff" we mean that current delivery is less affected by the experiment's load impedance. This means that on its own, a single LTD stage can drive a smaller range of load impedances, relative to a comparable Marx-based system.

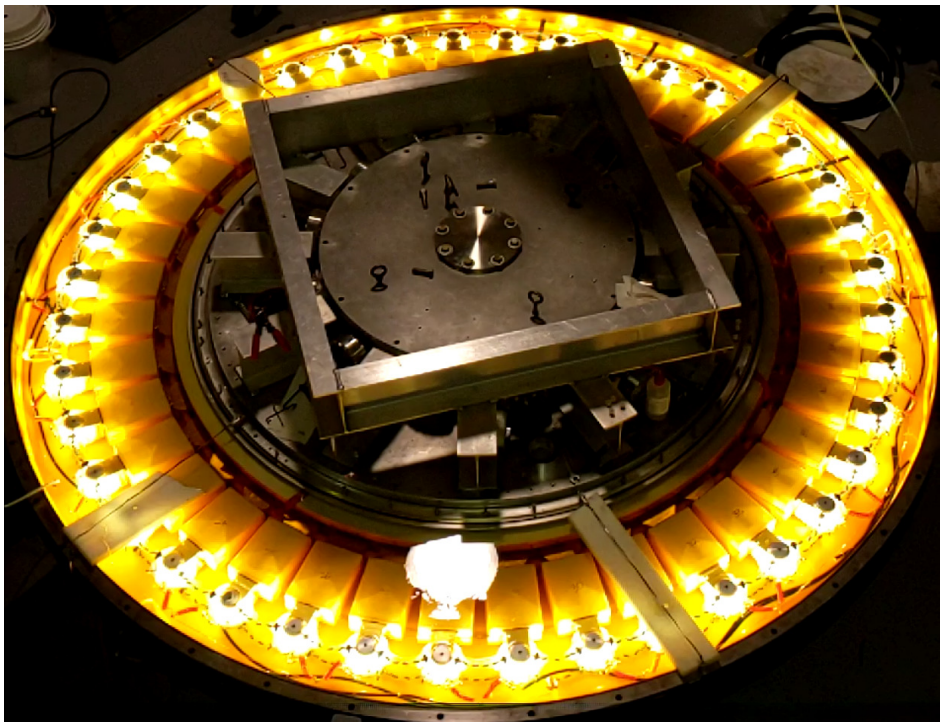

Figure 1.3: A picture of the MAIZE LTD firing. MAIZE is a single-stage, 3-meter-diameter LTD stage. Photo by Trevor Johannes Smith.

1.2 Why Use Pulsed Power?

Both Marx-based and LTD-based drivers can be quite large in scale. They store energy by slowly charging capacitors, often separated by meters from the experimental load hardware. After the capacitors are fully charged, high-power switches are triggered to send a large electromagnetic power pulse towards the experiment at the center of the machine. Often, the experimental target is a cylinder with both height and radius dimensions on the order of 1 cm. On the Z facility, several MJ are delivered to the target in approximately 100 ns, resulting in a peak electrical power of approximately 80 TW—this is momentarily greater than the average generating capacity of the entire world. Herein lies the allure of pulsed power.

Pulsed-power devices have played, and continue to play, a key role in high energy density physics (HEDP). This subfield of physics is the study of matter and radiation in extreme conditions, or pressures in excess of 1 Mbar. HEDP is a very multidisciplinary field that encompasses interests such as astrophysical phenomena [17, 18], planetary formation [19], dynamic material properties [20, 21], radiation generation [22, 23], and nuclear fusion [24, 25, 26, 27]. Oftentimes, one experimental platform is all that is needed to probe several of these areas. For example, conditions that are important to fusion experiments are also relevant to the physics of star formation and death. With so many avenues of study, and

new experimental capabilities becoming available, it is an exciting time to be involved with pulsed-power-driven HEDP research.

Lasers are another popular choice for driving HEDP experiments [28]. There are some trade offs between laser-driven and pulsed-power-driven HEDP platforms though. Laser pulse durations (usually only a few ns at most) are often quite short compared to pulsed power rise times ($\sim$ 100 ns). As a consequence, laser-based HEDP experiments can usually only be driven for a short period of time (a few nanoseconds at most). Additionally, generating laser photons and coupling these laser photons to an HEDP experiment is often much less efficient energy-wise than the direct coupling of electrical energy in a comparable pulsed-power-driven experiment. The choice of driver, whether laser or pulsed power, comes down to how hard a material needs to be driven, how long the material needs to be driven, how large of a material needs to be driven, and what the material's properties are (e.g. density, geometry, diagnostic access, pulse-shaping precision). Making this decision requires knowledge not only of the experimental parameters, but also knowledge of the machine parameters. The two are inextricably linked, in both the pulsed-power and laser case. A mismatch between the driver and the experimental objectives is an easy path to poor results that can be avoided by taking into account the above considerations. In Chapter 3 we will discuss how the experimental hardware was manufactured and designed in order to best match the pulsed power machine used.

1.3 Fusion Research

We now switch our focus from the many applications of pulsed power to one in particular, inertial confinement fusion (ICF). Fusion research today is in three primary areas, magnetic confinement fusion (MCF), laser driven ICF experiments, and pulsed power driven ICF experiments.

One of the main pulsed power driven ICF concepts being pursued on the Z facility at Sandia National Laboratories is the Magnetized Liner Inertial Fusion (MagLIF) concept [24]. MagLIF reaches thermonuclear fusion conditions by using using an approximately 20-MA current pulse from the Z facility to drive the implosion of a cylindrical metal shell, or liner, which compresses preheated and premagnetized fusion fuel.

MagLIF employs several tricks in order to relax the convergence requirements needed to achieve fusion. Since the concept relies on a relatively slowly imploding cylinder, rather than a faster imploding sphere, these tricks will be necessary to compete with the laser driven spherically converging concepts of direct and indirect laser driven fusion.

Indirect drive, laser driven implosions at the National Ignition Facility (NIF) reach

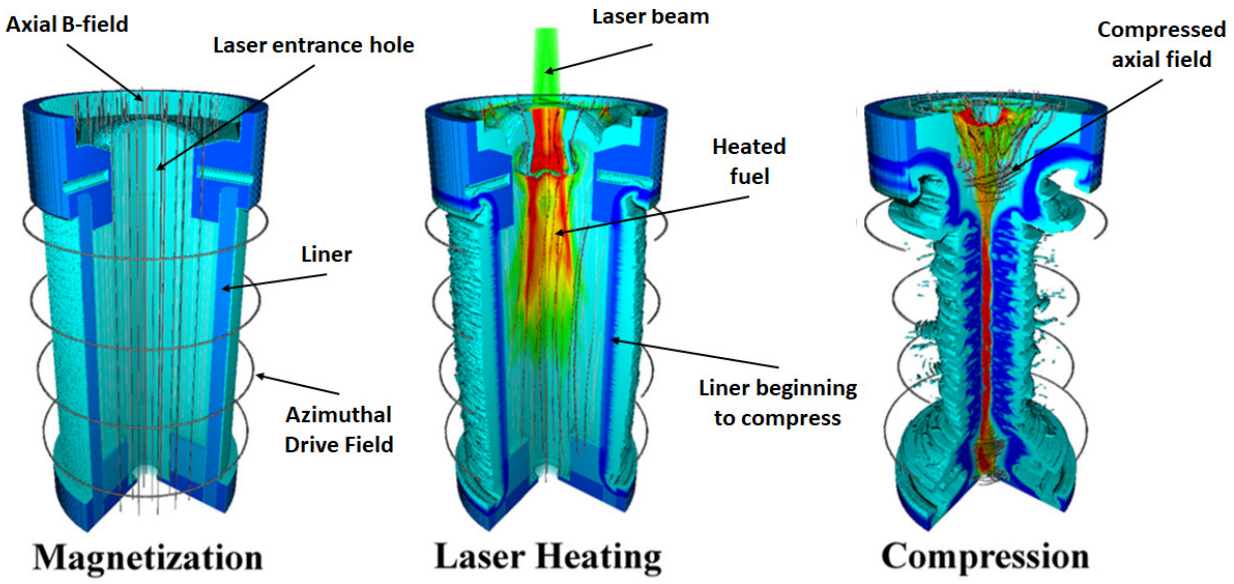

Figure 1.4: An illustration of the three stages of MagLIF. First is the magnetization stage where an external axial magnetic field is applied to the fusion fuel filled cylindrical target. Next is the laser heating stage where the fuel is heated by a laser. Last is the compression stage where an axial current creates a Lorentz force that is used to implode the cylindrical target. Figure adapted from M.R. Gomez et al. [1].

velocities of ∼400 km/s while MagLIF implosions reach velocities of 70–150 km/s [29]. These fast implosion velocities are supersonic in the fuel which generate shocks that heat the fuel to fusion temperatures when further compressed. Since MagLIF implosions have subsonic velocities preheating the fuel is necessary. The time scale of the MagLIF experiment is also longer, so the preheated fuel will need to be kept hot for the longer implosion time and will need to be kept insulated from the cold liner. In order to work with these constraints MagLIF employs three stages.

The first of MagLIF's stages is the pre-magnetization stage, where an axial magnetic field, B_z, is applied to the load region approximately 3 ms before the Z machine's 100-ns current pulse is driven through the liner. Applying the B_z field early allows the field lines the time needed to fully diffuse through the liner and into the fuel prior to the implosion. The magnetic field helps to inhibit radial energy losses by reducing the thermal conduction from the hot fuel to the cold liner wall. This inhibition occurs throughout the implosion stage, as both the fuel and the B_z field are compressed by the imploding liner. At stagnation, the flux compressed B_z field also helps to heat the fuel by trapping charged fusion products in the fuel—i.e., these trapped fusion products can deposit the kinetic energy they obtained from the fusion reaction that generated them back into the fuel.

Next is the laser preheating stage. As the name suggests the fuel is preheated by a

multi-kJ laser pulse. The fuel needs to be preheated since the compression on its own will not heat the fuel to the fusion relevant temperatures desired. Cylindrical geometry, along with the slower implosion velocity, works against us in this case, as seen by the convergence ratio for an adiabatically compressed target, $CR = (T_{ig}/T_0)^{3/2g}$, where g is a geometry dependent parameter that is 2 for a cylindrical convergence geometry and 3 for a spherical convergence geometry [24]. In order to reach the ignition temperature, T_{ig}, from the fuel's initial temperature, T_0, a material needs to be compressed more in the cylindrical case. Preheating helps relax this constraint to more modest convergence ratios.

During the compression stage, the machine current ramps up and the resulting Lorentz force compresses the liner. The compression stage is a violent dynamic process, where the liner is susceptible to a whole host of instabilities that work to perturb the fusion fuel contained inside the liner and decrease the number of fusion reactions occurring in the fuel. The focus of this dissertation will be on one class of these instabilities in particular, Rayleigh Taylor instabilities, and a promising new method for controlling its growth, called the dynamic screw pinch. The theoretical framework necessary to discuss and interpret this concept and its results will be developed in Chapter 2. Experimental hardware and setup will be shown in Chapter 3. Results of experimental tests of this concept will be presented in Chapter 4. Finally, concluding remarks and ideas for future work are presented in Chapters 5 and 6.

CHAPTER 2

Cylindrical Liner Implosion Theory

In this Chapter, we will explore the theory of cylindrical implosions. We will start by introducing the z-pinch, a plasma confinement method. Next, we will discuss a class of instabilities known as Rayleigh-Taylor instabilities, which form when fluids of disparate densities are accelerated into one another. Dispersion relations for this class of instabilities, in the appropriate geometries, will be reviewed so that we can make some predictions about what to expect in our experiments. Finally, we will discuss the shortcoming of the models used and see if we can make some small improvements to them, to better predict experiment.

2.1 Z-Pinches

Z-pinches are a type of plasma confinement scheme, formed when electrical currents runs through electrically conducting materials, usually cylindrical in geometry [30, 31]. The "z", in z-pinch refers to the direction of the current flow, meaning this is an axial current flow that is typically aligned with the z-axis of a cylindrical coordinate system. The axially directed current I generates an azimuthal magnetic field $B_\theta = \mu_0 I/2\pi R$, where R is the liner radius, and μ_0 is the permeability of free space.

Referring to Fig. 3.5, the axial current density $\mathbf{J}$ and the azimuthal magnetic field $\mathbf{B}$ result in a radially inward Lorentz force $\mathbf{F} = \mathbf{J} \times \mathbf{B}$, where $\mathbf{F}$ is a force density (i.e., a force per unit volume). This compression can also be described by the increase in magnetic pressure, $P_{mag} = B^2/2\mu_0$.

Some of the configurations z-pinches can come in include gas puffs, wire arrays, and liners. Liners are solid cylindrical metal tubes, while wire arrays are a cylindrical arrangement of metal wires, and gas puffs are an annular puff of gas. Gas puffs and wire arrays are generally used as radiation sources; both produce x-rays, and gas puffs can produce neutrons, when a gas like deuterium is used. Liners are of particular interest due to the MagLIF ICF concept.

Z-pinch implosions are susceptible to a whole host of instabilities, such as the sausage instability ($m = 0$, where m is the azimuthal mode number), the kink instability ($m = 1$),

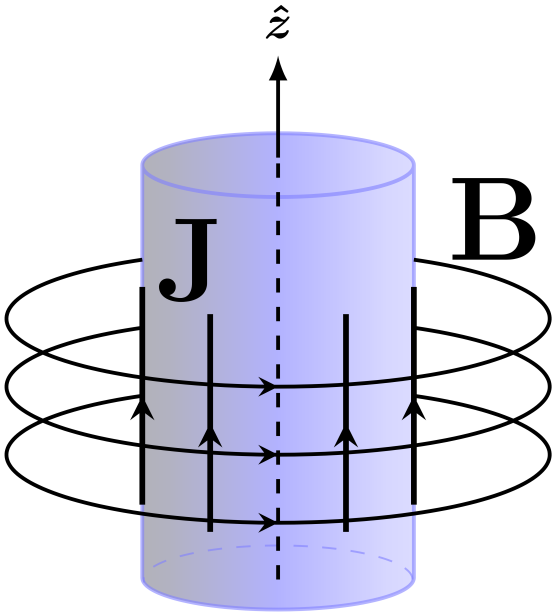

Figure 2.1: An illustration of a plasma column, in blue, with a current density **J** running through it and the associated magnetic field **B**.

$$\mathbf{F} = \mathbf{J} \times \mathbf{B}/V = -P_{mag} \cdot A_S = -P_{mag} \cdot 2\pi Rh$$

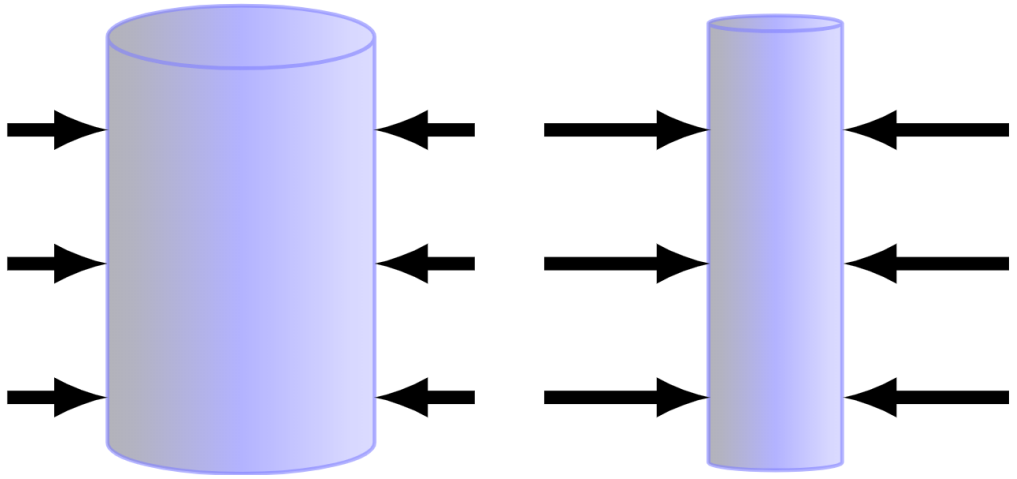

Figure 2.2: An illustration of a liner imploding radially inward due to the associated magnetic pressure (Lorentz force) that points inward. The liner's height, and surface area are given by h, and A_S respectively.

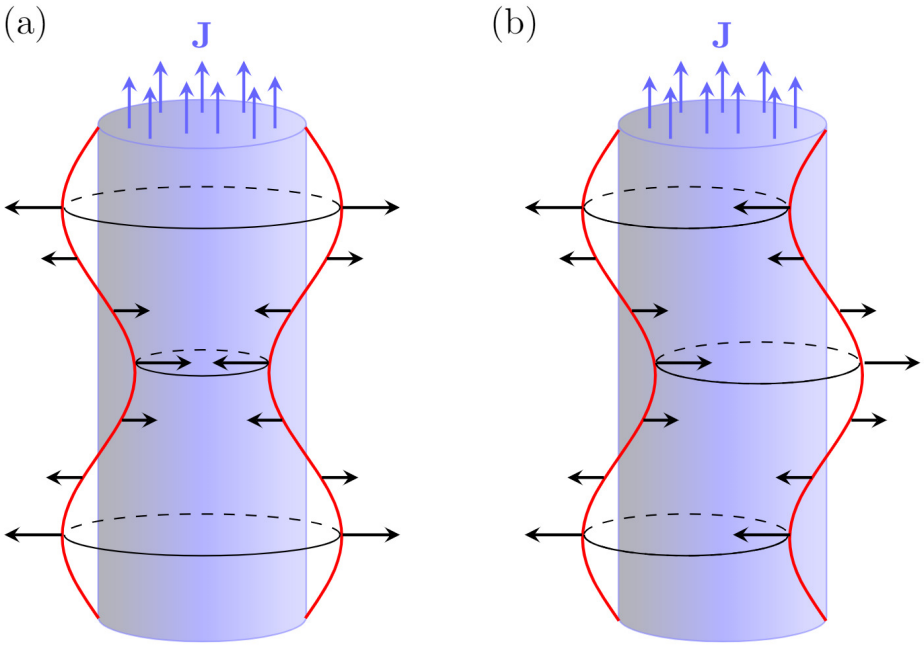

Figure 2.3: Illustrations of plasma columns going sausage mode ($m = 0$) unstable (a) and kink mode ($m = 1$) unstable (b). The blue shaded cylinders represent the initial plasma configurations. The blue arrows indicate that the plasma columns are current carrying. The red lines indicate how the liner will be perturbed in each case. The black arrows indicate the directions the perturbed surfaces will move.

higher-order helical instabilities in general ($m \geq 1$), and the magneto-Rayleigh-Taylor (MRT) instability (MRTI) [30]. A great deal of research, including this dissertation, has gone into stabilizing z-pinches [32, 33, 34, 35, 36, 37, 38].

An unstable equilibrium can exist in a z-pinch when the radial inward force, $\mathbf{J} \times \mathbf{B}$, balances the radial outward force, ∇p. This is also known as the Bennett relation and for a z-pinch at equilibrium [30, 31] reads:

$$\frac{d}{dr}\left(p + \frac{B_\theta^2}{2\mu_0}\right) + \frac{B_\theta^2}{\mu_0 r} = 0. \tag{2.1}$$

Note that there can be other forces in play due to effects like ram pressure, but for this simple picture, we will focus on just these two. This equilibrium is unstable and instabilities can form on the plasma-vacuum interface, when perturbed. These perturbations can arise due to things like material roughness in the liner before it ablates or due to asymmetric current flow [39]. Once a perturbation has been seeded, it will grow due to increases or decreases in the magnetic pressure. Recalling that the equation for a liner's self-generated magnetic field

has a $1/R$ dependency, and since magnetic pressure goes as B_θ^2, small perturbations to the liner's radius can lead to rapidly changing magnetic pressures along the liner's surface. This is a positive feedback loop that will continue to cause small perturbations to grow larger and larger until the plasma breaks itself apart.

2.2 Rayleigh-Taylor Instabilities

Now that the basic picture for how these current-carrying plasmas can tear themselves apart has been outlined, a discussion of the deeper physics behind the processes involved can begin. We start with a class of instabilities know as Rayleigh-Taylor instabilities (RTI) [40, 41]. These instabilities form at the boundary of two fluids of disparate densities. When the less dense fluid pushes on the more dense fluid, RTI can grow; if the acceleration is flipped the boundary becomes RT stable. This is a ubiquitous phenomena with examples ranging from supernovae and solar coronas [42] to turbulent mixing in the ocean [2] .

The simplest formulation of linear RTI growth rate is given by:

$$\gamma = \sqrt{Akg}, \tag{2.2}$$

$$A = \frac{\rho_1 - \rho_2}{\rho_1 + \rho_2} \tag{2.3}$$

where A is the Atwood number, ρ is the fluid density, k is the wavenumber, and g is the effective gravity [43]. This simple model is excellent in the small amplitude RT limit and can be used to quickly estimate the order of magnitude of expected growth rates. However, more detail will need to be added to this simple model of RTI in order to make meaningful comparisons to experiments.

So far, only RT that is being accelerated (or under an effective gravity) without the presence of a magnetic field has been considered, but our z-pinches are being accelerated by magnetic fields. When the light fluid is a magnetic field, we get the magneto-Rayleigh-Taylor instability (MRTI). For a planar slab implosion driven by a magnetic field, the MRTI can be described using the following dispersion relation from Harris [44]:

$$\omega^4 - \omega^2 4k_z^2 ag \coth(2ka) - k^2 g^2 (1 - 4k_z^2 a/k) = 0 \tag{2.4}$$

where ω is temporal frequency of the perturbation, g is the effective gravity, k_z is the axial wavenumber (spatial frequency) of the perturbation, and a is the slab thickness. Note that ω can either be purely real or purely imaginary since 2.4 always results in a real valued ω^2. The

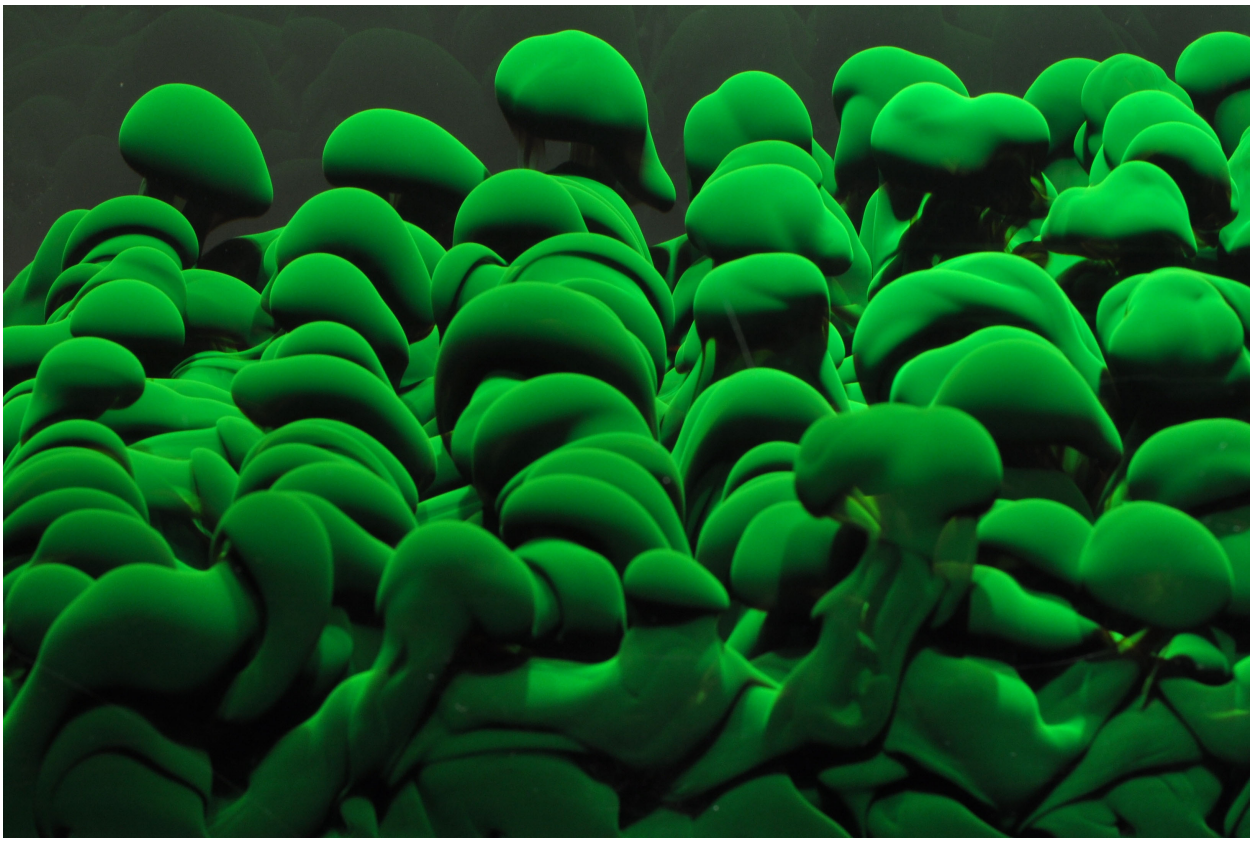

Figure 2.4: An example image of the Rayleigh Taylor instability. The green fluid is lower density fresh water and the clear fluid is higher density salt water. Image by Megan S. Davies Wykes from the University of Cambridge. The image may be found at `http://www2.eng.cam.ac.uk/~msd38/gallery.html` and the associated paper is Ref. [2].

real part represents the oscillating factor of the perturbation (i.e., the sine and cosine factors), while the imaginary part represents a growing or decaying amplitude factor. The instability amplitude grows (decays) if the imaginary part is negative (positive). Harris was the first person to describe MRTI for cylindrical liner implosions, and did so in several limiting cases, as well as deriving this planar slab dispersion relation. Harris's dispersion relation work laid the foundation for subsequent MRTI theory [45, 46, 7]. While we will not be using Harris's models to compare to our experimental values, the planar slab dispersion relation will be useful to see how key parameters like liner thickness and effective gravity affect growth rates.

Throughout this dissertation, two models from Ref. [7] will be used to determine analytic growth rates to be compared to experiment and to determine basic scaling. We use these models as they are robust descriptions of the implosion dynamics, including effects from both axial and azimuthal magnetic field components, which are a key part of the analysis. They provide dispersion relations for both thick and thin shell limits, while also including the so-called Bell-Plesset effects that arise for finite-thickness shells imploding in convergent geometries.

2.2.1 Thick Shell Cylindrical Model

The first model we will explore in detail is the model by Velikovich and Schmit (V&S) [7] for the implosion of a thick cylindrical shell. This model includes effects due to liner thickness, like the model from Ref. [46], as well as to Bell-Plesset effects, which are the effects on the instability growth rate caused by the finite thickness of a shell imploding in a convergent geometry. For example, the instability growth rate can be affected by the velocity of the shell's inner surface relative to the shell's outer surface. The V&S model also includes the effect of an axial magnetic field, B_z, which will play a key role in controlling MRTI growth. The dispersion relation for this model is given by Eq. (D100) in the supplemental material for Ref. [7]:

$$M_{11}M_{22} - M_{12}M_{21} = 0. \tag{2.5}$$

where

$$M_{11} = \frac{G_1}{kR_{out}\Delta}(-\omega^2 - \nu^2 - \Omega^2 + i\nu\omega) + D_{11}(i\nu\omega + \nu^2) - \Omega^2 \tag{2.6}$$

$$- \frac{1}{4\pi\rho R_{out}}\left[\left(\frac{m}{R_{out}}B_\phi + kB_{z,out}\right)^2 \frac{K_{out}}{kK'_{out}} + \frac{B_\phi^2}{R_{out}}\right], \tag{2.7}$$

$$M_{12} = \frac{1}{k^2 R_{out}^2 \Delta}\left(\omega^2 + i\frac{\zeta^2 - 1}{\zeta^2}\nu\omega + \frac{1}{\zeta^2}\Omega^2 + \frac{2}{\zeta^4}\nu^2\right) \tag{2.8}$$

$$- \frac{1}{kR_{out}}\left(i\nu\omega + \frac{1}{\zeta^2}\nu^2\right)D_{21}, \tag{2.9}$$

$$M_{21} = \frac{1}{k^2 R_{in}^2 \Delta}\left(- \omega^2 + i\frac{\zeta^2 - 1}{\zeta^2}\nu\omega - \Omega^2 - \frac{\zeta^2 + 1}{\zeta^2}\nu^2\right) \tag{2.10}$$

$$+ \frac{1}{kR_{in}\zeta}(i\nu\omega + \nu^2)D_{21}, \tag{2.11}$$

$$M_{22} = \frac{G_2}{kR_{in}\Delta}\left(- \omega^2 + i\frac{1}{\zeta^2}\nu\omega - \frac{1}{\zeta^2}\Omega^2 + \frac{\zeta^2 - 2}{\zeta^4}\nu^2\right) \tag{2.12}$$

$$+ \left(i\frac{1}{\zeta}\nu\omega + \frac{1}{\zeta^3}\nu^2\right)D_{22} - \frac{1}{\zeta^2}\left(\Omega^2 + \frac{1 - \zeta^2}{\zeta^2}\nu^2\right) - \frac{kB_{z,in}^2}{4\pi\rho R_i n}\frac{I_{in}}{I'_{in}} \tag{2.13}$$

This gives a 4th order polynomial in ω, while the parameters Δ, ζ, Ω, and ν are given by:

$$\nu = \frac{\dot{R}_{out}}{R_{out}}, \tag{2.14}$$

$$\Omega^2 = \frac{g_{out}}{R_{out}} = -\frac{\ddot{R}_{out}}{R_{out}}, \tag{2.15}$$

$$\zeta = \frac{R_{in}}{R_{out}}, \tag{2.16}$$

where the outer and inner liner radius are the variables R_{out} and R_{in} respectively. The parameters G_1, G_2 are given by:

$$G1 = I'_{in}K_{out} - I_{out}K'_{in}, \tag{2.17}$$

$$G2 = I'_{in}K_{out} - I'_{out}K_{in}, \tag{2.18}$$

$$\Delta = I'_{in}K'_{out} - I'_{out}K'_{in}. \tag{2.19}$$

These parameters rely heavily on I and K, which are the modified Bessel functions of the

first and second kind with primes denoting their derivatives. The arguments to these Bessel functions are given as:

$$I_{out} = I_m(kR_{out}), \quad I_{in} = I_m(kR_{in}), \tag{2.20}$$

$$K_{out} = K_m(kR_{out}), \quad K_{in} = K_m(kR_{in}) \tag{2.21}$$

where k and m are the axial wavenumber and integer azimuthal mode number, respectively. Finally, the last set of parameters to define are:

$$D_{11} = 1 - \frac{G_1}{\Delta^2}(I'_{in}K''_{out} - I''_{out}K'_{in}) + \frac{1}{\zeta\Delta}(I''_{in}K_{out} - I_{out}K''_{in}) \tag{2.22}$$

$$- \frac{G_1}{\zeta\Delta^2}(I''_{in}K'_{out} - I'_{out}K''_{in}), \tag{2.23}$$

$$D_{12} = -\frac{1}{\Delta^2}\left[I'_{in}K''_{out} - I''_{out}K'_{in} + \frac{1}{\zeta}(I''_{in}K'_{out} - I'_{out}K''_{in})\right], \tag{2.24}$$

$$D_{21} = D_{12}, \tag{2.25}$$

$$D_{22} = \frac{I_{in}K''_{out} - I''_{out}K_{in}}{\Delta} - \frac{G_2}{\Delta^2}(I'_{in}K''_{out} - I''_{out}K'_{in}) \tag{2.26}$$

$$+\frac{1}{\zeta}\left[1 - \frac{G_2}{\Delta^2}(I''_{in}K'_{out} - I'_{out}K''_{in})\right] \tag{2.27}$$

Note that in this model, the following convention is used for the complex ω. The real part represents the oscillating factor of the perturbation (i.e., the sine and cosine factors), while the imaginary part represents a growing or decaying amplitude factor. The instability amplitude grows (decays) if the imaginary part is negative (positive).

The entire derivation of this model will not be discussed, but we will briefly discuss the major assumptions needed to arrive at the dispersion relation. The derivation of this model begins by determining motion of a driven shell (a liner). This shell is assumed to be incompressible ($\nabla \cdot \mathbf{v} = \mathbf{0}$) and its density is assumed constant. Incompressibility, in turn, implies that the velocity potential ($\mathbf{v} = \nabla\mathbf{\Phi}$) satisfies a Laplacian ($\nabla^2\mathbf{\Phi} = \mathbf{0}$). This incompressible shell is also assumed to be a perfectly conductor (no magnetic fields can exist in the shell itself), this makes the boundary conditions for the magnetic fields much simpler. Once the motion of the shell has been determined, it is then perturbed in the usual linear fashion, with small amplitudes and long wavelengths (shell thickness much smaller than perturbation wavelength). The perturbed flow inside the shell is assumed to be curl free ($\nabla \times \mathbf{v}^{(1)} = \mathbf{0}$, where the superscript (1) denotes a perturbed value). For a full derivation of

this model, see Ref. [7].

2.2.2 Thin Shell Cylindrical Model

The second model we will make use of is a thin shell version of the thick shell model we have just described. We can arrive at this model by making the assumption that the shell in the perturbation equations is infinitesimally thin. Working through the math yields the following dispersion relation:

$$\omega^4 - i\frac{2m^2\dot{R}}{(k^2R^2+m^2)R}\omega^3 + W\omega^2 - i\frac{2m^2W\dot{R}}{(k^2R^2+m^2)R}\omega - \left(k^2+\frac{m^2}{R^2}\right)g^2 = 0, \tag{2.28}$$

which is again 4th order in ω, where

$$W = -\frac{g}{R} + \frac{1}{2\mu}\left[B_\phi^2 + (mB_\phi + kRB_{z0})^2\frac{K_m}{kRK_m'} - B_{z,in}^2\frac{kRI_m}{I_m'}\right], \tag{2.29}$$

and where $\mu = 2\pi R_0 d\rho$ is the areal density. Again our solution depends on the modified Bessel functions I and K. Note that the value ω is complex in this case as long as $\dot{R} \neq 0$, or, in other words, ω is complex due to Bell-Plesset effects. This is also the reason for complex ω values in the thick-shell-model (but it is easier to see in this formulation).

2.3 Dynamic Screw Pinches

We have discussed one type of pinch, the z-pinch, and how unstable they can be. But what if our experiment requires a uniform surface? Is it possible to control the growth of these instabilities? These are problems that plague not only pinches, but all plasma confinement schemes. For z-pinches in particular, several ideas are already being implemented in present day experiments to control instability growth. Most of these ideas revolve around tamping out early time instabilities like the electrothermal instiablity (ETI) and the electrochoric instability (ECI) [47], which are thought to be seeds for the larger amplitude instabilities observed later in time. Instabilities like ETI and ECI are material based and have been combated through liner material choices and liner coatings [48, 49, 50, 51].

The fastest growing modes, known as interchange modes, for liner implosions are ones that satisfy $\mathbf{k}\cdot\mathbf{B} = \mathbf{0}$, where k is the perturbation wave vector and B is the magnetic field vector. These modes are the fastest growing modes because they are not affected by the stabilizing influence of magnetic tension, meaning they can move magnetic field lines without bending them. In a standard z-pinch configuration, where an axial current induces an azimuthal

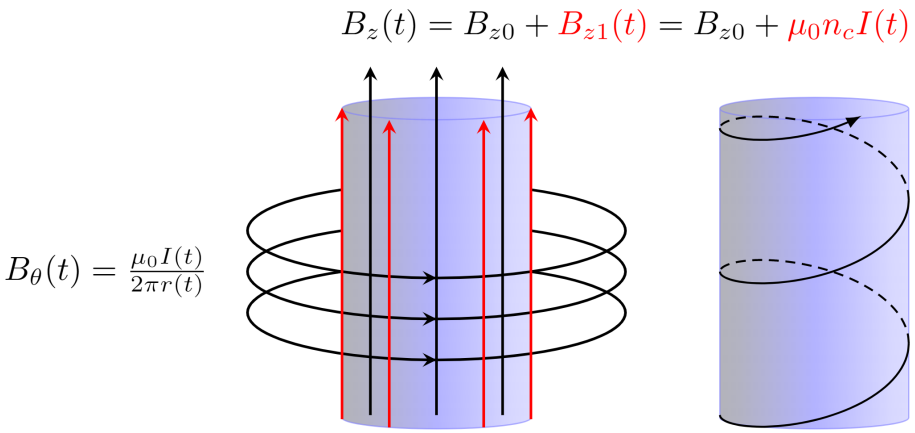

Figure 2.5: An illustration of a liner with axial magnetic fields imposed on it. For the configuration to be considered a dynamic screw pinch, the axial magnetic field must vary in time (the red axial field lines), otherwise it is a standard z-pinch configuration, even with a static axial field applied (the black axial field lines). The liner on the left has the two field components separated while the liner on the right is what the overall field structure will look like for both the magnetized SZP case and the DSP case. Note that the configuration can still be a DSP when $B_{z0} = 0$.

magnetic field, the fastest growing modes are azimuthally symmetric, with an azimuthal mode number $m = 0$.

In Ref. [52] the authors propose a novel instability control method for liner implosions known as a dynamic screw pinch (DSP). Previously, this technique was used to stabilize gas-puff z-pinch implosions [53]. The DSP is generated using a helical return-current structure, which surrounds the imploding liner, rather than the straight return-current structure of a standard z-pinch. CAD models and hardware specifications will be provided in Chapter 3. The helical return-current path results in a helical magnetic field, $\mathbf{B}(t) = B_\theta(t)\hat{\boldsymbol{\theta}} + B_z(t)\hat{\mathbf{z}}$, at the liner's outer surface, which drives the implosion, see Fig. 2.5. The components are given by $B_\theta(t) \approx \mu_0 I(t)/[2\pi r_\ell(t)]$ and $B_z(t) \approx \mu_0 n_c I(t)$, where n_c is the number of turns per unit length of the helical return-current structure.

Since only the B_θ component depends on the liner radius, the ratio of the components will remain fixed until the liner starts to implode. During the implosion, $B_\theta(t) \propto I(t)/r_\ell(t)$ increases relative to $B_z(t) \propto I(t)$. This dynamically rotates the angle of the driving magnetic field $\phi_B(t) = \arctan[B_z(t)/B_\theta(t)] = \arctan[2\pi n_c r_\ell(t)]$, with $\mathbf{B}(t)$ approaching a pure azimuthal field as $r_\ell(t)$ approaches the cylindrical axis.

The rotating magnetic field thus drives a spectrum of modes (and azimuthal mode numbers), with $\mathbf{k} \cdot \mathbf{B} = 0$ satisfied at some point during the implosion. Since a different mode is being driven in each moment in time this reduces the overall duration that any single

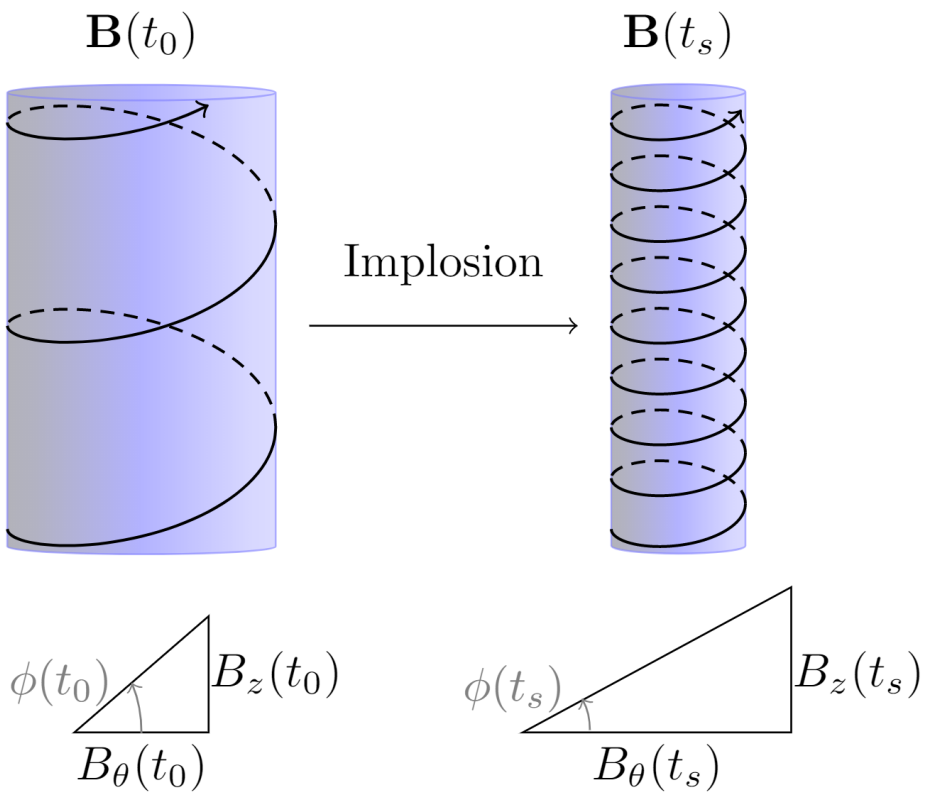

Figure 2.6: An illustration of a liner undergoing a DSP implosion. Underneath are illustrations of the two components of the magnetic field and how they will as the liner implodes. The axial componentis proportional to the driving load current, $I(t)$, throughout the implosion, while the azimuthal component is proportional to $I(t)/R(t)$, where $R(t)$ is the radius of the liner's outer surface. Thus, as $R(t)$ goes to zero, the magnetic field's helical pitch angle $\phi(t)$ goes to zero. Note that the field components being illustrated here are along the liner's outer surface, not inside the liner

mode is driven with $\mathbf{k} \cdot \mathbf{B} = 0$ satisfied. By contrast, in a standard z-pinch configuration, $\mathbf{k} \cdot \mathbf{B} = 0$ is satisfied throughout the entire implosion for one and only one azimuthal mode number: $m = 0$. The calculations presented in Ref. [52] suggest that, for the thick-shell liners on Z, the cumulative exponential growth for a DSP-driven implosion could be 1 to 2 orders of magnitude less than that of a standard z-pinch-driven implosion. In Ref. [52] they used the Semi-Analytic MagLIF Model (SAMM) [3] to simulate implosion trajectories for their dispersion relations in order to calculate growth rates.

Since the magnetic field configuration of a DSP resembles that of an axially pre-magnetized SZP, it is important to clarify how they are different. Both the SZP and the DSP can either include or exclude a background axial magnetic field, B_{z0}. An example of an axially premagnetized SZP is the standard MagLIF configuration. Also, as proposed in Ref. [52], an axially premagnetized MagLIF target could be driven by a DSP to help further stabilize the liner implosion. MagLIF uses the background axial field to thermally insulate the hot fuel from the cold liner wall and to trap charged fusion products in the fuel during fusion burn. However, this background axial magnetic field also provides a stabilizing magnetic tension term (i.e. the background axial field helps keep $\mathbf{k} \cdot \mathbf{B} \neq 0$). By contrast, a DSP that does not include a background axial magnetic field relies on the implosion of the liner to rotate the helical pitch angle of the driving magnetic field to create its stabilizing effects.

Note that the axially premagnetized SZP should also have a rotation of its magnetic field pitch angle. However, there are differences in how the pitch angle rotates in an axially premagnetized SZP versus a DSP without a background axial field. This difference is illustrated in Fig. 2.7, where we plot $\phi_B(t)$ and its time derivative $d\phi_B/dt$. In the DSP cases, the polarization angle only rotates approximately 5°, while the premagnetized SZP case rotates by almost 90°. However, nearly all of the rotation in the premagnetized SZP case happens well before the liner begins its implosion, while all of the rotation for the DSP cases occurs during the implosion. As we have discussed, MRTI growth is driven by acceleration, and if the field lines rotate only when there is little to no acceleration, then no stabilizing effects due to rotation will be conferred. The only way to push the rotation later in time would be to use much stronger pre-imposed static axial fields. For the pre-magnetized SZP case plotted in Fig. 2.7, a pre-imposed axial field of 2 T was used. Compared to the peak azimuthal magnetic field of roughly 100 T, it is no wonder that nearly all of the rotation happens so early.

Additionally, one may want to get rid of B_{z0} coils to simplify MagLIF. This would reduce the high inductance of the tall swooping power feeds in MagLIF, which would allow more current to be delivered to the liner. This may be possible if, as Ref. [54] suggests, the DSP can inject sufficient amounts of axial magnetic field into the liner.

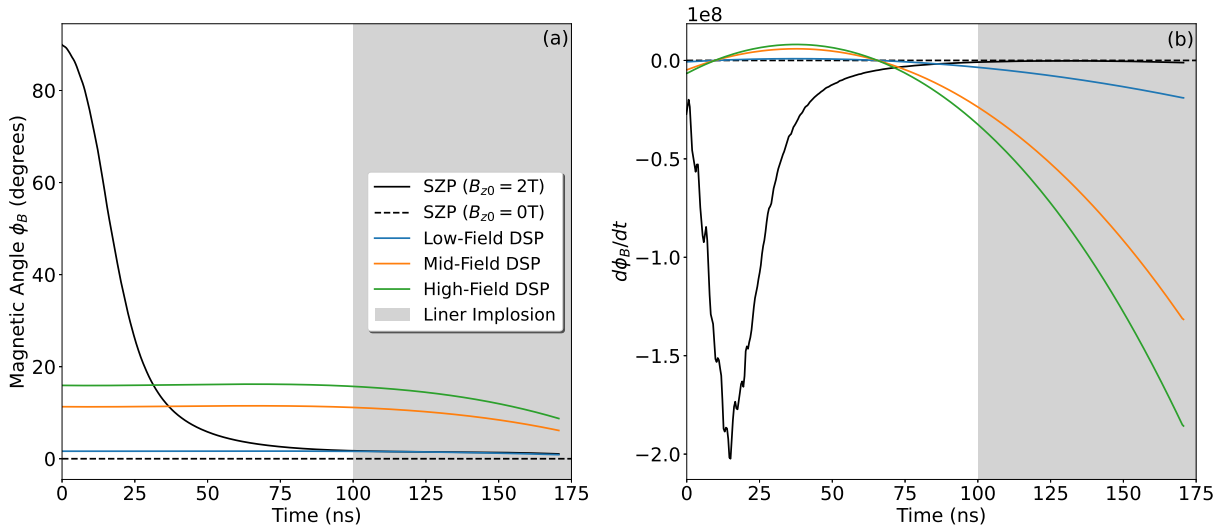

Figure 2.7: Plots of (a) the magnetic polarization angle, ϕ_B, and (b) its derivative, with respect to time $d\phi_B/dt$. Three DSP cases, which were tested experimentally (see Chapter 4), are are plotted along with an axially premagnetized SZP case. The DSP cases have peak axial magnetic field values of 2 T, 14 T, and 20 T, while the SZP uses a static axial magnetic field of 2 T. Note that in (b) the magnetized SZP case is scaled down by 95%.

2.4 MRTI Growth Rates

Now that descriptions of our liner implosions have been developed, we can begin to explore what growth rates we might expect in experiments. By solving for the roots of the dispersion relations presented in Section 2.2 the instantaneous growth rate, γ, can be calculated. In this convention, the largest value of $-Im(\omega)$ is the most unstable mode. From the instantaneous growth rate, the cumulative instability growth (in terms of the number of e-foldings) can be calculated using $\Gamma = \int_{t1}^{t2} \gamma(t')dt'$.

We will be making use of a simple thin-shell implosion model (see Appendix A) as well as the SAMM code [3] to simulate implosion trajectories we might expect to find in experiment in order to determine the fastest growing modes. In Fig. 2.8, we present example trajectories from the simple thin-shell model and from SAMM. The thin-shell trajectory is a simulation of what we might expect in a thin-foil experiment driven by a 1-MA, 100-ns university-scale facility. The thick-shell SAMM trajectory is an example of a MagLIF liner implosion driven by a 20-MA, 100-ns current pulse on the Z facility at Sandia. Given that MRTI is driven by acceleration, the similar implosion trajectories (and thus similar acceleration histories) demonstrated here suggest that MagLIF-relevant MRTI studies can be executed on smaller, 1-MA facilities. This will also allow us to more easily compare MRTI simulations of 1-MA implosions with those presented for MagLIF on the Z facility in Ref. [52].

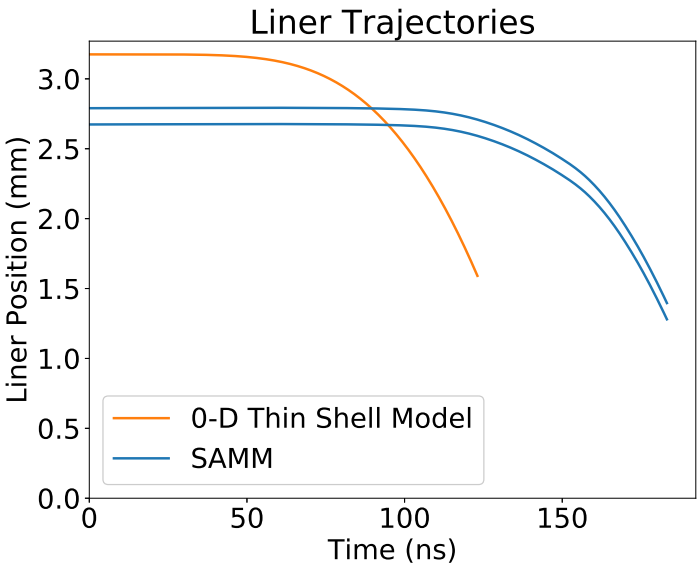

Figure 2.8: A plot of simulated liner trajectories the simple thin-shell (0-D) implosion model and the SAMM code [3] model for convergence ratios of 2, where the convergence ratio is defined as $C_r = R_{out,i}/R_{out,f}$.

With the liner implosion trajectories in hand, we can now see what modes the V&S theory of Ref. [7] predicts will be the fastest growing for two cases: the thick shelled dispersion relation using the SAMM trajectory and the thin shelled dispersion relation using the thin shell trajectory. In Figures 2.9 and 2.10, we present the cumulative instability growth Γ (the number of e-foldings) over a wide range of azimuthal mode numbers, m, and normalized axial mode numbers, $\hat{k} = k_z/(2\pi/L)$, where L is the axial length of the liner (1 cm). The theory predicts predicts that larger $\hat{k}$ values (shorter wavelengths), along with negative mode numbers, m, will be the fastest growing modes in the DSP case, while in the standard z-pinch case, modes with $m = 0$ will be the fastest growing. In the DSP case, the sign of m matters for growth rates. Modes with negative m correspond to plasma helices with a chirality (or "handedness") that matches that of the helical global magnetic field, while modes with positive m correspond to plasma helices with a chirality that is opposite to that of the global magnetic field [6, 55, 56].

In Figures 2.9 and 2.10, the thick shell case (see Fig. 2.9) has a much narrower band of intense instability growth relative to the thin shell case (Fig. 2.10). At the top of the band of intense intability growth, in the thick shell case, we also see peak e-folding values that are slightly higher than in the thin shell case. Overall, the DSP is predicted to have a larger stabilizing effect in the thick shell case.

Harris showed in the planar slab's two limiting cases that: (1) the fastest growing modes

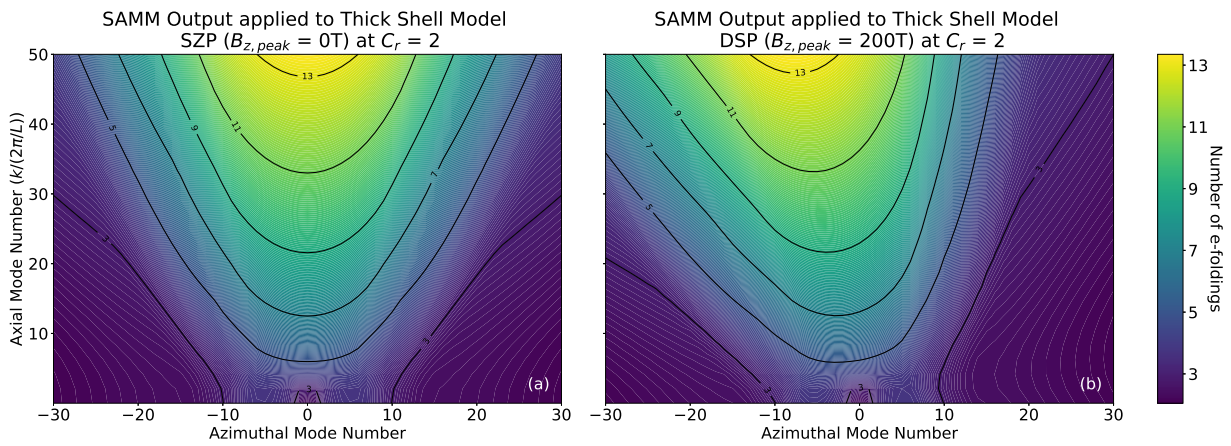

Figure 2.9: Contour plots of the cumulative instability growth, Γ (number of e-foldings), for the simulated SAMM implosion for both (a) a SZP case and (b) a DSP case.

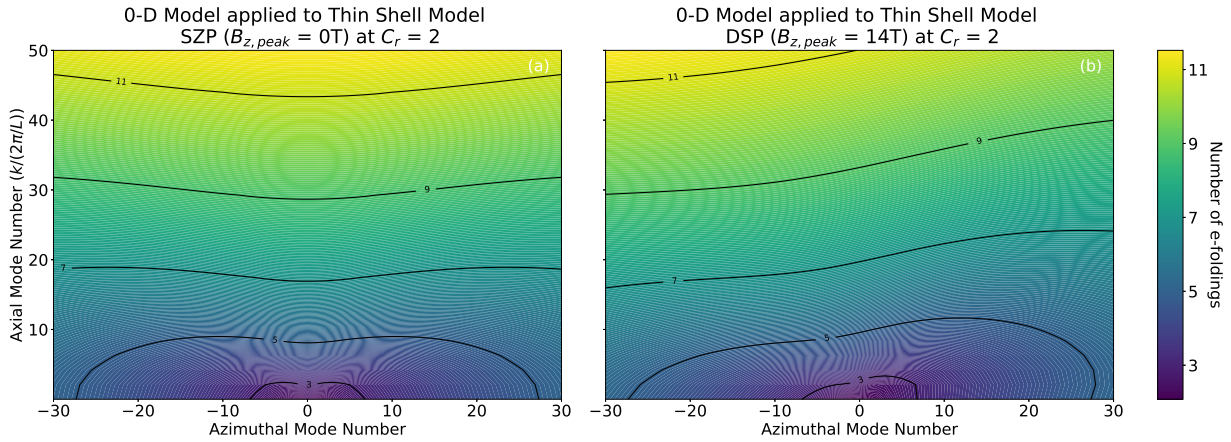

Figure 2.10: Contour plots of the cumulative instability growth, Γ (number of e-foldings), for the simulated thin shell model implosion for both (a) a SZP case and (b) a DSP case.

are thickness independent, you recover the usual $\omega^2 = \pm kg$, with the negative sign being the unstable mode, and (2) the condition for unstable modes is $\lambda > 8\pi a \cos^2\theta$ (Eq. 36 in Ref. [44]). As a reminder, Harris uses a for shell thickness and θ as the angle between k and B. This condition directly depends on liner thickness and states that shorter wavelengths, relative to the liner thickness, will be stabilized. In other words, the stabilization benefits from nonzero $\mathbf{k} \cdot \mathbf{B}$ depend intimately on the liner thickness.

While these plots give us an idea of how much growth to expect in our experiment, they do have two very important shortcomings that we will try and address. First, these instability growth models are linear perturbation theories as discussed previously. They rely on *small amplitude* perturbations to the plasma that follow the form $\exp(-i\omega t + ikz - im\theta)$. In our

experiments, we do see nonlinear MRTI evolution, and thus an analytic nonlinear MRTI model would be ideal. Unfortunately, we do not know of a robust, analytic, nonlinear MRTI framework for this particular application; although there has been ample work done for the weakly non-linear RT and MRT regimes [57, 58, 59, 60, 61]. Nonetheless, as will be shown when we analyze our experimental data in Chapter 4, the linear theory does give us a reasonable estimate of the relative stabilization that could be expected when comparing the SZP to various DSP cases.

The second shortcoming is that these cumulative growths ignore mode merging phenomena that have been previously observed in experiment [62, 56, 63] and simulation [64]. From these past experimental observations, we know that the dominant instability structures start out with very large k and m values (corresponding to very short overall wavelengths, $\sim$ 50 µm). These k and m values decrease precipitously as the implosion evolves (i.e., the dominant overall wavelength grows precipitously throughout the implosion, often with values $\sim$ 1 cm at stagnation). As an example of how mode merging works, see Fig. 2.11. In the leftmost image of this figure, there are four intertwined helices present (i.e., $m = 4$). In the rightmost image, the four helices have merged into two intertwined helices (i.e., $m = 2$). Note that in this example, the axial wavelength, λ_z, doubles after the merging (meaning k_z decreases by a factor of 2), while the helical pitch $p = \lambda_z m = 2\pi m/k_z$ remains constant. Note that p (and thus m/k_z) will remain constant as long as axial outflows are not permitted. Axial outflows could, in principle, stretch the helices in the axial direction, which would increase p.

In experiments, however, we do not usually see a full 3D picture of this phenomena; instead, we take pictures of the plasma and see a 2D projection. In the 2D images from such an experiment, we would typically observe many small instability peaks on the edges of the plasma. This is illustrated in Fig. 2.12. Working from left to right in this figure (i.e., stepping forward in time), illustrates a mode merging event as would be seen in a sequence of shadowgraphs taken from a side-on field of view. If we first focus on two peaks that are moving toward one another (one peak from each of the two intertwined helices), we see that both peaks become taller (both peaks increase in radius), while the single trough between these two approaching peaks becomes shallower (as the bottom of this trough also increases in radius). This occurs until we are left with a single peak at large radius. If we now focus on two peaks that are moving away from one another, then the trough between these two peaks becomes deeper (as the bottom of this trough decreases in radius). This occurs until we are left with a single, deep trough at a small radius.

Imploding helical structures can be described by their helical pitch angle

$$\phi_{plasma} \approx \arctan[p/(2\pi R)] \approx m/(k_z R) \tag{2.30}$$

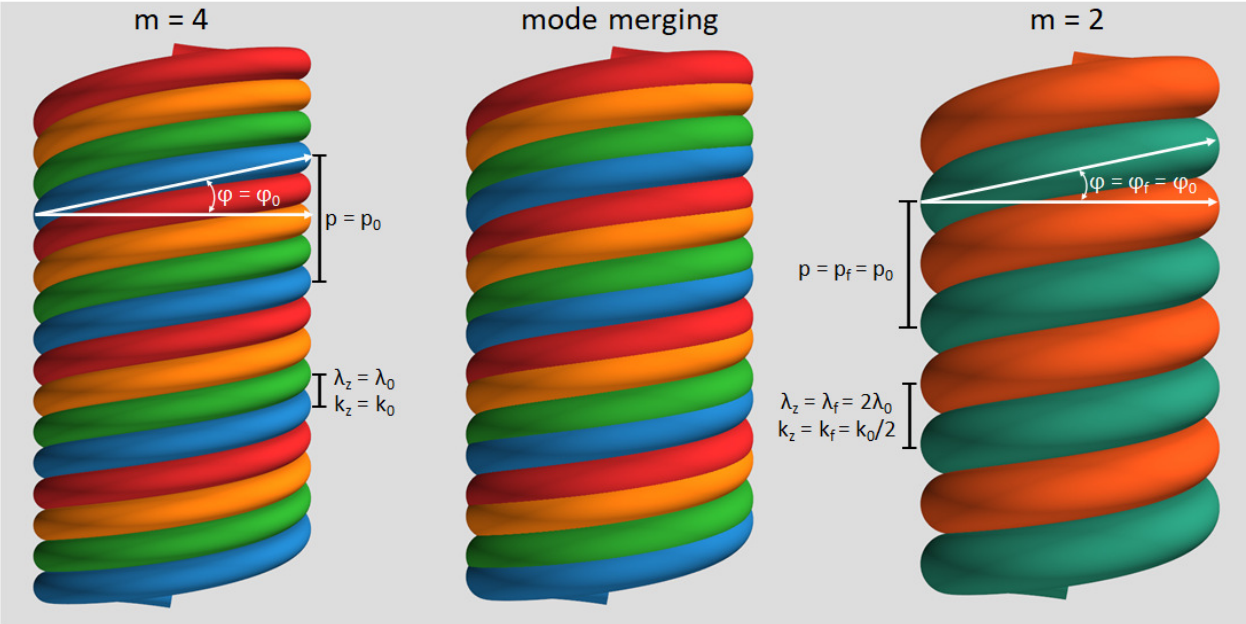

Figure 2.11: An illustration of a mode merging event. In the leftmost image, we see 4 plasma helices, in blue, green, orange, and red, so this is an m=4 mode. The helices grow and move into one another during the mode merging phase. Finally, in the rightmost image, we are left with only 2 helixes, in blue-green and red-orange, so we have arrived at an m=2 mode. We also see that the pitch angle ϕ remains the same since the plasma column is neither expanding radially nor being compressed radially. While the axial instability wavelength has doubled, the pitch p (and thus the quantity m/k_z), of each of the helices remains the same. Note that p (or m/k_z) is constant because there are no axial outflows permitted. Axial outflows could, in principle, stretch the helices in the axial direction, which would result in an increasing helical pitch p.

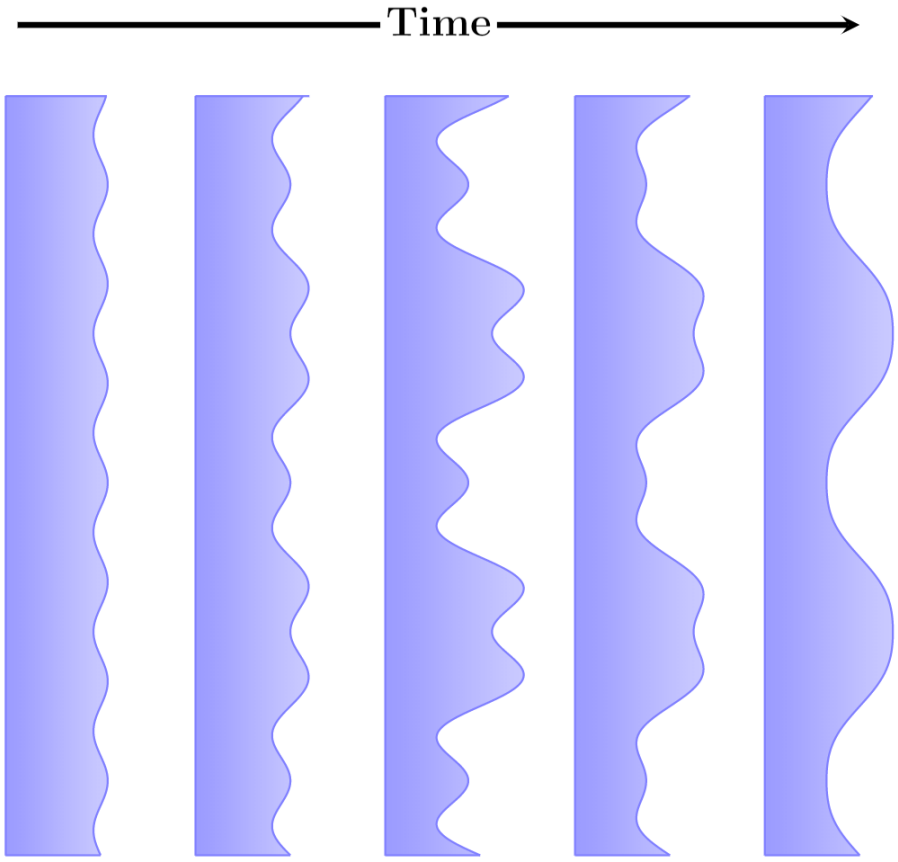

Figure 2.12: A mode merging event, as viewed through a cartoon of a shadowgraphy image sequence. While the helical structure is not as readily apparent as on the previous figure, we can infer mode structure from the edge of the plasma.

where p is the pitch and k_z is the axial wave number [65, 46]. This theory relies on the assumption that $m/k_z \approx constant$, meaning that if the mode number m changes, the axial wavenumber k_z must proportionally change along with it. From our example, in Figures 2.9 and 2.10, it is easy to see why the assumption holds. Using Eqs. 2.30 to describe the behavior of the dominant instability mode, we can now estimate how the dominant azimuthal mode number will change as the liner implodes, given starting and ending axial wavelengths for the dominant instability mode.

CHAPTER 3

Experimental Design

In this Chapter the experimental setup, design, and pulsed-power drivers for our experiment, along with the diagnostic suite used to collect data will be described.

3.1 The COBRA Pulsed Power Driver

The COBRA (Cornell Beam Research Accelerator) pulsed power generator is a Marx-based, low-impedance (0.5 Ω) driver used for high energy density plasma experiments [4, 66]. It provides a 1-MA peak current with a rist time of 100 ns in short pulse mode or 0.9 MA in 200 ns in long pulse mode. Such short pulses are achieved through pulse compression. Referring to Fig. 3.1, two Marx generators send a pulse to two water dielectric intermediate storage capacitors (ISC). Each ISC is then switched by the two main self-breaking gas switches, which send the pulse to four coaxial water dielectric pulse-forming lines (PFLs). These PFLs are connected to a current adding tri-plate transmission line via four output switches. This tri-plate structure is in vacuum and feeds power radially inward and slightly upward using two power flow levels (an upper level and a lower level). These two levels are self-magnetically insulated transmission lines (MITLs). Their outputs are combined via a post-hole convolute into a single, final power feed. The final power feed swoops upwards into the experimental vacuum chamber and connects to the experimental load hardware and target. Short and long pulse modes are achieved by changing the pressure in the two main switches to connect the two Marx generator outputs synchronously (short pulse) or asynchronously (long pulse). No pulsed power driver operates perfectly, and COBRA is no exception, so long pulses will often be produced when trying to operate in short pulse mode.

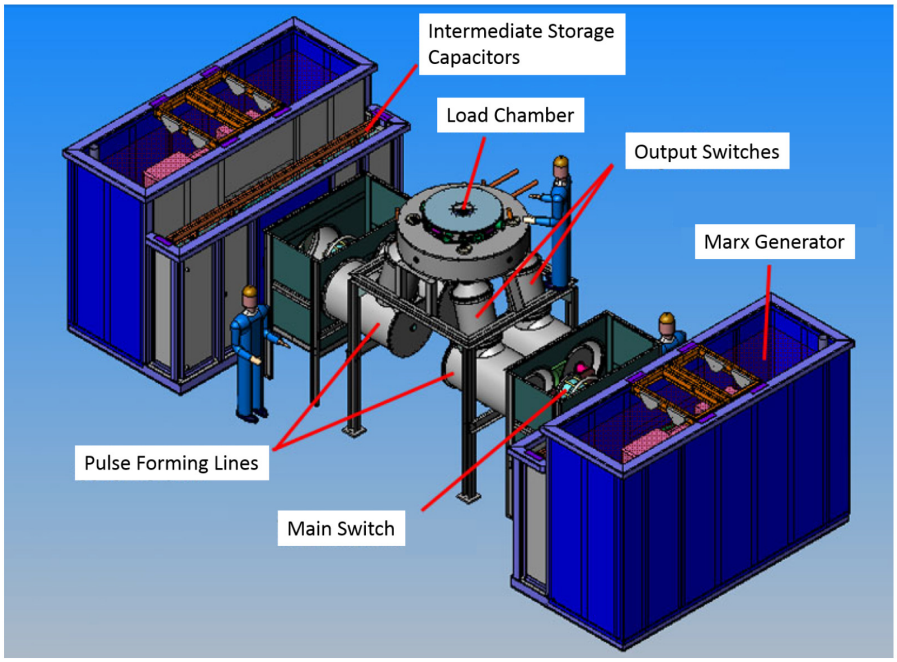

Figure 3.1: A schematic of the COBRA pulsed power driver at Cornell University [4].

3.2 Helical Return Current Path Design

In Chapter 2 how the DSP will stabilizes implosions via a helical return-current path was discussed, but what do we mean by helical return-current path? Return current structures in standard z-pinches often have straight posts, as shown in Fig. 3.2. For the DSP cases, we will modify the posts by tilting or twisting the posts into a helical structure. By modifying the direction current flows, we will be able to generate the needed axial component of our magnetic field to complement the already self-generated azimuthal component. Typically, return current posts are kept far away from the liner in order to keep perturbations to the liner's self generated magnetic field at a minimum. However, in the DSP case, the helical return-current posts can not be moved too far away from the liner due to inductance constraints. Recalling from earlier in this section that pulsed power drivers can be reduced to simple LC circuits, minimizing inductance is key for optimizing pulsed power drivers. Keeping this in mind, we will have to balance the pitch of our return current posts, the radius of the posts, and the overall height of the return can in order to produce the axial magnetic fields while not needlessly adding inductance to our circuit.

COBRA was designed to drive loads of roughly 10 nH but has been used to drive more inductive loads, some around 20 nH. Due to this inductance constraint, we designed our experiments to have inductances of 10 nH or less. CST EM Studio, a 3D electromagnetic analysis software package, was used to design return-current structures and estimate their

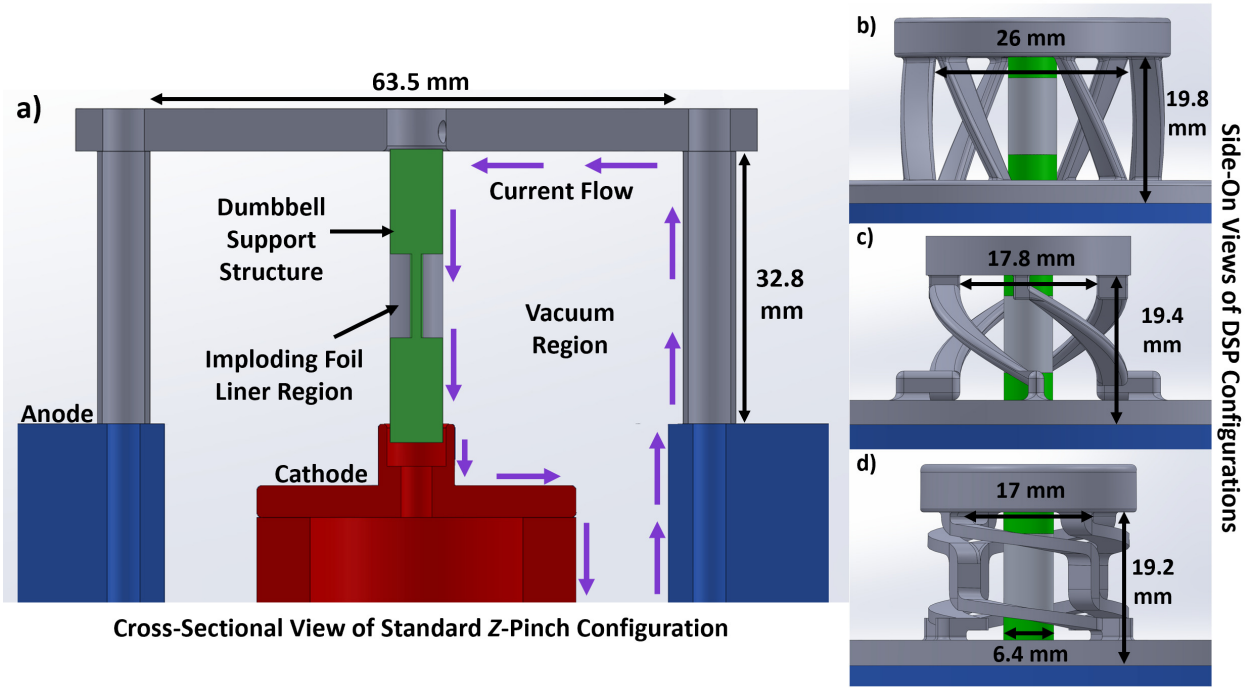

Figure 3.2: CAD models of all the return-current structures tested in these experiments. (a) The straight z-pinch return-current structure with an illustration of the power feed. (b) The low-field twisted return-current structure, predicted to have a peak axial field of 2 T. (c) The mid-field twisted return-current structure, predicted to have a peak axial field of 14 T. (d) The high-field twisted return-current structure, predicted to have a peak axial field of 20 T. Heights are measured from the top of the anode plate (blue) to the bottom of the return-current structure's lid. Diameters are measured from the inside edges of the return-current posts/twists.

inductances. Note that these target inductances are also in line with load inductances that can be driven by the MAIZE LTD, described in Appendix B

For these experiments, one straight return-current structure and three different helical return-current structures were designed, simulated, fabricated, and tested (see Fig. 3.2). Despite their helicity, the twisted return-current structures had inductances similar to that of the SZP return-current structure, because the straight structure was both taller and wider than the DSP structures. The simulated inductances for these return current structures were 8.32 nH for the SZP, 6.61 nH for the low-field DSP case, 6.98 nH for the mid-field DSP case, and 9.76 nH for the high-field DSP case. The straight return-current structure was machined out of 304 stainless steel, while the twisted structures were 3D printed using a binder jetting process from a mix of 316 stainless steel and bronze (60% steel, 40% bronze).

Useful metrics for characterizing the strength of a given DSP configuration include the peak

Table 3.1: Parameters to characterize the four return-current structures tested on COBRA: the SZP, the low-field DSP, the mid-field DSP, and the high-field DSP.

Pinch Type	$B_{z,peak}$ (T)	n_c (1/cm)	$\theta_{B,0}$
SZP	0	0	0
Low-Field DSP	2	0.0271	0.0275
Mid-Field DSP	14	0.1855	0.187
High-Field DSP	20	0.2616	0.275

axial magnetic field generated, the initial ratio of the axial and azimuthal field components (which is constant up until the time when the liner starts to implode radially inward), and the return-current structure's number of turns per unit length, n_c. In Table 3.1, these parameters are provided for each SZP/DSP case tested on COBRA. The parameter $\theta_{B,0} = B_{z,0}/B_{\theta,0}$ represents the ratio of the field compnents before the liner implodes.

The DSP provides additional benefits beyond enhanced stability. For example, due to the additional magnetic drive pressure from the B_z component, and given the same load current pulse, a DSP-driven MagLIF implosion could reach stagnation about 10 ns earlier than a standard MagLIF implosion [52]. Alternatively, for the same implosion time, the DSP can drive a liner with a larger initial radius and thus impart more kinetic energy into the imploding shell [53]. Furthermore, calculations suggest that the DSP configuration could be used to inject axial magnetic field into the MagLIF fuel, potentially removing the need for external B_z coils [54, 67].

How the additional drive pressure comes about is a subtle point that is not at all obvious at first glance. Initially one might guess that this additional drive pressure just comes about from the return current posts in the DSP case being placed at smaller radii. While it is true that this increases the magnetic pressure generated, a DSP return current structure with posts at the same radius as its SZP counterpart can *still* produce more magnetic pressure. To help understand this phenomena we will first look at Fig. 3.3, which shows the inner cylindrical conductor of a coaxial system delivering a current pulse to a region with helical current flow.

In this picture, both a streamline and vector representation of the current density driven along the inner conductor's (and liner's) outer surface is shown. The total current being supplied by the generator and being returned to it, is $I = J_z \cdot 2\pi r$, where J_z is the axial component of the linear surface current density (units of A/m). In the helical current flow section, the additional surface current density, J_θ, is induced, where J_θ is the azimuthal component of the linear surface current density (again with units of A/m). This comes from the changing axial magnetic field, $\dot{B}_z$, generated by the surrounding helical return current

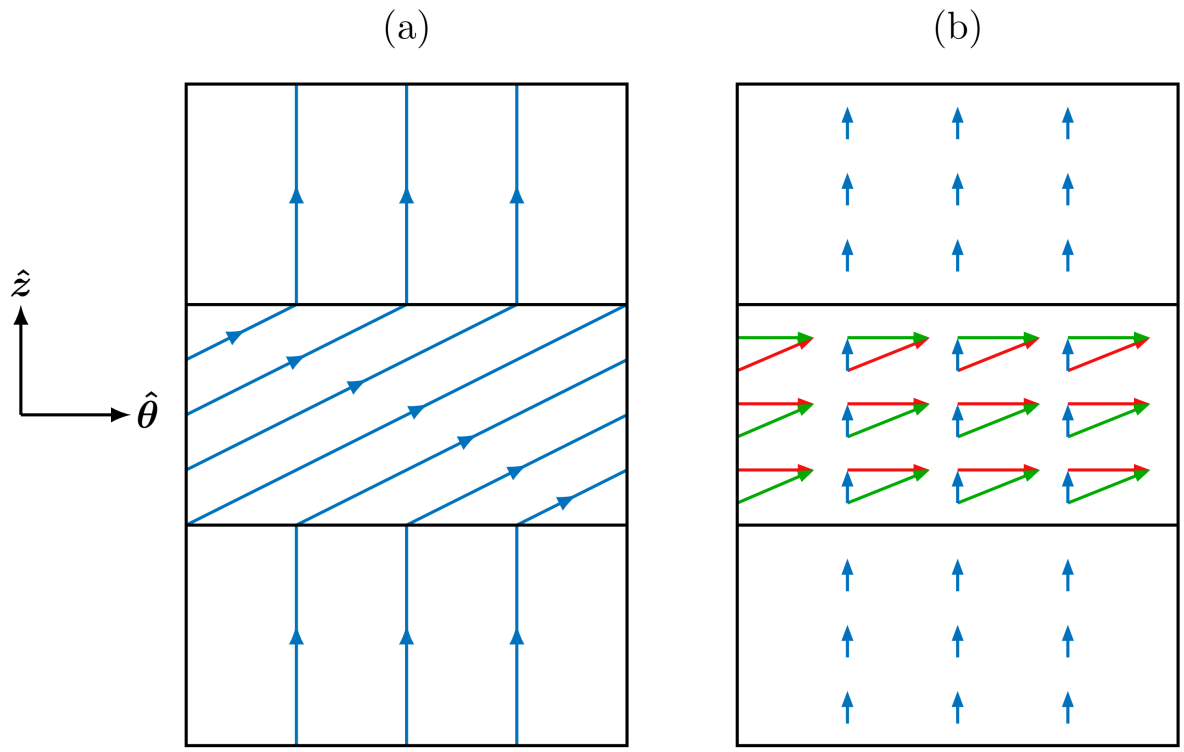

Figure 3.3: Representations of the surface current density $\mathbf{J}$ along the outer surface of a cylindrical conductor, unwrapped in the $\hat{\boldsymbol{\theta}}$ direction. The central region, which represents the outer surface of a liner, has an induced J_θ, which results in a net helical current flow. (a) Streamlines of current, where the density of the streamlines indicates the magnitude $|\mathbf{J}|$. Geometrically, since every streamline $\mathbf{J}$ flowing into the bottom of the helical section must flow out of the top of the helical section, and since $\mathbf{J}$ becomes tilted in the helical section, the streamline density must increase. Thus $|\mathbf{J}|$ must increase in the helical section. (b) A vector-arrow representation of $\mathbf{J}$, which shows that J_z (blue arrows) is continuous everywhere along this conductor, including across the interfaces between regions with helical and purely axial flows. Were this not the case, a local charge density, $\rho(t)$, would build up at the interfaces between the regions.

structure. Note that J_θ must be induced on the liner's outer surface to satisfy the boundary condition for a time-changing magnetic field surrounding a perfect conductor, $B_z = \mu_0 J_\theta$. This means that J_θ does not originate from or return to the generator, i.e., it is a separate circuit (or loop) from the circuit (or loop) that includes the generator. Nonetheless, the generator supplies all of the power for the magnetic flux in the system, including both circuits (or loops). To better understand this coupling between the two circuits, we will address the partitioning of supplied generator power.

First note that J_z in the helical section is equal to J_z in the pure axial sections above and below the helical section. This must be the case in order to satisfy the charge continuity equation:

$$\nabla \cdot \mathbf{J} = \frac{1}{r}\frac{\partial}{\partial r}(rJ_r) + \frac{1}{r}\frac{\partial J_\theta}{\partial \theta} + \frac{\partial J_z}{\partial z} = -\frac{\partial \rho}{\partial t} = 0. \tag{3.1}$$

Since J_θ is not varying in the $\hat{\boldsymbol{\theta}}$ direction, we know that $\frac{\partial J_\theta}{\partial \theta} = 0$, and because $J_r = 0$ everywhere, we know that $\frac{\partial}{\partial r}(rJ_r) = 0$. This leaves us with $\frac{\partial J_z}{\partial z} = -\frac{\partial \rho}{\partial t} = 0$. This tells us that J_z must be continuous everywhere along the cylinder's surface, including across the interfaces between the helical section and pure axial sections, or else there would be an accumulation of charge over time at these interfaces. The continuity of J_z is illustrated in the vector-arrow representation of the system in Fig. 3.3(b). Summarizing, this means that the axial current I_z in the helical section is equal to the axial current in the axial sections, which is equal to the total current supplied by the generator. Superimposed on this current, in the helical section, is an additional azimuthal current I_θ that is induced along the liner's outer surface. This current is equal in magnitude, but runs opposite to the azimuthal current running in the helical return-current structure. The additional azimuthal current along the liner's outer surface is consistent with the additional magnetic pressure due to the axial magnetic field, B_z, which causes the liner to implode earlier in the DSP case (relative to the SZP case). This additional azimuthal current should not cause any alarm, however, as a similar phenomenon happens in transformers—i.e., the induced current in a secondary winding can exceed the generator current in the primary winding if an appropriate turns ratio and load impedance are used.

The increased current density along the liner's outer surface, $J = \sqrt{J_z^2 + J_\theta^2}$, can also be seen geometrically using Fig. 3.3(a). Note this is equivalent to an increased $B = \sqrt{B_z^2 + B_\theta^2}$ and an increased $p_{mag} = B^2/(2\mu_0) = (B_\theta^2 + B_z^2)/(2\mu_0)$ at the liner's outer surface due to the boundary conditions for the interface between vacuum and a perfect conductor: $B_z = \mu_0 J_\theta$ and $B_\theta = \mu_0 J_z$. Due to the fact that every streamline of $\mathbf{J}$ flowing into the bottom of the helical section must flow out of the top of the helical section, and that $\mathbf{J}$ becomes tilted in the helical section, the streamline density must therefore increase in the helical section. And since

the density of streamlines represents the magnitude of $\mathbf{J}$ ($|\mathbf{J}| = J$), we know that J must be larger in the helical section (along the liner's outer surface) than in the axial sections above and below the helical section. The boundary conditions for an interface between vacuum and a perfect conductor hold in terms of absolute magnitudes as well—i.e., $B = \mu_0 J$, where the directions of $\mathbf{B}$ and $\mathbf{J}$ are perpendicular to one another, but both $\mathbf{B}$ and $\mathbf{J}$ follow helical paths along the liner's outer surface. This is the same thing as saying that the $\mathbf{J} \times \mathbf{B}$ force density is directly radially inwards everywhere, but in the SZP case, there is only one component $|J_z B_\theta|(-\hat{\boldsymbol{r}})$, while in the DSP case, there are two components $|J_z B_\theta|(-\hat{\boldsymbol{r}})$ and $|J_\theta B_z|(-\hat{\boldsymbol{r}})$, where the $J_\theta B_z$ component is an additional inward force density due to the θ-pinch effect.

Regardless of the higher current density, and thus the higher magnetic pressure in the helical section, energy must always be conserved. All of the energy for the additional azimuthal current and axial magnetic field in the helical section must come from the pulsed-power generator. The DSP allows us to concentrate the delivery of magnetic energy to the region where we want it (i.e., to the helical section with the imploding liner). For the special case where, relative to the SZP configuration, we concentrate more magnetic energy total (not just energy density) in the load region of the DSP configuration, the magnetic energy in the connecting transmission lines of the DSP case must be lower to conserve the total energy supplied by the generator. Building up excess magnetic energy, and thus magnetic pressure, in the magnetically insulated transmission lines (MITLs) is not useful for driving the implosion (see Fig. 3.4), since the liner is not located in this region; thus, the ability of the DSP configuration to change the distribution of magnetic energy from the MITL region to the load region is a distinct advantage of using the DSP configuration.

How does this relative redistribution of magnetic energy from the MITL region to the load region come about in the DSP case? Let us compare a helical return-current path (DSP case) with a straight return current path (SZP case), where both return-current paths reside at the same radius. In this case, the helical return path would be more inductive, because the helical path produces more magnetic flux linkage per unit current delivered from the pulsed-power generator, since both B_θ and B_z are generated. This more inductive path would result in a lower peak current delivered from the generator to the load, and thus a lower B_θ, but in some special cases, the increase in B_z at the liner's outer surface can exceed the decrease in B_θ at the liner's outer surface, thus resulting in a higher drive pressure for these special DSP cases.

The pulsed-power generator applies a voltage V to the inductance of the entire vacuum cavity, L, which includes the inductance of both the load region, L_{load}, and the inductance of the connecting MITLs, L_{MITL}. Thus, in total, we have $L = L_{load} + L_{MITL}$. For simplicity we will consider a static (non-imploding) liner. The applied voltage causes a current pulse

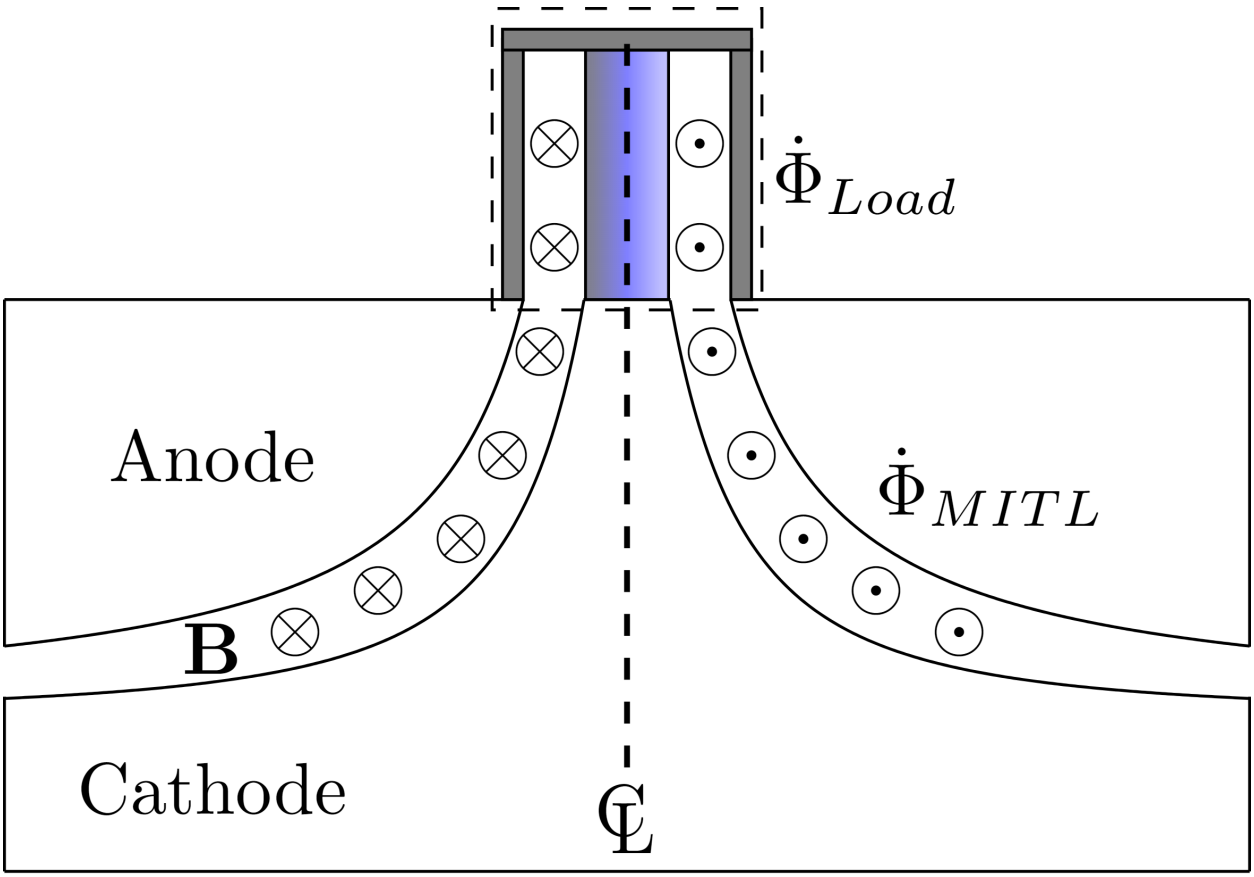

Figure 3.4: An illustration of a MITL with a SZP in the load region. We want to concentrate the magnetic flux in the load region, illustrated here by the dashed box. Magnetic flux in the MITL, the region below the load region, between the anode and cathode, does *not* benefit the experiment. Relative to the SZP case shown here, the DSP case can be designed to preferentially concentrate more total magnetic flux in the load region by trading some of the B_θ flux in the MITL for B_z flux generated only in the load region.

to begin rising at a rate of $\dot{I} = V/L$, which is just Faraday's law for describing the rate of increasing magnetic flux in each vacuum region due to the applied voltage, or $V = L\dot{I} = \dot{\Phi} = \dot{\Phi}_{load} + \dot{\Phi}_{MITL}$. Note that $\dot{\Phi}$ is directly related to $\dot{I}$ and that we are applying a minus sign to Faraday's law to simplify the discussion—i.e., so that a positive voltage drives a positive increase in current and a positive increase in magnetic flux filling the vacuum regions of the load and MITLs. The smaller $\dot{I}$ in the helical case (due to the larger overall L) means that $\dot{\Phi}_{MITL}$ will be smaller in the helical case, and thus $\dot{\Phi}_{load}$ will be larger in the helical case, since more of the generator's total $V = \dot{\Phi}_{load} + \dot{\Phi}_{MITL}$ is applied to the load. This means that in this particular case, where the DSP return-current radius is equal to the SZP return-current radius, more magnetic energy is delivered to the load region of the DSP case. Also note that the total $\dot{\Phi}_{load}$ has both azimuthal and axial components ($\dot{\Phi}_{load,\theta}$ and $\dot{\Phi}_{load,z}$) due to $\dot{B}_\theta$ and $\dot{B}_z$.

Now, in this particular comparison between a straight return-current path and a helical return-current path at the same radius, the total $\dot{\Phi}_{load}$, and thus the total magnetic energy delivered to the load region is larger in the helical case, while the volume of the helical load region, is the same as that in the straight return-current case (since the same return-current radius is used in both cases). Thus, the spatially-averaged flux density (or, equivalently, the spatially-averaged magnetic field strength B) in the load region is higher in the helical case, which means that the spatially-averaged magnetic energy density (or, equivalently, the spatially-averaged magnetic pressure $p_{mag} = B^2/(2\mu_0)$) in the load region is higher in the helical case. However, for comparing drive pressures, we must evaluate and compare the local magnetic flux density (or, equivalently, the local magnetic field strength B and thus the local magnetic drive pressure p_{mag}) at the liner's outer surface. To do this, we recall that the flux associated with $B_\theta(r)$ is preferentially distributed near the liner's outer surface, since $B_\theta(r) = \mu_0 I/(2\pi r) \propto 1/r$, while the flux associated with $B_z = \mu_0 In =$ constant is distributed uniformly.

Whether the total drive pressure is higher or lower for a particular DSP case relative to the corresponding SZP case, where both cases use the same return-current radius, comes down to the specifics of the configuration—e.g., the return-current radius relative to the liner radius, the strength (or helicity) of the DSP return-current structure (basically the turns per unit length, n), and the ratio L_{load}/L_{MITL}. These comparisons become quite complicated, and currently there is no convenient analytical way of expressing where the transition occurs (where a DSP case has a higher or lower drive pressure relative to a SZP case with the same return-current radius).

Relative to the SZP case, the DSP case can cause a liner to implode earlier and thus stagnate earlier, even when the same return current radius is used. However, as we saw above,

the same return-current radius was not used in the SZP and DSP cases tested on COBRA. In our COBRA experiments, the return-current radii selected for the DSP cases were smaller than the return-current radius used for the SZP case. This was done to equalize L_{load} between the cases. With approximately equal values for L_{load}, the total current I delivered to the load from the generator is approximately the same in all the cases [at least prior to the start of significant radial motion (implosion) of the liner]. This means that I_z is approximately the same in all cases, but the DSP cases have an additional I_θ [consistent with an additional J_θ and B_z, and thus providing $p_{\text{mag,DSP}} = (B_\theta^2 + B_z^2)/(2\mu_0) > p_{\text{mag,SZP}} = B_\theta^2/(2\mu_0)$]. This means that in our experiments, the DSP cases should implode earlier. In Chapter 4, we will analyze implosions trajectories for the various cases, each with roughly equal L_{load}, to determine if the DSP cases due in fact implode earlier than the SZP case.

3.3 Liner Design

As discussed in Chapter 2, the stabilizing effect of the DSP is tied to the liner thickness, for all but the most unstable modes. Not only will the liner thickness change how the DSP stabilizes the implosion, but it will also change the early-time ablation dynamics. The liners used in our experiments are extremely thin; thinner than their electrical skin depth. The skin depth is how far into a material a time-varying current can penetrate, it can be determined by:

$$\delta_{skin} = \sqrt{\frac{4\rho\tau_r}{\pi\mu}}, \tag{3.2}$$

where ρ is the resistivity of the conductor, τ_r is the rise time of the current, and μ is the permeability of the conductor. For aluminum on COBRA, the skin depth is approximately 50 µm, which is quite comparable to the skin depth of a beryllium liner on Z, which is approximately 60 µm.

An important parameter for characterizing the liner's susceptibility to MHDI feedthrough is the liner's initial aspect ratio, $A_{r0} \equiv r_{\ell 0}/\delta_0$, where $r_{\ell 0}$ is the initial radius of the liner's outer surface, and δ_0 is the liner's initial wall thickness. MagLIF liners on the Z facility typically use $A_{r0} \approx 6$, where $r_{\ell 0} \approx 3$ mm, and $\delta_0 \approx 500$ µm; larger A_{r0} liners are more susceptible to MHDI, while lower A_{r0} liners result in slower implosion velocities. Similarly, experiments designed to study dynamic material properties use low aspect-ratio liners ($A_{r0} \approx 2$–4) to mitigate MHDI and maintain sample uniformity under compression [20, 21]. For the low-A_{r0} liners used on the Z facility, the wall thickness is greater than the electrical skin depth, $\delta_e \sim 100$ µm. Thus, the MHDI initially forms near the liner's outer surface and works its

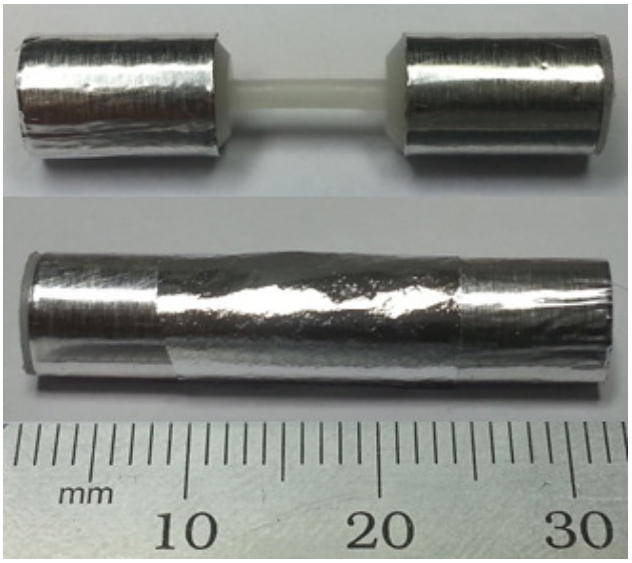

Figure 3.5: Photos of the liner support structure (top) and the support structure with the liner wrapped around it (bottom). Photo by David Yager-Elorriaga.

way toward the liner's inner surface throughout the implosion [62, 68].

To study the physics of MagLIF-like liner implosions at 1 MA, thin-foil liners are typically used because 1-MA machines lack the energy to implode massive, thick-walled MagLIF liners. For our COBRA experiments, 650-nm-thick aluminum foil was the chosen liner material. The use of such thin foils allows a liner with $r_{\ell 0} \sim 3$ mm to be imploded in $\sim$100 ns (i.e. a similar implosion trajectory to a MagLIF implosion). Since MRTI growth is governed by the acceleration history of the implosion, a MagLIF-relevant implosion trajectory should result in MagLIF-relevant MRTI growth. The initial liner radius was 3.175 mm for all cases. Because the foils are so thin, the liners are not self-supporting. Thus, following Ref. [69], the liner loads were assembled by wrapping rectangular foils onto a plastic dumbbell-shaped support structure (see Fig. 3.5). The ends of the dumbbell have a diameter that matches the desired initial diameter of the liner, while the connecting rod in the central portion of the dumbbell has a diameter that is made as small as possible to allow as much implosion convergence as possible. For our experiments, the central portion of the dumbbell (the on-axis support rod) had a radius of 0.65 mm, allowing for a convergence ratio of up to 4.9. However, the maximum convergence ratio observed in our experiments (for the liner's outer surface) was approximately 2. The thin foils are not nearly as robust as the freestanding liner used in MagLIF experiments on Z. They are easily crinkled, resulting in larger seed perturbation amplitudes. Furthermore, there is a thin seam where the rectangular foil, wrapped into a cylindrical shell, overlaps itself. This seam was positioned azimuthally to minimize interference with imaging diagnostics and instability measurements.

Previous thin-foil experiments have already demonstrated relevancy to MagLIF. For example, thin-foil experiments at 650 kA have found both $m \approx 0$ instability structures for SZP cases with no applied axial field and more stable $m \approx 2$ helical structures for SZP cases with an externally applied $B_{z0} = 2$ T. Note that with a thickness of roughly 500 nm, these thin foils should be highly susceptible to instability feedthrough (i.e., they have an initial liner aspect ratio, A_{r0}, of approximately 6,000, where A_{r0} is defined as the liner's initial outer radius divided by the liner's initial wall thickness). However, because the electrical skin depth is initially much greater than the foil thickness, ohmic heating causes the thin foils to rapidly expand to a wall thickness of 100–1000 µm prior to the implosion [70, 71], thus lowering the effective A_{r0} to 3–30, which is more in line with the initial aspect ratios used for MagLIF experiments on the Z facility (A_{r0}=6). (Note that the liners on Z have wall thicknesses of approximately 500 microns, which is greater than the electrical skin depth. This results in the liners on Z actually compressing up prior to imploding, which can lead to an effective A_{r0} of approximately 10.)

Not only will the thickness of the liner change how instabilities feed through the liner, but also the degree of stabilization the DSP has. This is due in part to how much magnetic shear can exist in the liner itself. By magnetic shear we mean how much the magnetic field lines rotate as you move radially inward or outward, for a given moment in time. For an infinitesimally thick liner, minimal magnetic shear can exist and the majority of the stabilization would need to come from the rotation of the magnetic field at the liner's outer surface. How much our liner expands is a bit ambiguous, which can make implementing some of the theory tricky. This point will be further discussed in Chapter 4, when we analyze our experimental growth rates and compare them to the V&S theory of Ref. [7].

3.4 Diagnostics

Now that we know what our experiment looks like and how it is driven, how will we generate data and attempt to understand these new implosion dynamics? In this subsection, an overview of the diagnostics used to probe our experiments will be presented. These include a Rogowski coil for measuring current, micro B-dot probes for measuring magnetic fields, a fast framing camera for imaging the visible light emitted from the liner, and extreme ultraviolet (XUV) cameras for imaging the UV light emitted from the liner.

3.4.1 Measuring Current

Current is one of the most important parameters to measure in a pulsed power experiment. The measurement can be made using B-dot probes as well as Rogowski coils. A Rogowski

coil around the cathode provides the most direct measurement of current on most pulsed power drivers.

Magnetic induction is the production of an electromotive force (EMF) across a conductor due to its interaction with a magnetic field. This phenomena can be understood by examining both Faraday's and Lenz's laws. Faraday's law states that any changing magnetic field through a loop of conducting material (i.e. a coil of wire) will cause a voltage or EMF to be induced. Mathematically, it is given by:

$$\mathcal{E} = -N\frac{d\Phi_B}{dt}, \tag{3.3}$$

where N is the number of turns or windings the conductor has, $\mathcal{E}$ is the EMF or induced voltage and Φ_B is the magnetic flux. The minus sign in the equation comes from Lenz's law which states that the current induced in the conductor by a changing magnetic field will always create a magnetic field that opposes the original field. More generally, this behavior is given by the Maxwell-Faraday equation:

$$\oint_{\partial\Sigma} \mathbf{E} \cdot d\boldsymbol{\ell} = -\frac{d}{dt}\int_{\Sigma} \mathbf{B} \cdot d\mathbf{A} \tag{3.4}$$

where Σ is the surface area bounded by the contour $\partial\Sigma$, $d\boldsymbol{\ell}$ is an infinitesimal vector element of the contour $\partial\Sigma$, and $d\mathbf{A}$ is a vector normal to an infinitesimal surface area element within the larger surface area Σ. While these are basic equations typically seen when first learning about solenoids in freshman E&M, they are important concepts since they are how magnetic induction can be leveraged to produce signals. Rogowski coils are essentially N-turn solenoids (MAIZE's coil uses around 20 in our coil). These solenoids are then wired into coaxial cables so the induced voltage can be measured by an oscilloscope.

The sensitivity or response of the Rogowski coil depends on variables other than the dB/dt as seen in the following equation (essentially a restatement of Eq. 3.3):

$$V = \pm NA\frac{dB}{dt}, \tag{3.5}$$

where N is the number of turns or loops the Rogowski coil has, and A is the cross-sectional area bounded by each loop (assuming each loop is the same). The $\pm$ is determined by the direction of the magnetic field and orientation of the Rogowski coil.

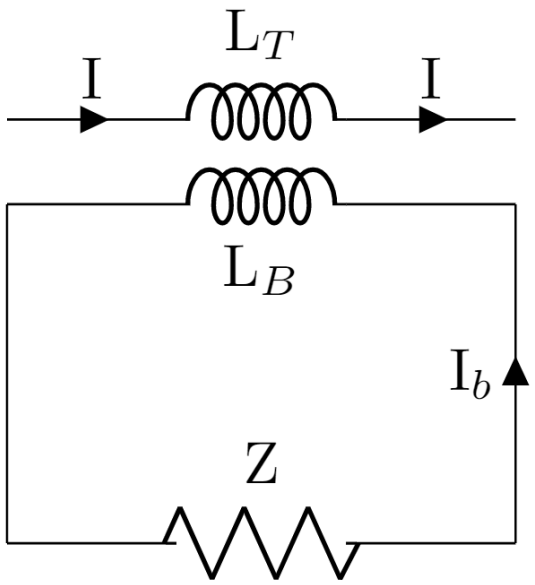

Figure 3.6: A circuit representation of how a B-dot probe generates voltage. On top is a transmission line with some inductance L_T. A current runs along this transmission line, which we would like to determine by measuring the magnetic field generated by this current. Underneath is the B-dot probe, with some inductance L_B and impedance Z. The mutual inductance between the two circuits causes a voltage or current to be induced in the B-dot probe, when a voltage or current pulse runs along the transmission line.

3.4.2 Measuring Magnetic Fields

Magnetic fields are important measurements to make in plasma experiments and are of particular interest to us, since our plasma stabilization scheme relies on generating two components of magnetic fields. These measurements can be made using B-dot probes, proton radiography, Zeeman spectroscopy, or Faraday rotation. We will be making use of B-dot probes to make measurements in our experiments.

In the previous subsection, how to make use of magnetic induction to make current measurements with a Rogowski coil was discussed. B-dot probes operate in very much the same manner, they are N-turn solenoids.

Another way to think about how B-dot probes make measurements is through a simplified circuit model. The loops of a B-dot probe can be thought of as an inductor, which then has a mutual inductance with a transmission line, for example where we would like to measure the current running along this transmission line. Through this mutual inductance, a voltage is induced and sent down a cable with some impedance to an oscilloscope. From this voltage

pulse, the current from the transmission line can be calculated. A B-dot's frequency response is determined by the time constant:

$$\tau = \frac{L}{R_0}, \tag{3.6}$$

where L is the inductance across the B-dot probe and R_0 is the resistance connected across its output (Z in Fig. 3.6). The inductance of the B-dot probe can be estimated assuming it is a simple solenoid:

$$L = \frac{\mu_0 N^2 A}{l}, \tag{3.7}$$

where l is the length of the solenoid. One constraint when designing B-dot probes is that the magnetic flux needs to be able to quickly penetrate the coil and not be excluded by opposing currents running in the coil itself [72]. This is equivalent to stating that the ratio L/R_0 must be small, so what happens when L/R_0 is large? As R_0 goes to zero, the signal becomes proportional to B instead of dB/dt. This is known as a self-integrating B-dot probe.

3.4.3 Visible Light Imaging

Imaging a plasma can be a challenging measurement to make since there are many factors to take into account, like the spectrum of light being imaged. Visible light imaging was a workhorse diagnostic for our experiments on COBRA since we are particularly interested in the dynamics of the plasma implosion. We will be primarily making use of visible light (400-700 nm wavelengths) due to the response curve of the ICCD in our camera. At Michigan, and at Cornell, an Invisible Vision Ultra UHSi 12/24, 12-frame fast framing camera is used to image plasma dynamics. The exposure time for each of the 12 frames can be set to as low as 5 ns, although for our experiments, 10 ns was used, with an inter-frame time of 0 ns (i.e. the time between the starts of each frame is 10 ns and the time between the start of one frame and the end of the next frame is 0 ns).

While we will just be looking at visible-light self-emission in this experiment, at Michigan we can couple laser light into the camera to get shadowgraphy images. The optical setup is shown in Fig. 3.7, which allows the 532-nm laser light to enter and exit the optical cavity through a 95/5 (transmission/reflection) beamsplitter. At a given point in space, each subsequent light pulse is delayed by 15 ns, which is set by the approximately 15-ft optical path length of the cavity. As the initial pulse enters the cavity, BS_2 (the first beamsplitter of the cavity) sends 95% of the beam energy to a beam dump, and BS_3 (the second beamsplitter of the cavity) picks off another 5% to send to the target. The intensity of each subsequent pulse is further reduced by about 10%. Using an intensified CCD camera, however, easily overcomes this substantial reduction in laser energy. It is necessary to configure the beamsplitters this

way in order to minimize the pulse-to-pulse intensity variation. If BS_2 were reversed, and it allowed 95% of the light to enter the cavity, each subsequent pulse would be 95% less intense than the previous pulse. Future diagnostics will use the "dumped beam" for interferometry and Faraday rotation measurements. The fast 12-frame camera is synchronized to capture the series of laser pulses directed from the optical cavity.

The stability of the cavity on MAIZE (shown in Fig. 3.7) may be calculated using the ray transfer (or ABCD) matrix of the overall system [73]. Each optical element in the system (e.g. mirrors, lenses, and the free space between the optics) has its own ray transfer matrix. For example, the transfer matrix for a curved mirror is given by

$$M_{cm} = \begin{pmatrix} 1 & 0 \\ -\frac{2}{R_e} & 1 \end{pmatrix}, \tag{3.8}$$

where R_e is the effective radius of curvature in the tangential plane. The matrices for each element are then multiplied together to result in a single ray transfer matrix for the system, M. Note that the order of the matrix multiplication is important, since matrix multiplication is non-commutative. From the product of the matrices, an eigenvalue equation may be solved to yield:

$$\lambda_{\pm} = g \pm \sqrt{g^2 - 1}, \quad g = \frac{tr(M)}{2}, \tag{3.9}$$

where $\lambda_{\pm}$ are the eigenvalues, g is the stability parameter, and $tr(M)$ is the trace of the system transfer matrix M. The condition for stability is $g^2 \leq 1$ [73]. The two concave mirrors of the system each have a radius of curvature of 1000 mm, and they are separated by 1003 mm of free space. Upon multiplying the matrices together for every element in Fig. 3.7 (including the free space between every pair of elements in Fig. 3.7), we obtain $g^2 = 0.965$, and thus the system is stable.

A plot of MAIZE's stability parameter as a function of the distance between the concave mirrors is shown in Fig. 3.8. While the plot shows a wide range of distances over which the concave mirrors can be placed, their separation should be as close as possible to 1000 mm to help preserve the original beam size. The farther apart the concave mirrors are placed, the smaller each subsequent beam in the optical cavity becomes. Another way of looking at this is that since this setup makes use of two concave mirrors separated by a distance of $\gtrapprox 2f$, where $f \approx R_e/2$ is the focal length of the concave mirrors, the cavity is in a region of optical stability.

An alternative to using a pulsed laser coupled to an optical cavity for 12-frame shadowgraphy is to simply use a continuous-wave (CW) laser, which removes the need for the optical cavity. This was recently implemented on MAIZE [74], and it allows to easily change the

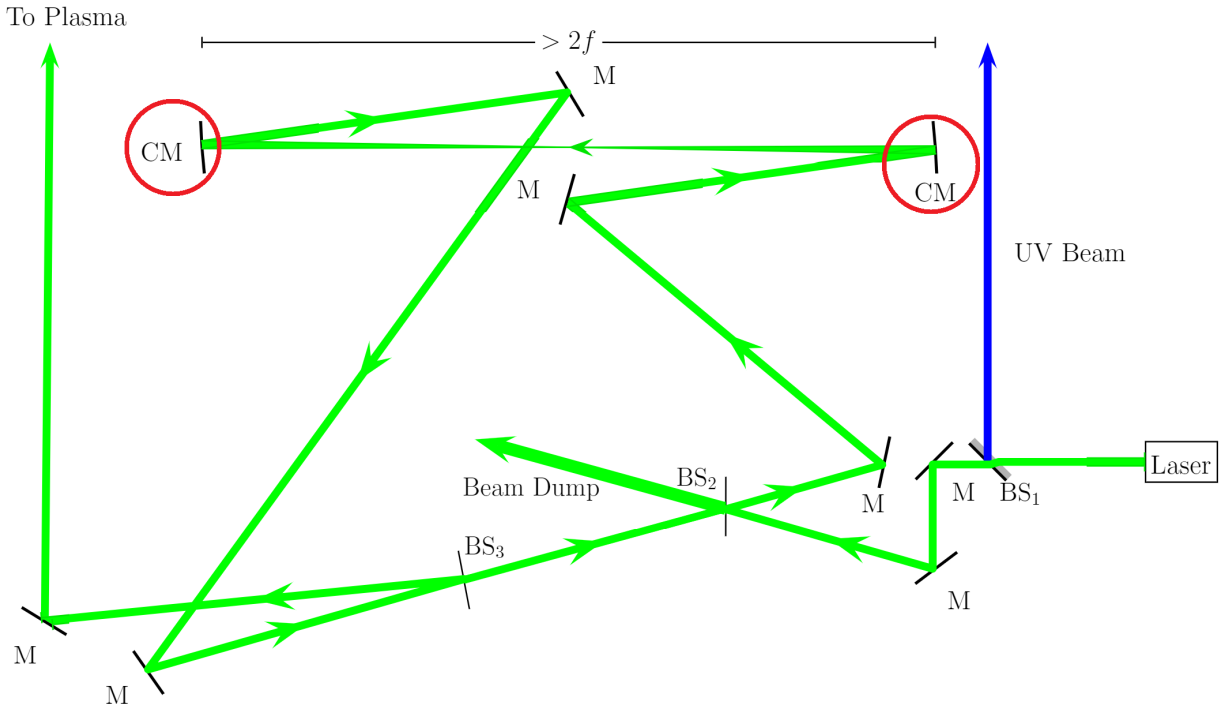

Figure 3.7: Optical setup of the 12-frame shadowgraphy system on MAIZE. This system, presented in Ref. [5], is a modified version of the system presented in Ref.[6]. The beamsplitters (BS), planar mirrors (M), and concave mirrors (CM, circled in red) are indicated in the figure. This optical cavity configuration allows for 12 or more beams (delayed in time relative to one another) to share the same optical axis while maintaining stability.

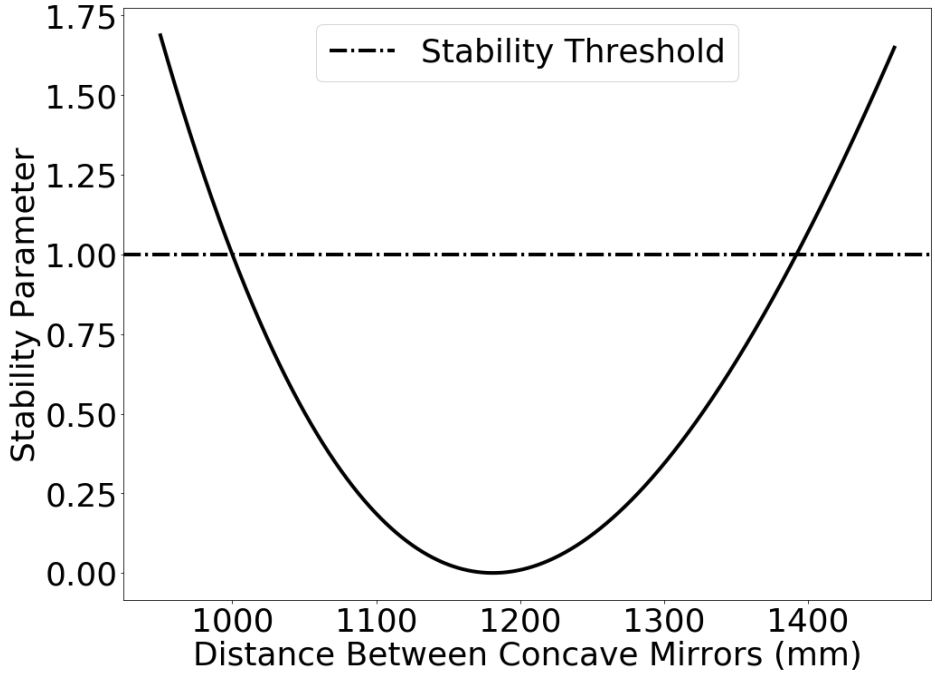

Figure 3.8: The stability parameter g of the optical cavity plotted as a function of the distance between the concave mirrors. The threshold for stability ($g^2 \leq 1$) is also plotted.

inter-frame times of the 12-frame (or even 24-frame) laser shadowgraphy system. Note that with a pulsed laser coupled to an optical cavity, changing the inter-frame times requires a lengthening of the cavity's optical path, which can be exceedingly cumbersome. However, there are advantages to using a pulsed laser coupled to an optical cavity for many experimental situations. First, the intensity is typically much higher for pulsed lasers when compared to CW lasers. This is an important factor to consider when the plasma is strongly radiating at the laser wavelength (as in a typical COBRA or MAIZE experiment). Without sufficient laser intensity, the self-emission of the plasma will dominate the image, greatly reducing the shadowgraphy contrast. Second, pulsed lasers are potentially safer for the ICCD camera. For example, if the camera shutter is inadvertently left open, a CW laser could damage the camera's ICCD, as the deposited laser energy will accumulate over time. To mitigate the risk of a CW laser damaging the ICCD, multiple optical shutters should be used for redundant protection (i.e., in case one of the shutters fails to close, there are other shutters which hopefully do close). Finally, the time resolution of a shadowgraphy system is determined by whichever is shorter, the laser pulse length or the frame exposure duration of the camera. On MAIZE, the fast-framing camera is capable of 5-ns exposures, while the laser has a 2-ns pulse duration. With a shorter-pulse laser, even better time resolution could be achieved.

3.4.4 UV Light Imaging

In addition to the visible self emission imaging, two time-gated, four-frame XUV pinhole cameras were used in the COBRA experiments. For these experiments the system used 200-µm pinholes placed approximately halfway between the load region (the object plane) and the camera detector (the image plane). The camera's detector is sensitive to photons above ∼7 eV [75]. Each of the four frames has a variable 5–20 ns exposure, with a 10-ns inter-frame delay. Additionally, the lines of sight of the two XUV cameras are roughly perpendicular to the optical self emission setup, so two different regions of the liner can be imaged simultaneously. This will help when trying to correlate instability structures that wrap around the imploding cylindrical liner.

Following Ref. [75], the geometric resolution of the system is given by

$$L_{\text{geo}} = d\left(1 + \frac{p}{q}\right), \tag{3.10}$$

where d is the diameter of the pinhole, p is the object-to-pinhole distance, and q is the pinhole-to-image distance. For the system on COBRA, $d = 200$ µm, $p = 0.53$ m, and $q = 0.38$ m, which gives $L_{\text{geo}} = 478$ µm. The inherent resolution of the microchannel plate (MCP) detectors in the XUV camera is ∼50 µm. The system's geometric resolution can be improved by switching to smaller pinholes (d), decreasing the object-to-image distance (p), and/or increasing the pinhole-to-image distance (q). However, because of diffraction limitations, decreasing the pinhole size also decreases the number of UV photons that reach the camera detector. For example, the diffraction limited spatial resolution is given by

$$L_{\text{diff}} = 1.22\frac{\lambda p}{d}, \tag{3.11}$$

where λ is the wavelength of the imaging photons. For 200-µm pinholes, $L_{\text{geo}} \geq L_{\text{diff}}$ only when $h\nu \geq 8.4$ eV. For 50-µm pinholes ($L_{\text{geo}} = 120$ µm), this threshold instead occurs at $h\nu \geq 33.5$ eV. If the only photons being generated by the plasma are 8.3-eV photons, then the 50-µm-pinhole system resolution will be limited (and actually degraded relative to the 200-µm-pinhole case) by diffraction (i.e., $L_{\text{system}} = L_{\text{diff}} = 478$ µm); however, if the plasma is hot enough to be generating significant amounts of 33.5-eV photons, then the better geometric resolution might be accessible (i.e., $L_{\text{system}} = L_{\text{geo}} = 119$ µm).

Finally, in Fig. 3.9, we illustrate how all of these diagnostics are oriented with respect to one another and the liner.

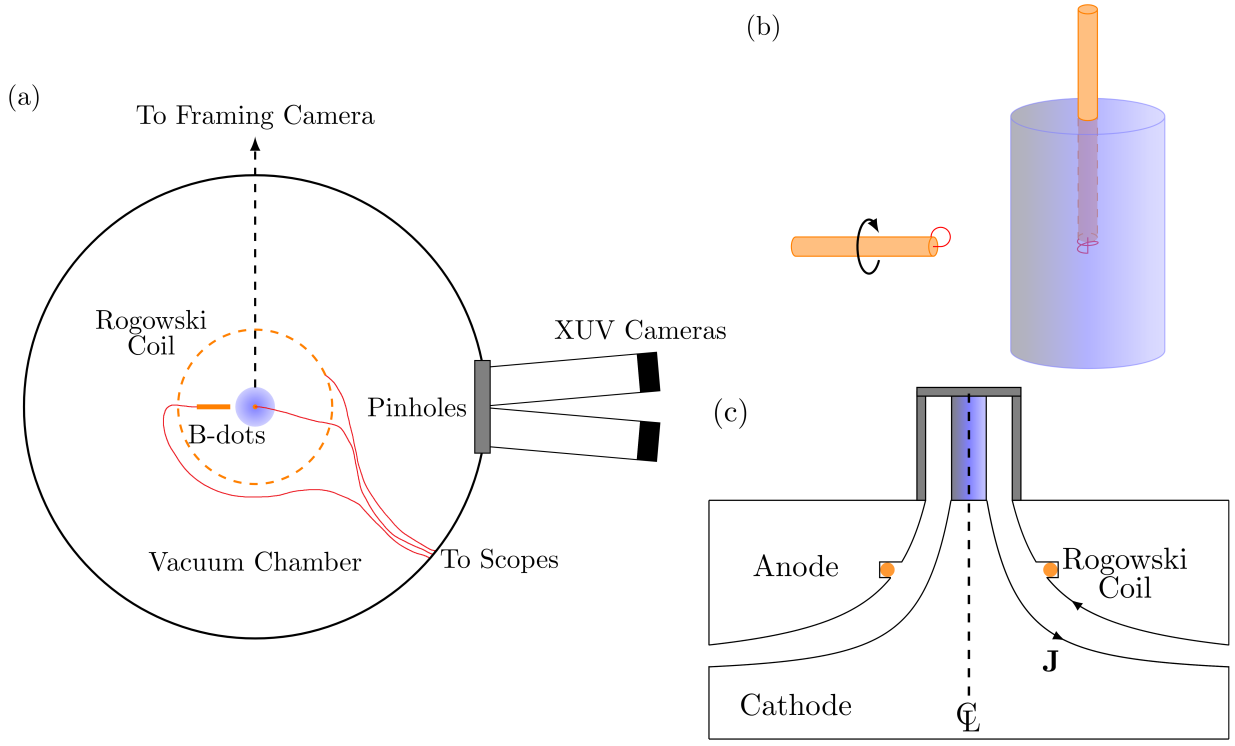

Figure 3.9: Illustrations of the experimental setup used on COBRA, showing the orientation of diagnostics with respect to the liner. (a) A top down view that shows how the Rogowski coil (dashed orange circle), pinholes (gray box), XUV cameras (black boxes), and the line of sight to the framing camera (black dashed arrow) are arranged. The liner is in the center in blue, red lines show the electrical connections to the Rogowski coil and to the micro B-dots probes (orange rectangle and orange circle). (b) A side-on view of the orientation of the micro B-dot probes with respect to the liner. The on-axis B-dot probe is used to measure the axial magnetic field inside the liner, while the outer B-dot probe can be used to measure either the axial or the azimuthal component of the magnetic fields, depending on the probe's orientation. In this illustration, the outer probe is oriented to measure azimuthal component. (c) A cross section of the power feed, with the liner in blue, a SZP return-current structure in grey, and the Rogowski coil in orange.

CHAPTER 4

Results

In this Chapter, results from two experimental runs on COBRA are presented. Magnetic field measurements both inside and outside the liner are shown, along with comparisons to the expected field strength based on simulations and current measurements. Next, XUV images are presented and helical instabilities are tracked and compared to the magnetic polarization angle. Visible self-emission images are also presented and used to track instability growth. Current waveforms, and their relevancy to power flow, are discussed along with particle in cell (PIC) simulations of the power feed.

4.1 Magnetic Field Measurements

As discussed in Chapter 3 (see Fig. 3.9), the axial magnetic fields generated by the return-current structures were measured with a micro B-dot probe [76] placed 3 mm radially outward from the liner surface. The drive current was measured using a Rogowski coil in COBRA's power feed. Examples of these measurements are presented in Figs. 4.1 and 4.2 (note that the axial magnetic field measurements made inside the liner, which are also presented in these figures, and the reference to t_{freeze} in these figure captions, are discussed further below in this section).

The axial field measurements agree reasonably well with the values predicted by CST design simulations. The low-field experiments had measured peak values of 3.5 ± 2.1 T, while the mid-field experiments had measured peak values of 11.5 ± 5.3 T (see Tables 4.1 and 4.2). Unfortunately, the probe failed on the only high-field shot. Note that the $B_z(t)$ waveform in Figs. 4.1 and 4.2 matches the drive current waveform very well during the rising edge of the pulse. After peak current, however, the micro B-dot probe appears to short out (as is indicated by this time-integrated signal not returning to zero). This behavior was consistent across other shots as well. During post-shot inspections, it was discovered that the dielectric insulator that covers the probe was compromised, which may explain the probe failures after peak current.

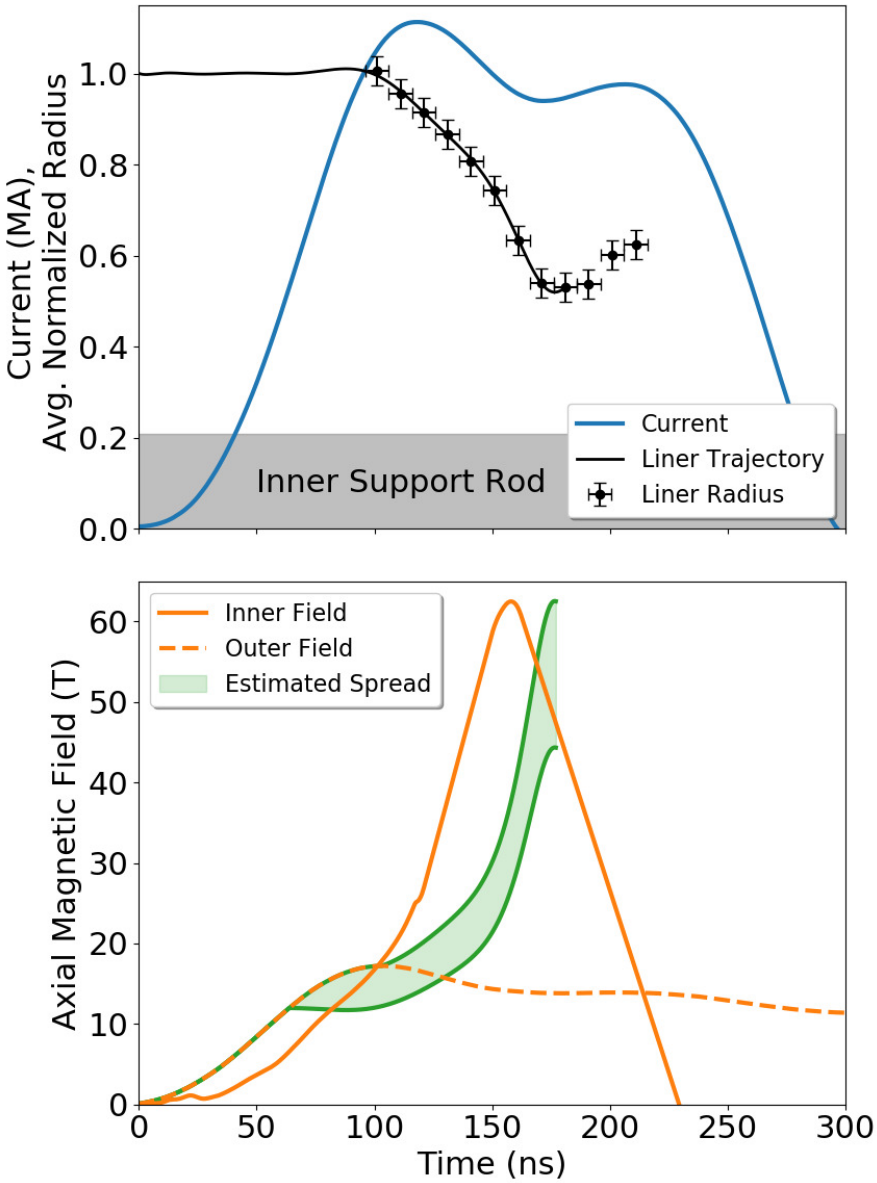

Figure 4.1: Experimental data from shot 5396, which was a 14-T DSP shot with COBRA in short pulse mode. (Top) Measured liner radii and drive current, along with a fit to estimate the liner's trajectory. The radius of the inner support rod is also shown. (Bottom) Axial magnetic field values both inside and outside the liner are plotted along with an estimate of how much the inner axial field should increase, based on the minimum and maximum values of t_{freeze}, measured imploding liner radii (of the liner's outer surface), and measured outer axial magnetic field. Note that the signal for the inner axial field measurement clipped the scope so the peak value is lower than it should be.

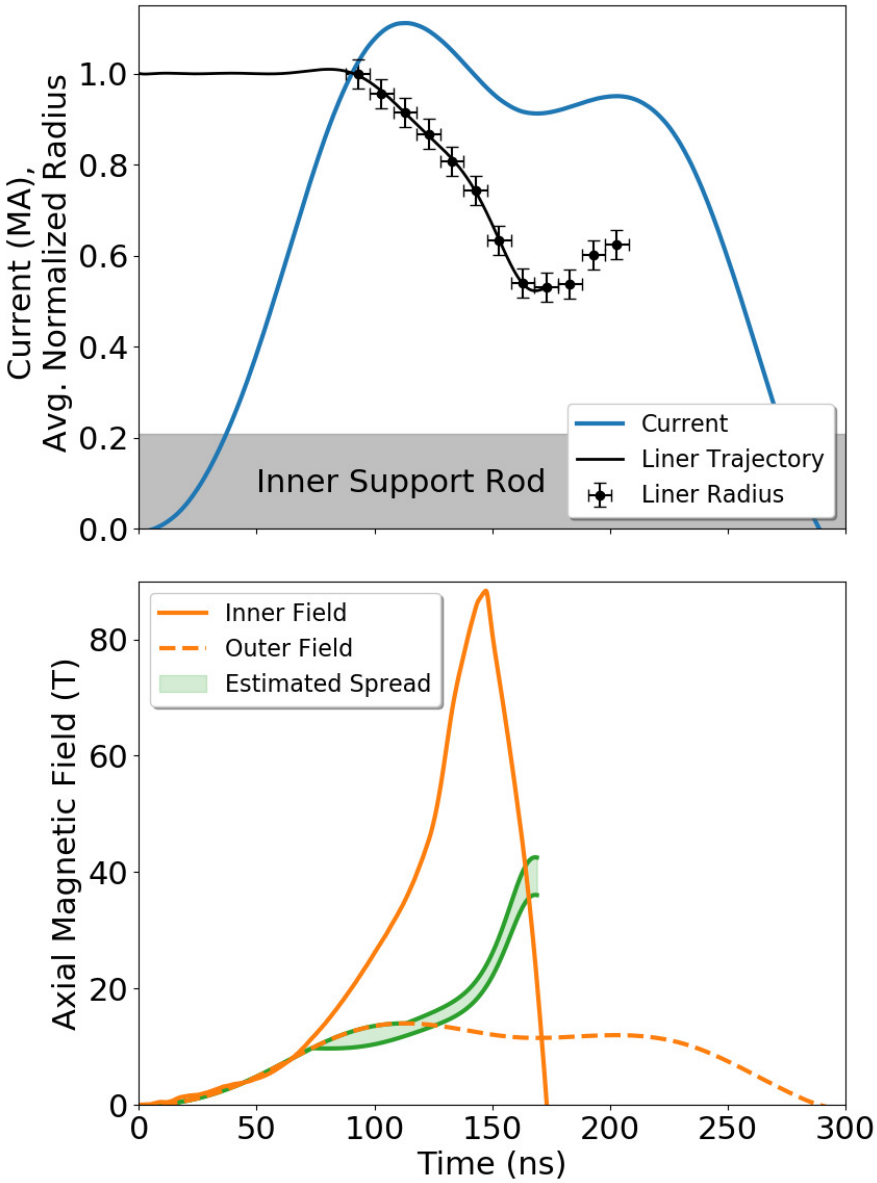

Figure 4.2: Experimental data from shot 5397, which was a 14-T DSP shot with COBRA in short pulse mode. (Top) Measured liner radii and drive current, along with a fit to estimate the liner's trajectory. The radius of the inner support rod is also shown. (Bottom) Axial magnetic field values both inside and outside the liner are plotted along with an estimate of how much the inner axial field should increase, based on the minimum and maximum values of t_{freeze}, measured imploding liner radii (of the liner's outer surface), and measured outer axial magnetic field. Note that the signal for the inner axial field measurement clipped the scope so the peak value is lower than it should be.

Table 4.1: Peak current and magnetic field strength data from the first COBRA run.

Shot No.	Peak Current (MA)	Peak Axial Magnetic Field (T)
SZP shots start		
5185	1.16	-
5186	1.11	-
5188	1.20	-
avg	1.16 ± .045	-
Mid-field DSP shots start		
5189	1.20	-
5190	1.22	14.1
5192	1.05	-
5193	1.21	8.4
5194	1.21	18.7
5195	1.08	18.0
avg	1.16 ± .075	14.8 ± 4.72

Table 4.2: Peak current and magnetic field strength data from the second COBRA run.

Shot No.	Peak Current (MA)	Outer Axial Field (T)	Inner Axial Field (T)
SZP shots start			
05389	0.90	-	-
05391	0.85	-	-
05393	1.03	-	-
05394	1.06	-	-
Avg.	0.96 ± .100	-	-
Mid-field DSP shots start			
05396	1.13	17	>62
05397	1.12	-	84
05398	1.00	6	128
05399	0.97	8	-
05400	1.14	-	-
05402	1.13	-	-
Avg.	1.08 ± .076	10.3 ± 5.86	91.3 ± 33.6
Low-field DSP shots start			
05403	1.12	5	73
05404	1.18	2	29
Avg.	1.15 ± .042	3.5 ± 2.12	51 ± 31.1
Applied B_z shots start			
05405	1.13	-	-
High-field DSP shots start			
05407	1.17	-	-
05408	1.19	-	82
Avg.	1.18 ± 0.014	-	-

Considering for a moment an axially premagnetized, SZP-driven liner implosion (e.g., a standard MagLIF configuration), ideal flux compression of the axial magnetic field trapped inside the imploding liner (e.g., in the fuel region of MagLIF) can be described by

$$B_{z,in} = B_{z0}\left(\frac{R_{in}(0)}{R_{in}(t)}\right)^2, \tag{4.1}$$

where B_{z0} is the strength of the preimposed axial magnetic field, and R_{in} is the inner radius of the liner. Of course, we are interested in DSP cases, not SZP cases, so why this formulation of interest? The answer is that with our thin-foil liner implosions, some drive field penetrates the liner interior and is then flux compressed by the imploding liner. The reason why this happens is because early in time, the liner foil material is ohmically heated rapidly. This causes the conducting metal to rapidly melt, vaporize, and then ionize into a conducting plasma. During the liner's transition to plasma, the unionized liquid-vapor state is highly resistive, thus the drive field can penetrate rapidly during this period. This happens early in the experiment, when the drive current is still low. Once the liquid-vapor state strongly ionizes into a conducting plasma, the external drive field becomes more excluded from the liner's interior. However, whatever flux penetrated the liner's interior during the brief liquid-vapor state is now trapped within the liner and can be flux compressed by the imploding liner. The time at which the liner ionizes into a strongly conducting plasma, thus separating/isolating/detaching the injected flux inside the liner from the external drive field, is the time we call t_{freeze} (see Figs. 4.1 and 4.2).

The magnetic Reynolds number will be used to try and determine the time t_{freeze}, when the liner goes from resistive to conducting—i.e., when it goes from allowing new flux from the generator to penetrate the liner interior to excluding new flux from the generator from penetrating the liner interior. The magnetic Reynolds number is typically defined as:

$$R_m = \frac{UL}{\eta}, \tag{4.2}$$

$$\eta = \frac{1}{\mu_0 \sigma_0}, \tag{4.3}$$

where U is a characteristic flow velocity, L is a characteristic length scale, η is the magnetic diffusivity, and σ_0 is the electrical conductivity. The magnetic Reynolds number gives an estimate of the effect of the advection of the magnetic field due to the material's motion (in this case the motion of the liner plasma) relative to the magnetic diffusion into the material. For $R_m \ll 1$ the material is diffusion dominated, and for $R_m \gg 1$ the material is advection dominated (i.e., where the plasma goes, the field goes, and vice versa). By estimating when

the liner makes this transition, we can determine how much magnetic flux has been frozen into the liner, and therefore how much it will be compressed up. We will be using $R_m = 1$ as the threshold for when the liner makes the transition to try and estimate a t_{freeze}. Then we can apply Eq. 4.1 to whatever flux is trapped inside the liner by the time of t_{freeze}.

For our calculations we will be using two different models of conductivity, the Spitzer model [77, 78] and the Lee More model [79], in the nondegnerate limit (this is to avoid having to compute any Fermi-Dirac integrals). Electrical conductivity for the two models is given by:

$$\sigma_S = \frac{3}{4\sqrt{2\pi}} \frac{(4\pi\epsilon_0)^2 (k_b T_e)^{3/2}}{Ze^2\sqrt{m_e} ln\Lambda} \tag{4.4}$$

$$\sigma_{LM} = n_e e^2 \tau A^\alpha / m_e, \tag{4.5}$$

where σ_S is the conductivity given by the Spitzer model and σ_{LM} is the conductivity given by the Lee More model. The parameters of electron relaxation time, τ, and A^α, in the nondegenerate limit are given by:

$$\tau = (k_b T_e)^{3/2} \frac{4\sqrt{2\pi}}{3} (4\pi\epsilon_0)^2 / Ze^4 n_i ln\Lambda, \tag{4.6}$$

$$A^\alpha = \frac{32}{3\pi}, \tag{4.7}$$

$$n_e = Z n_i. \tag{4.8}$$

Before continuing, a few notes on this implementation of the Lee More model should be discussed. First, Desjarlais added important contributions to the Lee More model [80, 81] that we are ignoring for simplicity. Second, while the Lee More model can account for electron and ion temperature differences, we are not considering effects from the ions (effectively we are saying that the ions are cold compared to the electrons). These effects only come about when using the Lee More model to calculate the Coulomb logarithm, $\ln\Lambda$, which varies only slightly in this case (values between 15-20 for the most extreme cases). Additionally, this parameter does not strongly affect the conductivity. Finally, for a singly ionized plasma, the Lee More model has no density dependence since the electron and ion densities will be the same.

Based on PERSEUS (an extended MHD code [82]) simulations of thin-foil liners, we estimate that in the bulk plasma, electron temperatures are in the range of eVs at the start of the implosion and 100's of eV at stagnation, shown in Fig. 4.3, with densities on the order of 10^{19} cm^{-3}. The simulations also show lower density plasma reaching temperatures in the keV range when the plasma impacts the inner support structure. For this model, we will use the more realistic final bulk temperature of 100 eV, shown in Fig. 4.3, which is quite close to

the temperature of a MagLIF liner at stagnation, where the relatively cold liner material is surrounding the hot (∼3 keV) fusion fuel. Note that these parameters at stagnation give a plasma parameter Λ of less than 100 (and a plasma coupling parameter Γ_c of less than 0.1), meaning this is neither a strongly nor weakly coupled plasma. The plasma parameter is defined as $\Lambda = 4\pi n_e \lambda_D^3$, where n is the number density of electrons and λ_D is the Debye length. The coupling parameter is defined as $\Gamma_c = (q_e^2/(4\pi\varepsilon_0 k T_e))(4\pi n_e/3)^{1/3}$, where T_e is the electron temperature, k is the Boltzman constant, and q_e is the electron charge. The fusion fuel in ICF experiments typically have Λ values in the range of 1000's, meaning they are weakly coupled plasmas. However, the shells that surround the fusion fuel are likely not as weakly coupled, since they will be colder than the fusion fuel. Taking an example MagLIF liner at stagnation with a temperature of 100 eV and number densities ranging from 10^{20} – 10^{22} cm^{-3} results in $\Gamma_c = 0.01$ – 0.05. These values that indicate that the MagLIF liners should be slightly more strongly coupled than our university scale liners.

Using this temperature estimate and aluminum's ionization energies from NIST [83] we can estimate values for the average ionization level, $\bar{Z}$, throughout the implosion. We can also compare our model to SESAME table values for aluminum, as shown in Fig. 4.4. The table uses the QLMD (quantum Lee More Desjarlais) conductivity model for Al, generated by tuning the wide-ranging Lee-More-Desjarlais algorithms [80] to QMD/Kubo-Greenwood calculations of the conductivity [81].

Both of our simple models capture the same trends that the more robust QLMD model does, and electrical conductivities are within an order of magnitude of each other at worst case. Now that we have an idea of how conductive our plasma is, we can calculate and plot the magnetic Reynolds number, a sample plot is provided in Fig. 4.5. Varying our parameters across reasonable ranges of temperature and density, we find that $R_m = 1$ anywhere from t = 75–100 ns. These will be our bounds for possible values of t_{freeze} during the liner implosion. Note that those times only apply to the short pulse shots and not to the long pulse shots.

Using experimental data, along with our estimates for t_{freeze}, we can now implement Eq. 4.1 and compare to our measured inner axial magnetic field values. We present two sample cases of this calculation for two different mid-field DSP cases in Figs. 4.1 and 4.2. Our estimates appear to do quite well in the case of shot 5396, but not in the case of shot 5397. These two cases reach different measured peak values despite nearly identical current traces and identical liner trajectories; however, in the case of shot 5396, the raw, unintegrated, B-dot signal clipped the top of the scope, artificially reducing the measurement. This also helps explain why the two shots have such radically different values for the inner magnetic field measurement. Looking at shot 5397, we see that our estimate underpredicts the growth

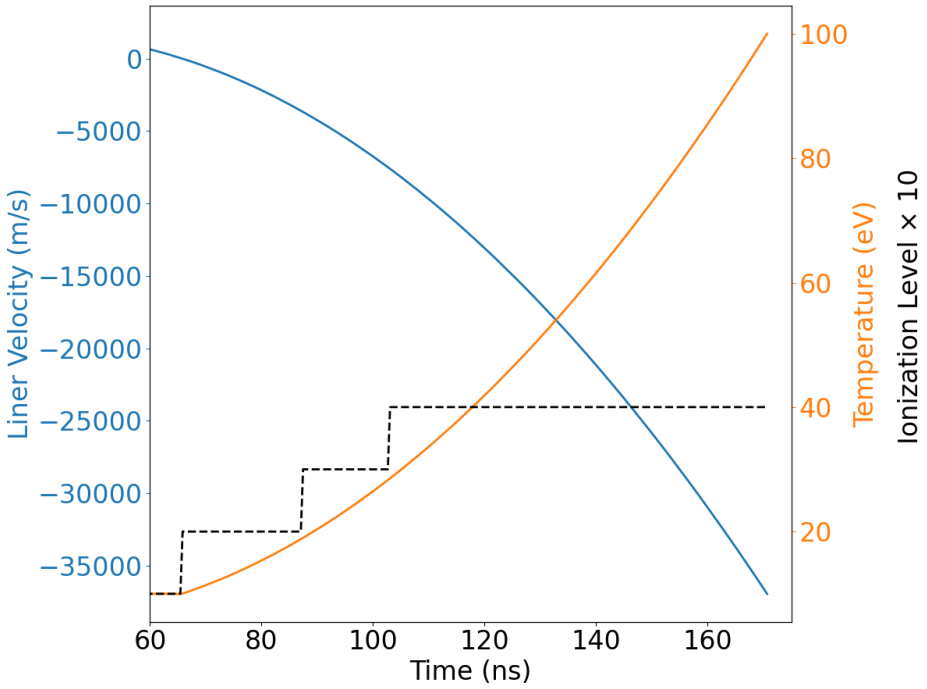

Figure 4.3: A plots of the liner parameters: velocity, temperature, and ionization level, as functions of time in the case where the final electron temperature reaches 100 eV.

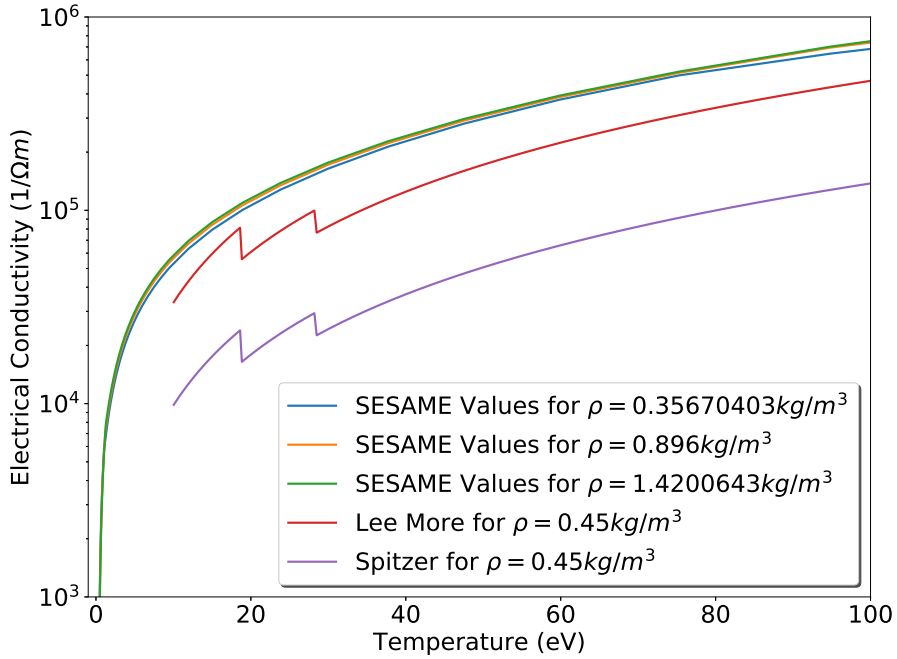

Figure 4.4: A plot of the liner conductivity, as a function of temperature, using both the Lee More and Spitzer models as well as values from the SESAME tables.

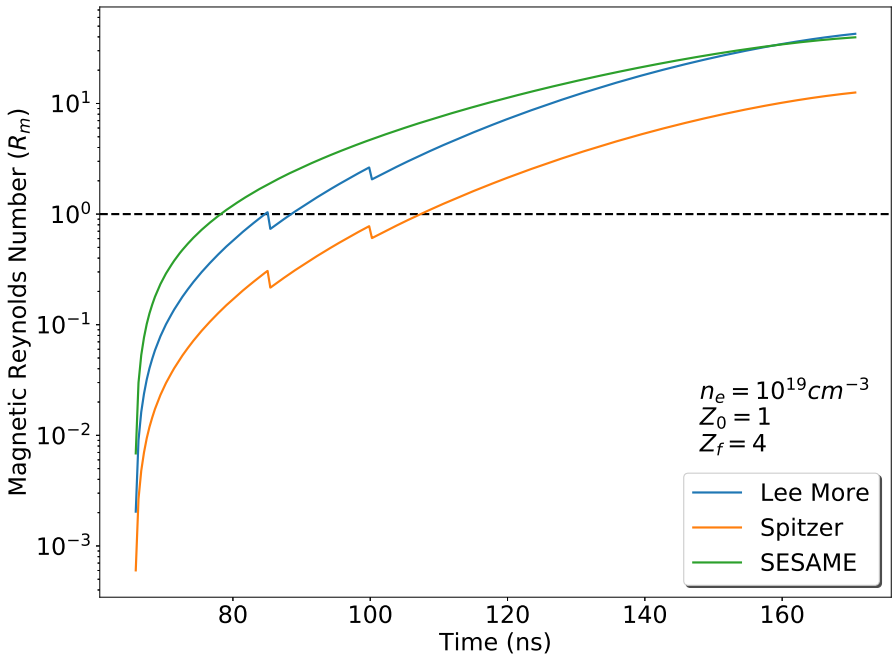

Figure 4.5: A plot of the magnetic Reynold's number, as a function of time, using SESAME values as well as our two simplified models. The simplified models used the listed number density, the SESAME curve uses a slightly higher number density. Ionization levels and temperatures used were previously given in Fig. 4.3(a).

of the inner axial field by a factor of two. In addition to this, our model's rate of rise also lags behind the measured inner axial magnetic field values.

The underpredicting of the measured values is consistent across other DSP cases as well. One explanation for this is the fact that Eq. 4.1 uses the *inner* liner radius and what we are able to measure is the *outer* liner radius. The outer radius consistently reaches a normalized radius (final radius divided by the initial radius) of 0.5, but the inner radius could be imploding all the way onto the inner support rod, which has a normalized radius of 0.2. This means that our calculations are only increasing the peak inner field values by a factor of 4, when they could need to be increased by as much as a factor of 25. Based on simulations from Weis [71] and experiments from Zier [70], the ohmically heated and expanding foil liner material could have a wide range of potential thicknesses, 100–1000 µm. When applying the Velikovich and Schmit theory, a liner thickness of 250 µm was found to be an ideal value for matching the relative cumulative instability growth across the various SZP/DSP cases tested [63]. We will take values of 250 µm and 800 µm as our bounds so, at a maximum, our convergence ratio is increased from 2 to 4. Taking a maximum value of 1000 µm forces the inner radius of the liner to values below the inner support rod radius at stagnation. These updated magnetic field estimates are presented in Figures 4.6 to 4.10.

Using our new inner radius values (see Figures 4.6 to 4.10) we find that the upper bound of the estimated spread is closer to the measured peak values of the axial magnetic field but the model is still slightly under predicting in all but one case. Unsurprisingly, since the liner trajectories have not changed (they have just been shifted down), the estimated axial magnetic field rise is still delayed with respect to the measured spread. This delay could be occurring for a couple of reasons. First, if the ablation of the liner happens immediately (i.e. within 10 ns into the current pulse), then the magnetic field could be frozen in even earlier than anticipated. Depending on what the density of the magnetic field carrying layer of plasma is, this potentially lower density layer could start to implode much earlier than the bulk material. The combination of these events would lead to a faster rise in the compression of the inner axial magnetic field. Along these lines, a low density plasma could be blowing off the bulk liner surface and hitting the on axis B-dot probe possibly damaging the probe, or interfering with the measurement. This seems unlikely, since the hallmark of a failed B-dot probe is when the signal plummets towards a large negative voltage, and clips the bottom of the oscilloscope. The on-axis B-dot probes do consistently show this behavior, but the probe failure occurs at roughly the same time as liner stagnation. For cases where the B-dot signal cuts out before the liner stagnates, this means we are likely *under measuring* the amount of flux compression. Additionally, even with identically repeated experiments, probe failures occurring at slightly different times (semi-randomly) from shot to shot would lead to different

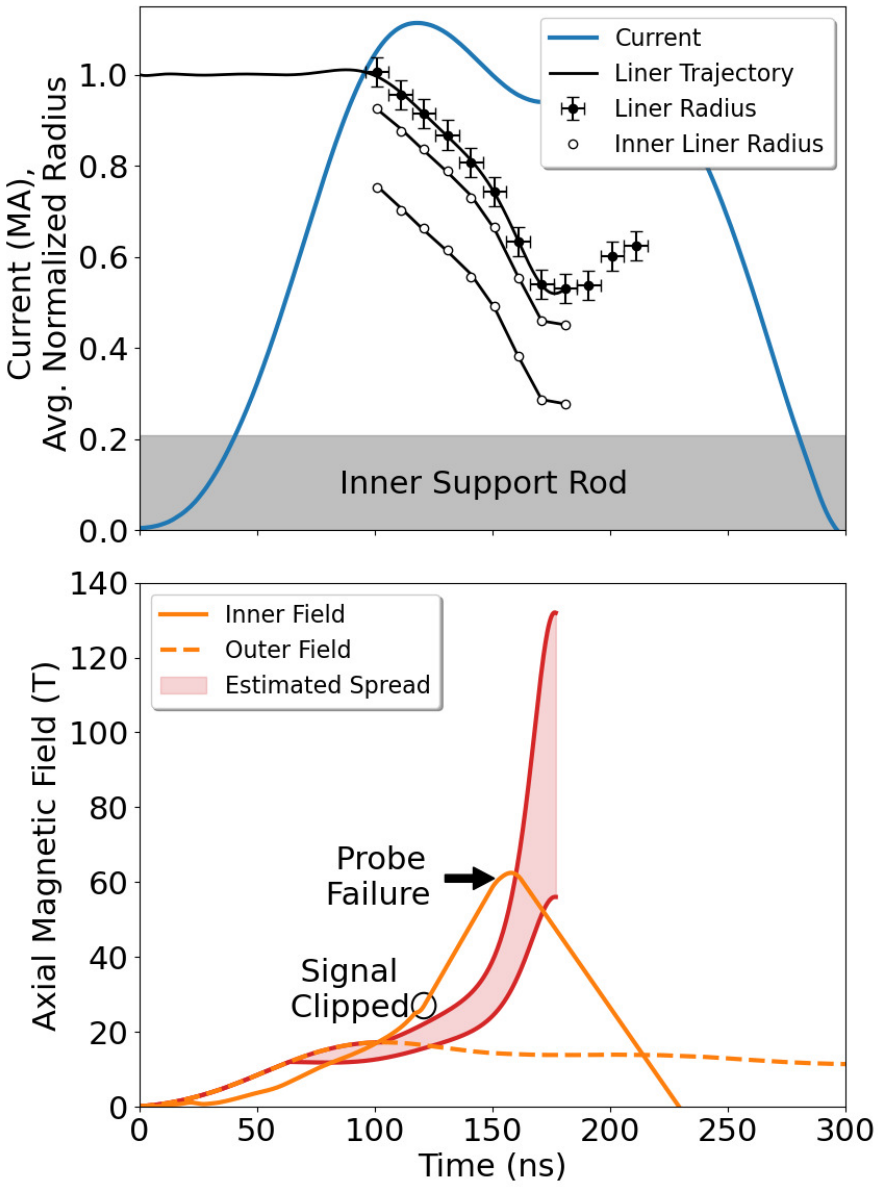

Figure 4.6: Experimental data from shot 5396, which used the mid-field DSP configuration with COBRA in short pulse mode. (Top) Measured (black filled circles) and inferred liner radii (white filled circles) and drive current, along with a fit to estimate the liner's trajectory. The inferred radii of the liner's inner surface (white filled circles) are downshifted by 250 µm and 800 µm from the measured radii to account for the assumed liner shell thickness. The radius of the inner support rod is also shown. (Bottom) Axial magnetic field values both inside and outside the liner are plotted along with an estimate of how much the inner axial field should increase, based on the minimum and maximum values of t_{freeze}, measured imploding liner radii of the liner's outer surface, and measured outer axial magnetic field. Note that the signal for the inner axial field measurement clipped the scope prior to probe failure so the peak value is lower than it should be.

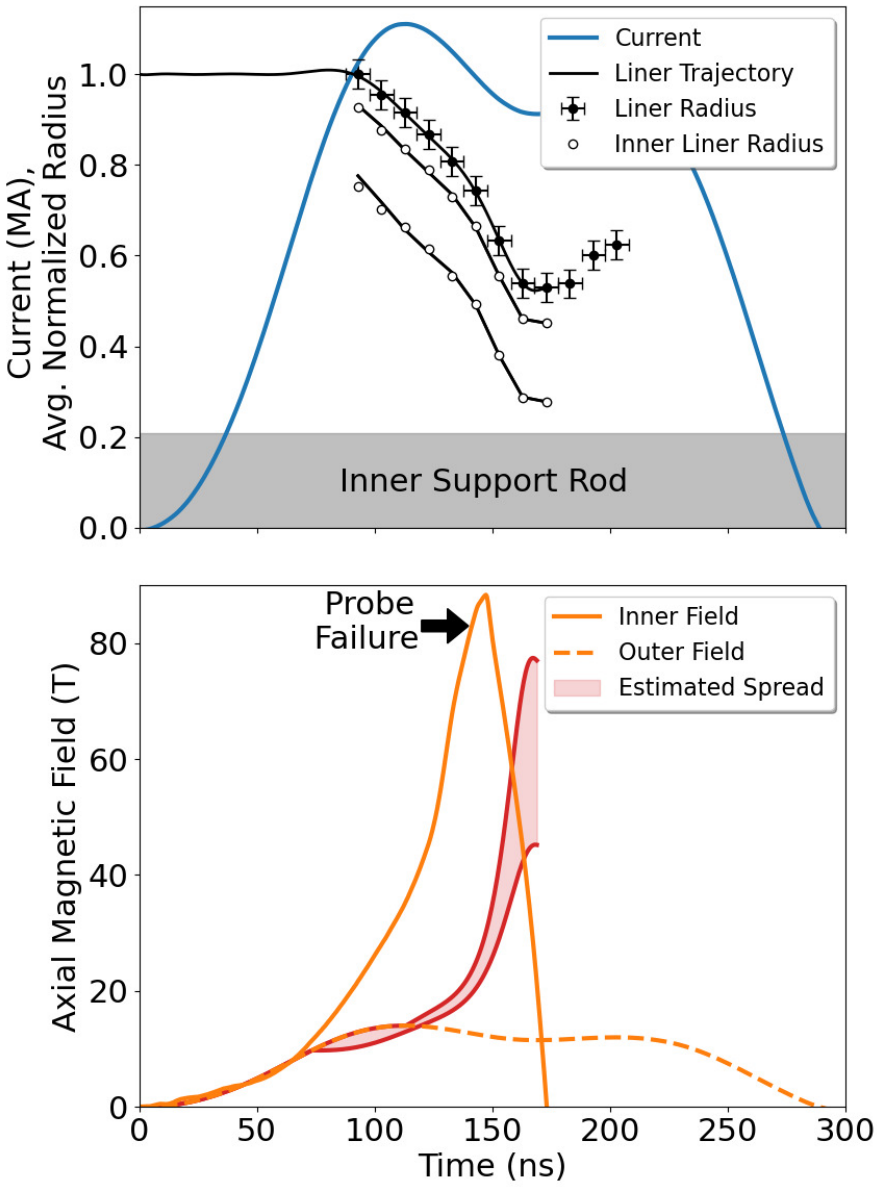

Figure 4.7: Experimental data from shot 5397, which used the mid-field DSP configuration with COBRA in short pulse mode. (Top) Measured (black filled circles) and inferred liner radii (white filled circles) (from shot 5396, since the camera was mistimed) and drive current, along with a fit to estimate the liner's trajectory. The inferred radii of the liner's inner surface (white filled circles) are downshifted by 250 µm and 800 µm from the measured radii to account for the assumed liner shell thickness. The radius of the inner support rod is also shown. (Bottom) Axial magnetic field values both inside and outside the liner are plotted along with an estimate of how much the inner axial field should increase, based on the minimum and maximum values of t_{freeze}, measured imploding liner radii of the liner's outer surface, and measured outer axial magnetic field.

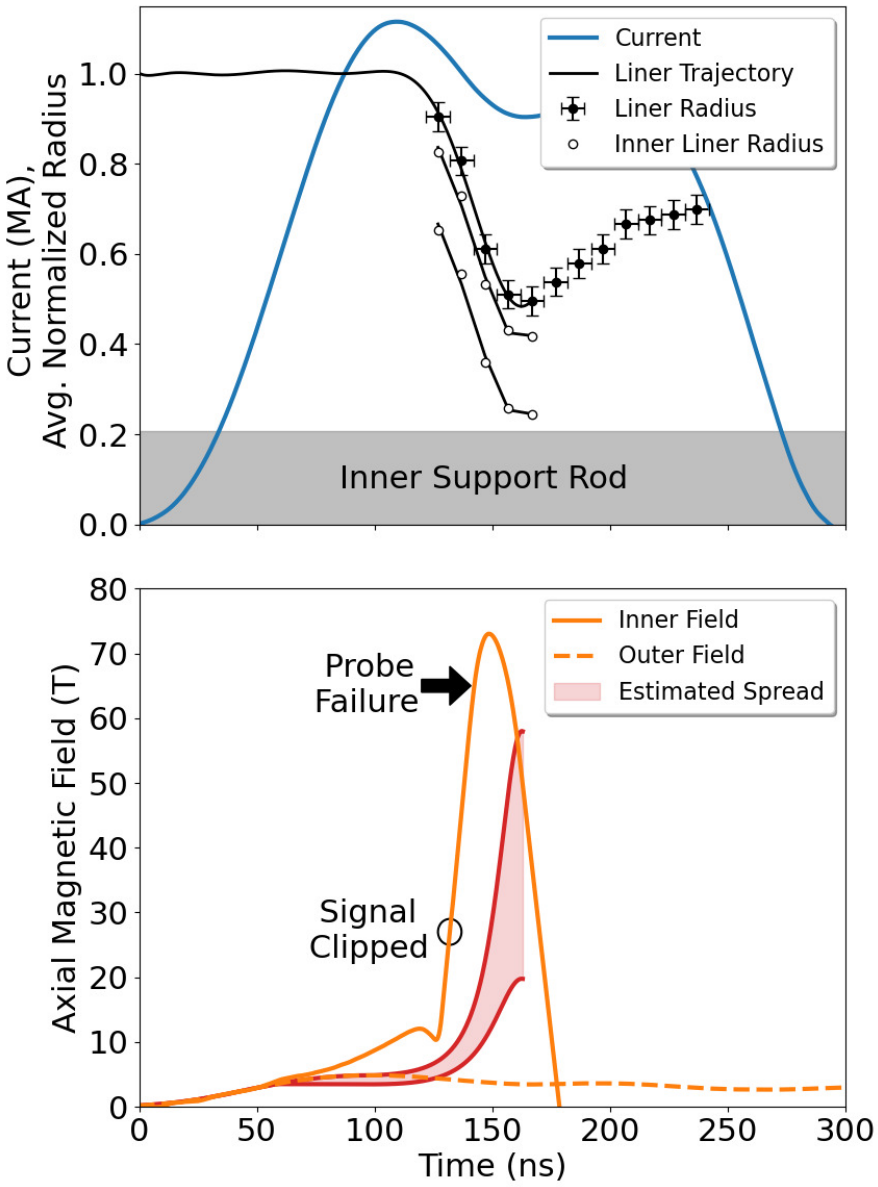

Figure 4.8: Experimental data from shot 5403, which used the low-field DSP configuration with COBRA in short pulse mode. (Top) Measured (black filled circles) and inferred liner radii (white filled circles) and drive current, along with a fit to estimate the liner's trajectory. The inferred radii of the liner's inner surface (white filled circles) are downshifted by 250 µm and 800 µm from the measured radii to account for the assumed liner shell thickness. The radius of the inner support rod is also shown. (Bottom) Axial magnetic field values both inside and outside the liner are plotted along with an estimate of how much the inner axial field should increase, based on the minimum and maximum values of t_{freeze}, measured imploding liner radii of the liner's outer surface, and measured outer axial magnetic field. Note that the signal for the inner axial field measurement clipped the scope prior to probe failure so the peak value is lower than it should be.

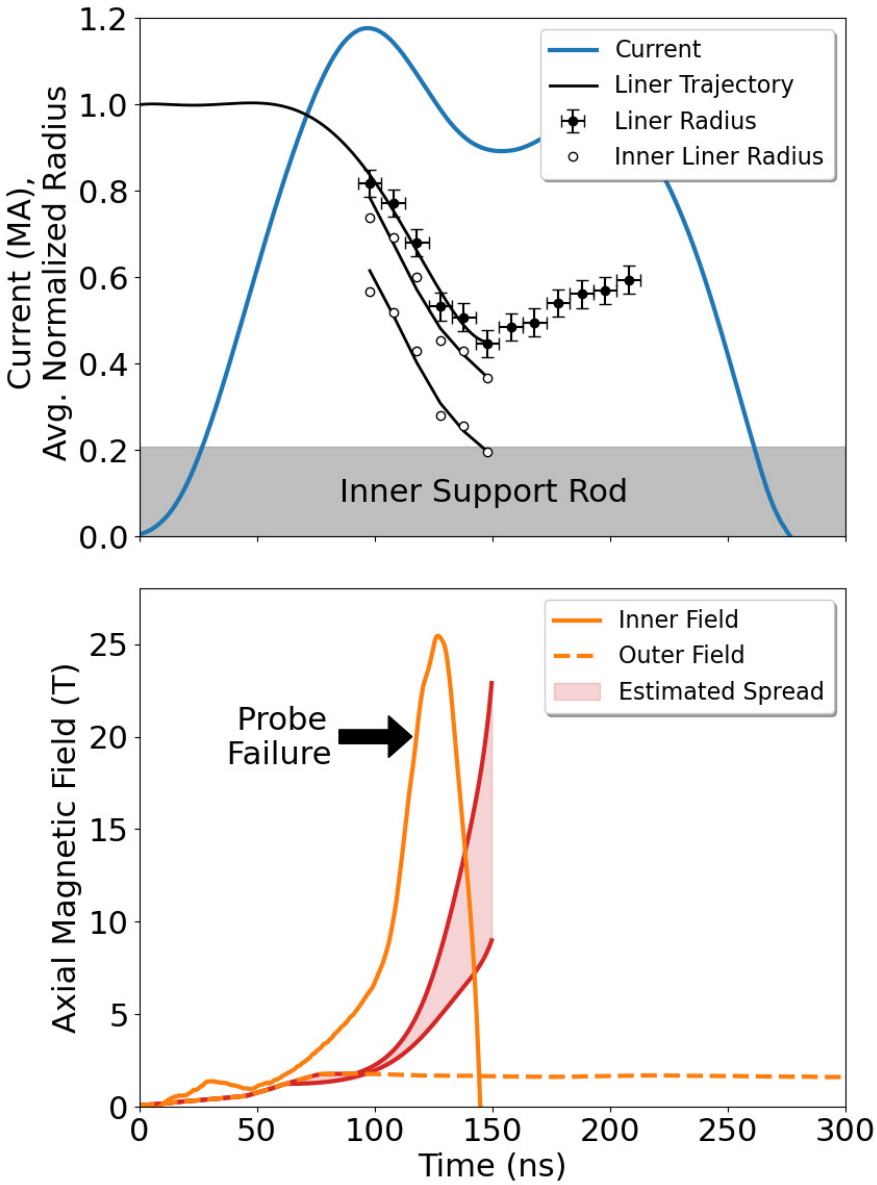

Figure 4.9: Experimental data from shot 5404, which used the low-field DSP configuration with COBRA in short pulse mode. (Top) Measured (black filled circles) and inferred liner radii (white filled circles) and drive current, along with a fit to estimate the liner's trajectory. The inferred radii of the liner's inner surface (white filled circles) are downshifted by 250 µm and 800 µm from the measured radii to account for the assumed liner shell thickness. The radius of the inner support rod is also shown. (Bottom) Axial magnetic field values both inside and outside the liner are plotted along with an estimate of how much the inner axial field should increase, based on the minimum and maximum values of t_{freeze}, measured radii, and measured outer axial magnetic field.

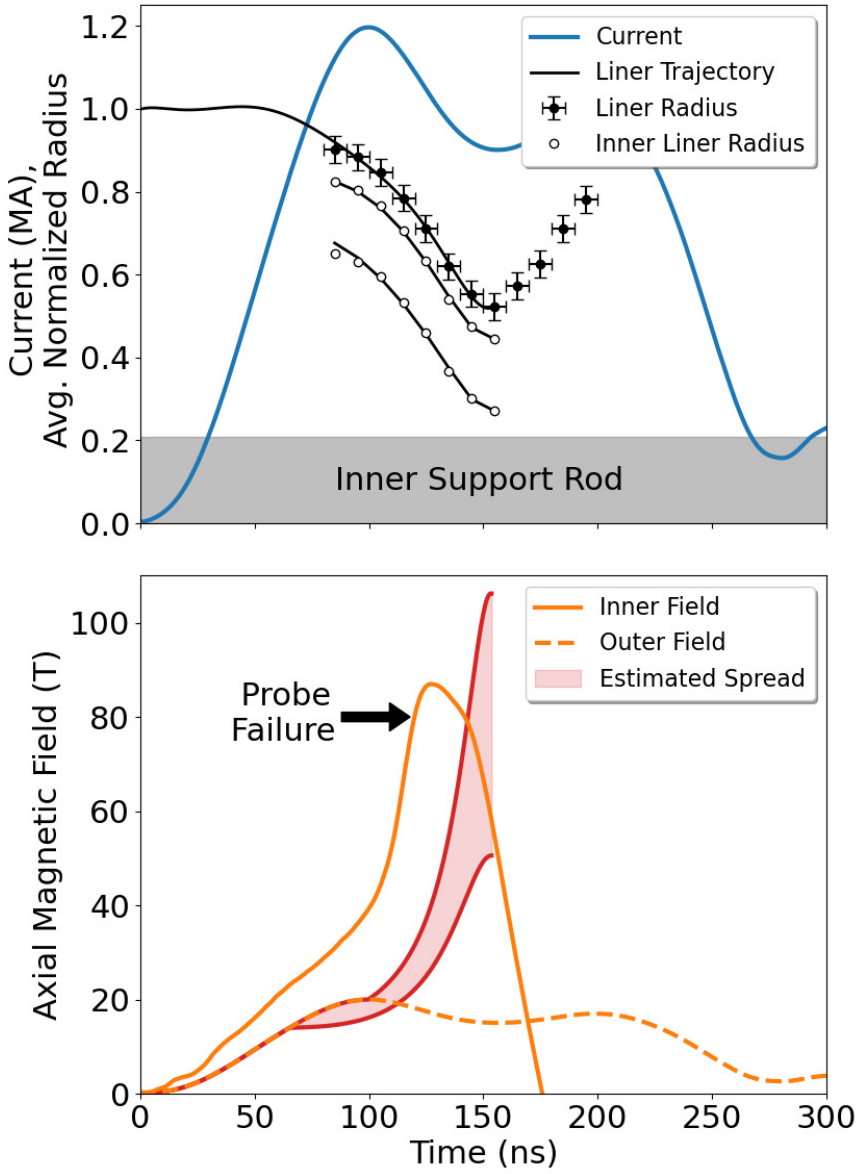

Figure 4.10: Experimental data from shot 5407, which used the high-field DSP configuration with COBRA in short pulse mode. (Top) Measured and inferred liner radii and drive current, along with a fit to estimate the liner's trajectory. The inferred radii of the liner's inner surface (white filled circles) are downshifted by 250 µm and 800 µm from the measured radii to account for the assumed liner shell thickness. The radius of the inner support rod is also shown. (Bottom) Axial magnetic field values both inside and outside the liner are plotted along with an estimate of how much the inner axial field should increase, based on the minimum and maximum values of t_{freeze}, measured radii, and measured outer axial magnetic field. Note that the outer axial field values are estimated from simulation since the outer B-dot probe failed on this shot.

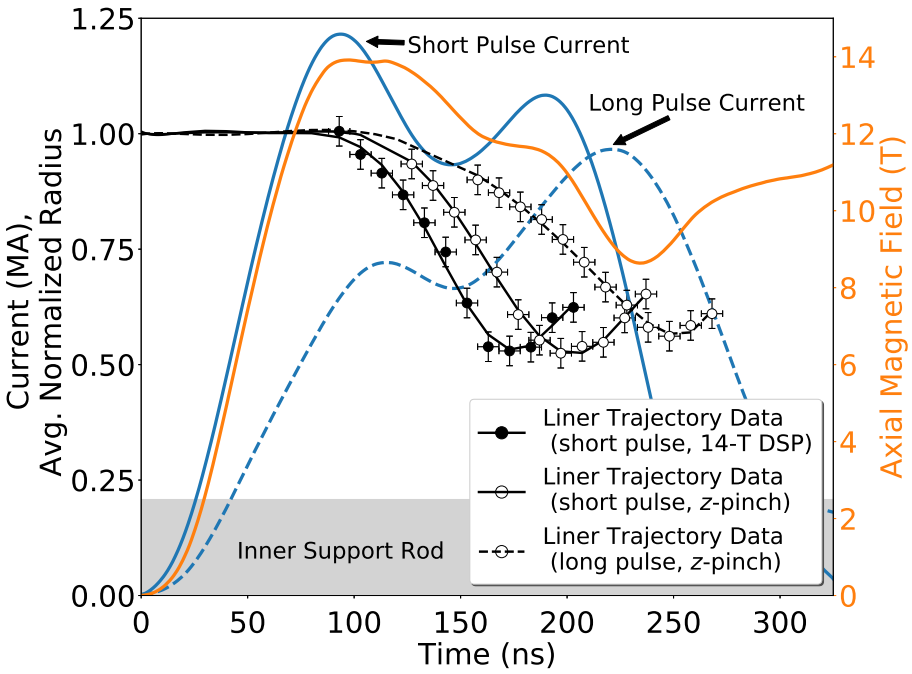

Figure 4.11: Example experimental data, including drive currents, liner implosion trajectories, and the axial magnetic field, $B_z(t)$, measured on the mid-field DSP shot that produced the short-pulse current trace shown. Fitting curves for the experimentally measured liner radii are also plotted.

amounts of peak flux compression measured in each shot. However, the flux compression history up until the time of probe failure should be the same from shot to shot, if all of the ablation and implosion dynamics remain the same. Implosion dynamics do vary, especially when comparing SZP to DSP shots. Sample trajectories are presented in Fig. 4.11.

Secondly, two simulation papers [54, 67] have shown axial fields diffusing through thick liners on time scales much faster than anticipated. The authors in Ref. [54] posit that the mechanism for this is that resistivity gradients in the liner can carry field lines toward the axis on shorter time scales than magnetic diffusion acting alone. Such large resistivity gradients seem unlikely in our ultrathin liners, but, if they exist, then this could account for the difference we see between our model of flux compression and the on-axis B-dot measurements.

Finally as we noted earlier some low density plasma in the PERSEUS simulations appears to be getting quite hot as it impacts onto the liner at stagnation. This lower density plasma could be blowing off the liner and get injected inward much faster than the bulk liner plasma, similar to a precursor plasma in wire arrays. This lower density coronal plasma could also carry frozen in magnetic field lines which would lead to the early rise in axial magnetic field signal observed in experiment.

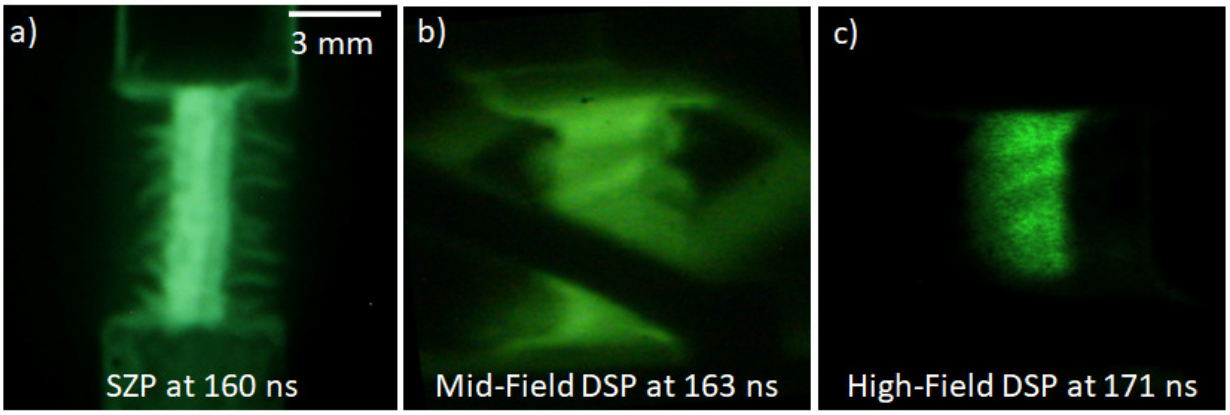

Figure 4.12: Contrast enhanced XUV images from three of the experimental cases taken near the time of stagnation. (a) The SZP case. (b) The mid-field DSP case. (c) The high-field DSP case.

4.2 Plasma Imaging

To study the instability evolution of our liners, a 12-frame fast framing camera and two 4-frame extreme ultraviolet (XUV) imaging cameras were fielded. Both imaging systems relied on self emission of the plasma (albeit at different wavelengths). The images reveal the profound effects that the various return-current structures had on the instability evolution. In particular, these images reveal that helical modes were present for the DSP cases and were absent for the SZP case. The helical modes are more readily apparent in the XUV images. These observations are reminiscent of the helical striations observed previously on the surfaces of *non*-imploding foil-liners in experiments with twisted return-current structures [84].

The imploding helical modes presented in Fig. 4.12 should evolve according to Eq. 2.30. As a reminder, the equation is defined as $\phi_{plasma} \approx \arctan[p/(2\pi R)] \approx m/(k_z R)$, where ϕ_{plasma} is the pitch angle, p is the helical pitch, and k_z is the axial wave number. In the XUV images of Fig. 4.12, the mid-field DSP return-current structure partially obstructs the view of the imploding liner in the mid-field case. This along with the small number of viewable striations make it difficult to identify m. However, the images can still be used to measure ϕ_{plasma}, p, and R, and thus the ratio m/k can be determined. Furthermore, other liner implosion experiments with B_z fields (using externally driven axial field coils) have found that $p \approx constant$ throughout the implosion [65]. This is effectively equivalent to $m/k \approx constant$ throughout the implosion [56]. If the assumption that $m/k \approx constant$ is made for the DSP cases, then the pitch angle of the plasma helices can be estimated for times when the liner first begins to implode. This initial plasma pitch angle, $\phi_{plasma,0}$, can then be compared to

the initial pitch angle of the magnetic field, $\phi_{B,0} = \arctan(B_z/B_\theta)$, which should be constant up until the time when the liner starts to implode. For example, in the mid-field DSP case, see Fig. 4.12(b), $m/k = 23 \pm 8$ degree-mm, which traces back to $\phi_{plasma,0} = 7 \pm 3°$, while $\phi_{B,0} = 6 \pm 1°$ [63]. Repeating the calculation for the high-field DSP case, see Fig. 4.12(c), $m/k = 30 \pm 9$ degree-mm, which traces back to $\phi_{plasma,0} = 10 \pm 3°$, while $\phi_{B,0} = 10 \pm 1°$. These initial pitch angles are nearly equal (within uncertainties), implying that the instability pitch angles observed during the implosion and after stagnation are set by $\phi_{B,0}$. Note that the calculation for the high-field case uses calculated axial field values rather then measured axial field values due to B-dot probe failure.

Furthermore, from these calculations, we see that $\phi_{plasma}(t)$ increases throughout the implosion, while $\phi_B(t)$ decreases throughout the implosion (see Fig. 4.13). Thus, it is likely that $\mathbf{k} \cdot \mathbf{B} \neq 0$ for these most dominant helical modes observed, which should imply enhanced stability. From the plots shown in Fig. 4.13 we see that the high-field DSP case should be the most stable out of the cases tested, relative to the standard z-pinch, which has no rotation of either ϕ_B or ϕ_{plasma}.

To further quantify the stability of the implosions, the visible imaging data (see Fig. 4.15) were analyzed to extract the instability amplitude as a function of the liner's normalized distance moved, $\hat{d} \equiv 1 - R(t)/R(0)$. Presenting the data as a function of $\hat{d}$ allows for both the short-pulse and long-pulse data to be plotted together. The results of this analysis are presented in Fig. 4.16, where the instability amplitudes for the mid-field and high-field DSP cases are shown to be smaller than in the SZP case by factors of about 2 and 3, respectively, at $\hat{d} = 0.5$ ($C_r = 2$, as a reminder $C_r = R_{out,i}/R_{out,f}$). Specifically, at $\hat{d} = 0.5$ ($C_r = 2$), the MRTI amplitudes for the SZP case and for the 14-T and 20-T DSP cases were, respectively, 1.1±0.3 mm, 0.7±0.2 mm, and 0.3±0.1 mm. Here the amplitudes were found by tracking the plasma-vacuum interface and taking the difference between the peaks and valleys. The error bars represent the standard deviations in the measurements. Note that the image resolution contributes negligibly to the plotted error bars. We also note that there was one low-field shot that appears to have grown from a large initial perturbation, which is not surprising given the delicate nature of such thin-foil liners. For the full 12-frame image sequences see Appendix C.

Not included in this analysis are corrections due to MRT bubble filling. Bubble filling is an unintended consequence of self emission imaging that can occur for MHDI with $m \geq 1$. Take for example the $m = 0$ sausage instability case shown in Fig. 4.17. It is easy to see in either perturbation case where the peaks and troughs (bubbles) of the instabilities are. But as the mode number increases to $m \geq 1$, the trough appears to move outward (i.e., the trough/bubble starts to fill in), as seen in Fig. 4.18, and 4.19. Because our visible self-emission

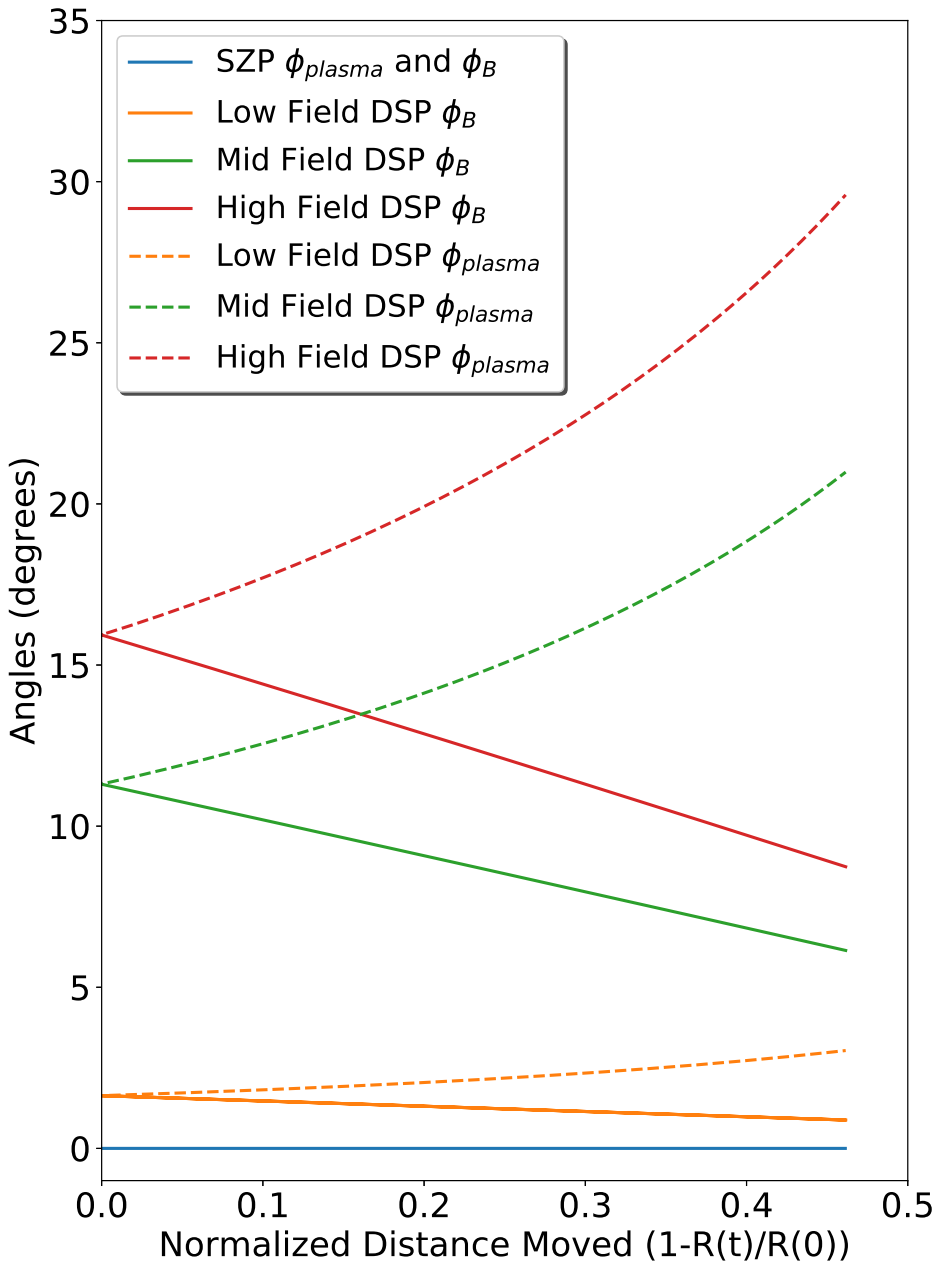

Figure 4.13: A plot of both the dynamic magnetic pitch angle $\phi_B(t)$, and the dynamic pitch angle of the plasma helices $\phi_{plasma}(t)$, for each of the experimental cases tested.

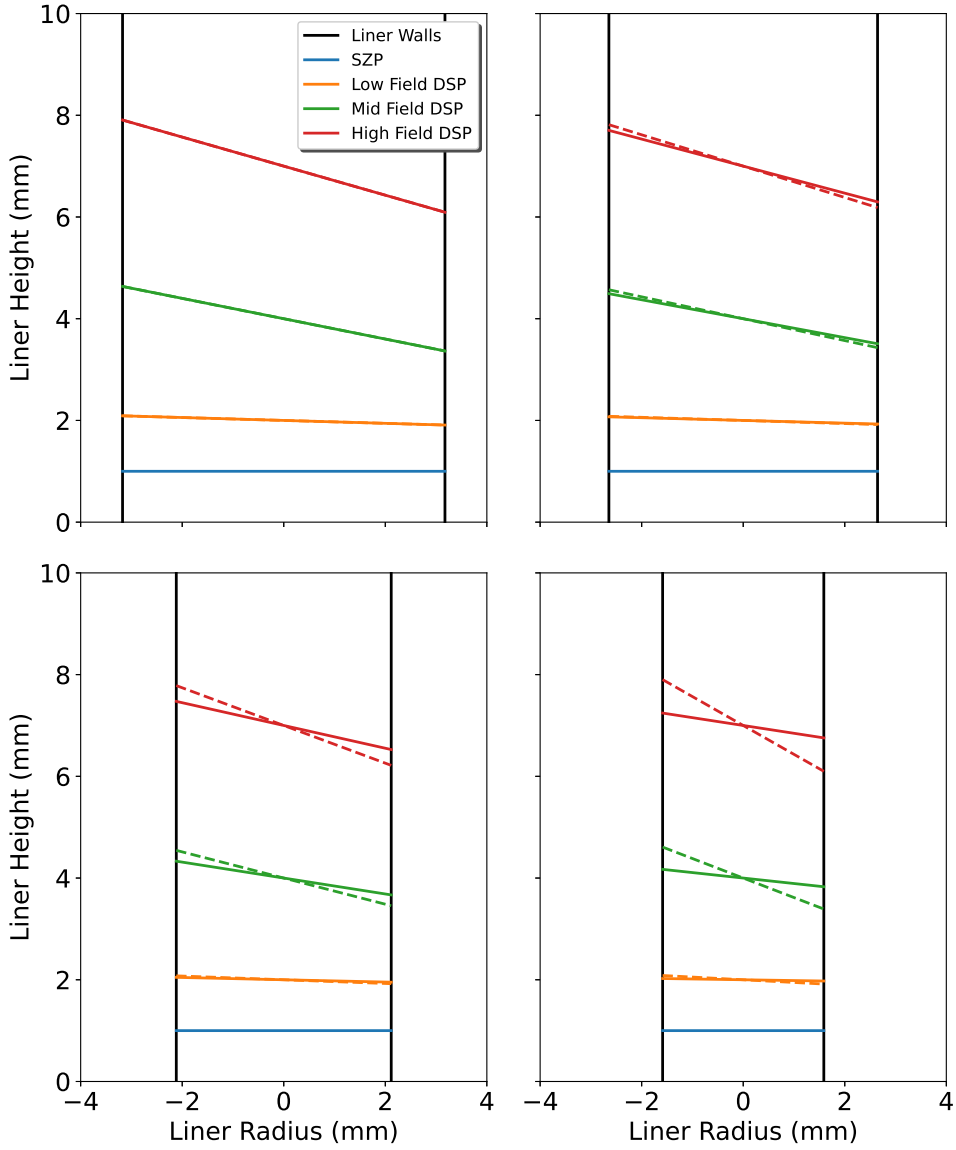

Figure 4.14: A plot showing how the pitch angle of the plasma helices $\phi_{plasma}(t)$ (dashed lines) and the pitch angle of the magnetic field lines $\phi_B(t)$ (solid lines) will evolve on the imploding liner's outer surface. Note that during the implosion, the plasma pitch angles increase while the magnetic field pitch angles decrease. Also note how the pitch p of the plasma helices remains constant as the liner implodes. This illustrates why the plasma pitch angles $\phi_{plasma}(t)$ increase during the implosion; $\phi_{plasma}(t)$ must increase under convergence in order to maintain a constant pitch p, since axial outflows are not permitted.

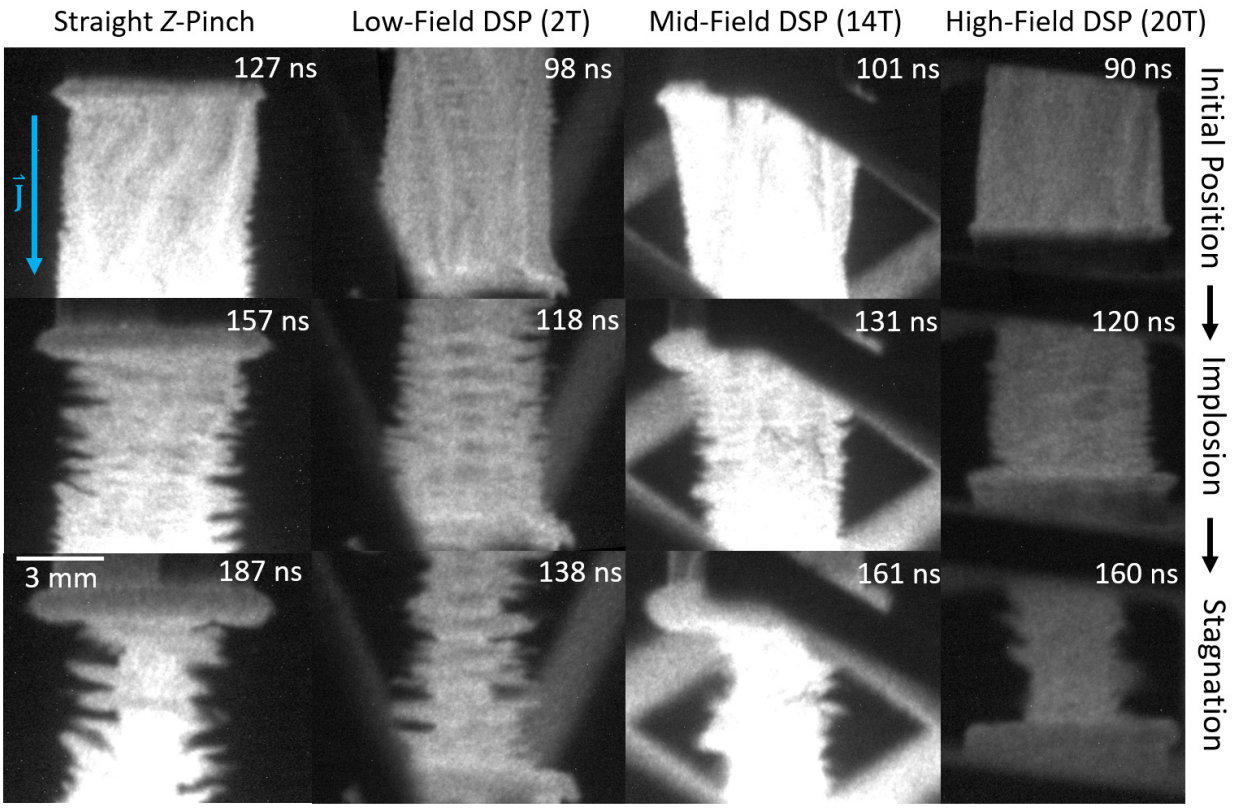

Figure 4.15: Sample visible self-emission images showing the liner dynamics from each of the experimental cases. Note that these images have not been contrast enhanced.

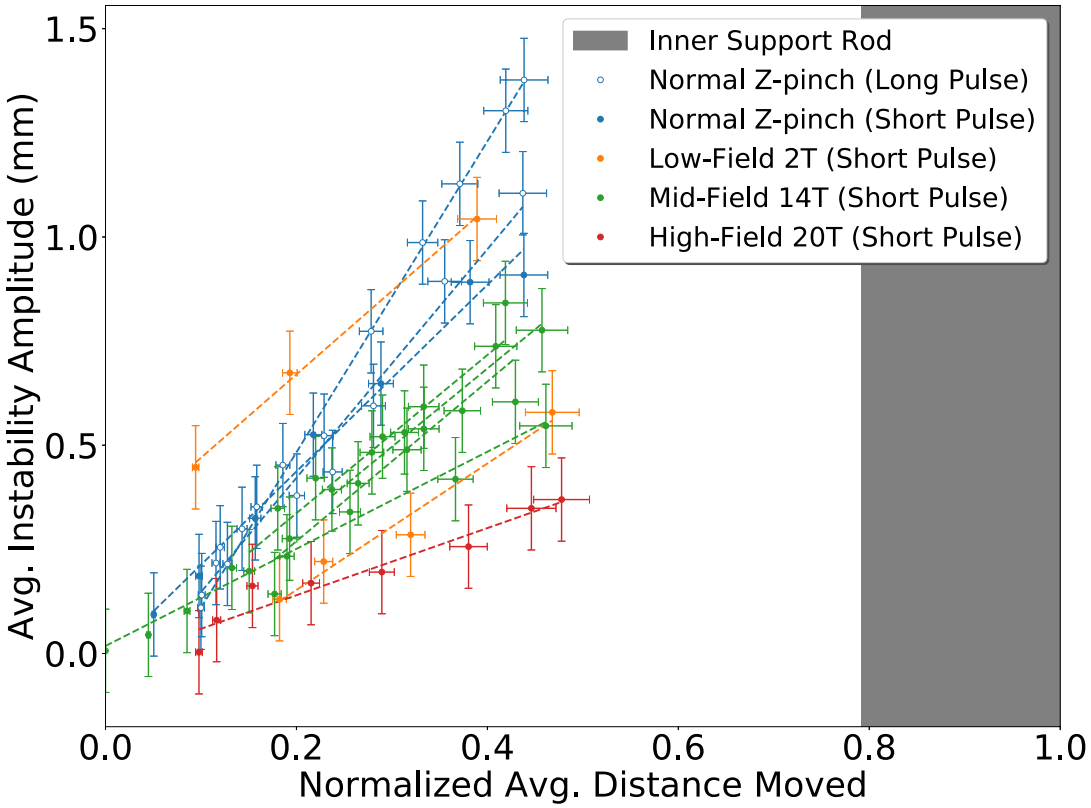

Figure 4.16: A plot of the average instability amplitudes as a function of the normalized distance moved, $\hat{d} = 1 - R(t)/R(0)$. Linear fits for each shot are plotted as dashed lines.

imaging is not complimented by any penetrating imaging, like x-ray radiography, we do not know how much bubble filling might be occurring in our experiments. However, after analyzing the amount of bubble filling in our simple graphical models (e.g., Figs. 4.17–4.19), we find that the effect is minimal for our cases of interest. The quantitative results are summarized in Figs. 4.20 and 4.21. The details of this analysis are discussed below.

We started by applying sinusoidal perturbations along the edge of a cylindrical liner that had imploded to a radius of 1.58 mm (half of its initial radius). Next, we varied both the perturbation amplitude (0.25–0.5 mm) and wavelength (1–2 mm) and found that the trough/bubble-filling effect is wavelength insensitive and does not become prominent until $m \geq 3$ (see Fig 4.20). By not prominent, we mean that the fractional change in amplitude does not drop below 0.8 until $m \geq 3$ is reached. Fractional change is defined as the ratio of the observed instability amplitude over the true instability amplitude.

While a sinusoidal perturbation is easy to model, it is not the most accurate model for instability growth that has gone nonlinear (where bubbles become cusp-like [62, 85]), so we will compare our sinusoidal perturbations results to cycloidic (cusp-like) perturbations. In the cycloidic case, we see that the bubble-filling effect does not become prominent until $m \geq 4$, (see Fig. 4.21). For the cases compared, we used a single wavelength of 2 mm, and a larger range of amplitudes (0.25 – 2 mm). In the most extreme case, the largest difference in perceived amplitude between the sinusoidal and cycloidic perturbations is roughly 0.4, which occurs at $m = 3$, when the bubble-filling effect becomes prominent in the sinusoidal case and is still negligible in the cycloidic case. It is unlikely that we are seeing any instabilities with modes numbers greater than 3, based on the analysis of the plasma and magnetic field pitch angles.

To compare the measured instability growth with theory, the finite-thickness cylindrical shell model of Ref. [7], discussed in Chapter 2 is used. As a reminder, this model is based on linear perturbation analysis and includes Bell-Plesset effects. We do not measure the position of the inner liner surface, only the outer liner surface, so we do not know the in-flight thickness of our liners. From previous work [70, 71], we have seen that there is a large range of likely thicknesses the liner can have (100–1000 µm). In Figs. 4.22–4.25, the cumulative instability growth, Γ (the number of e-foldings), is plotted for the four experimental cases tested over a range of assumed liner thicknesses (including an infinitely thin case). These contour plots also cover a large range of azimuthal mode numbers, m, and axial wave numbers, k_z and are computed from when $\hat{d}$ returns back to 0 after the expansion phase, until $\hat{d} \approx 0.5$, when the liner stagnates on axis.

Beyond contour plots, we also used the thick-shell V&S model to calculate the instability growth for a dominant perturbation structure with a pitch angle that rotates according to

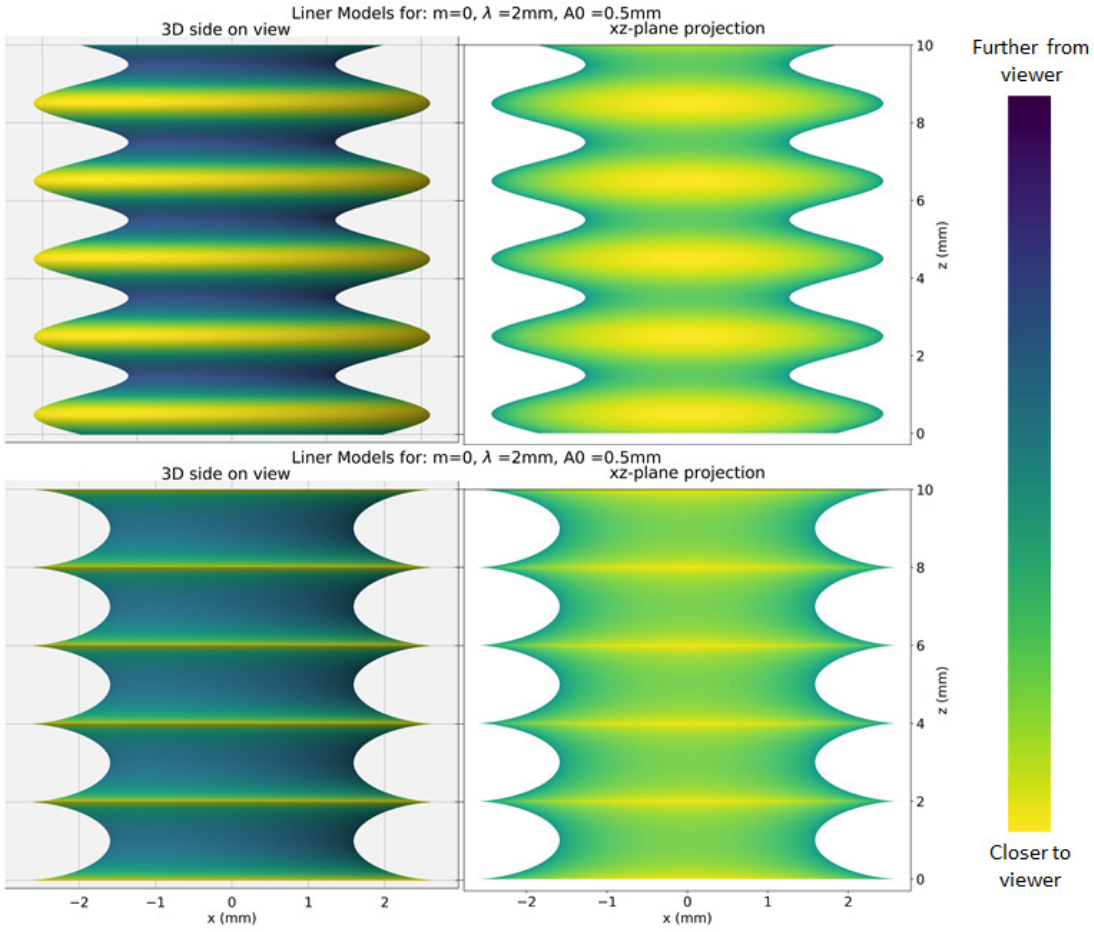

Figure 4.17: Shown here are two different views of a liner, for both sinusoidal (top) and cycloidic (bottom) perturbations. Shown on the left is a side-on view of a "3D" object. Shown on the right is the projection of that object onto the xz-plane; i.e., this is an attempt to mimic a picture of the object. While the colormaps are the same, they have slightly different meanings between the two cases. On the left, yellow corresponds to larger radius, while blue corresponds to smaller radius. On the right, yellow corresponds to being closer to the viewer (or camera), while blue corresponds to being father from the viewer.

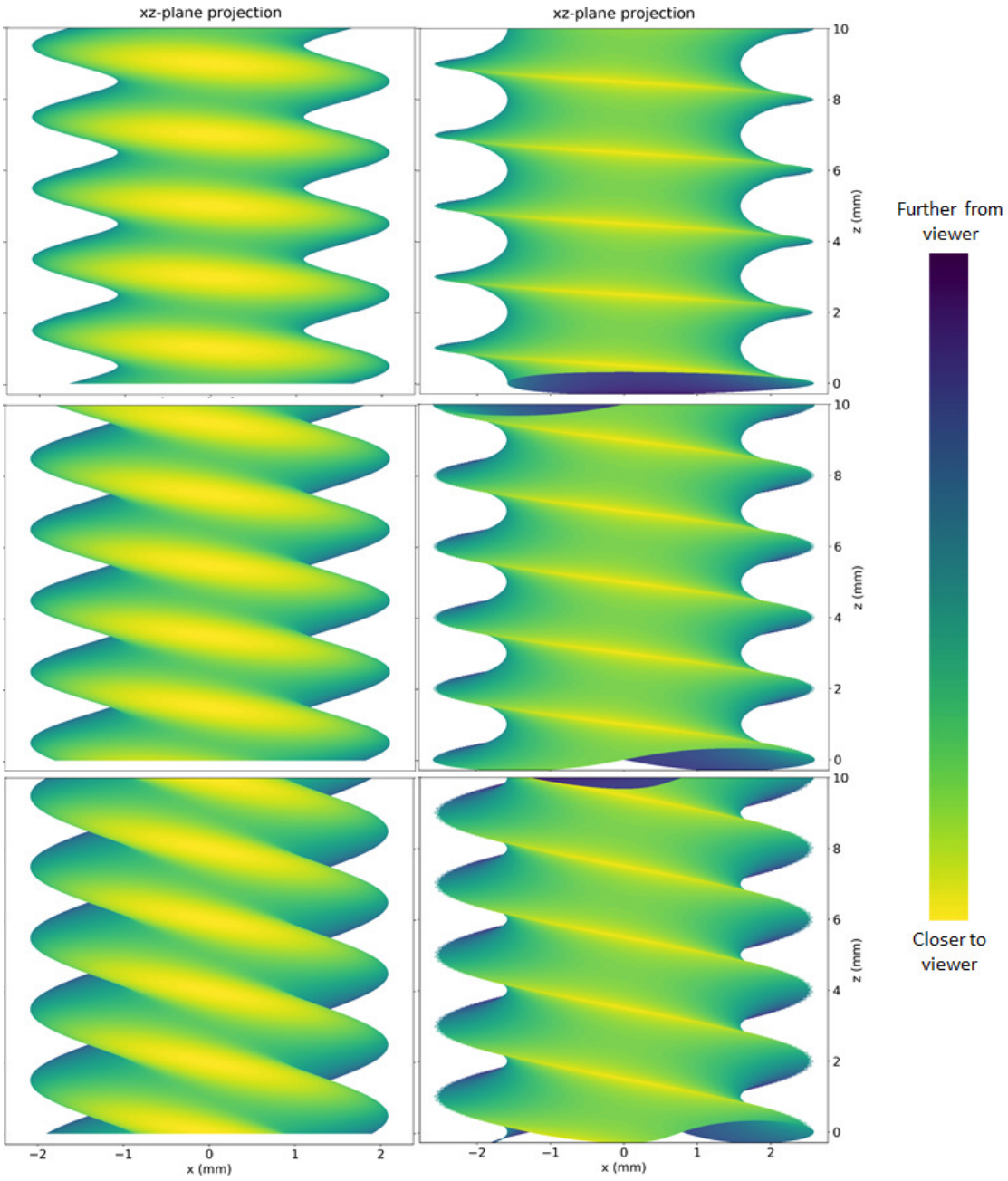

Figure 4.18: Shown here are two sets of liner models, one with sinusoidal perturbations (left) and one with cycloidic perturbations (right). Both sets are the xz-plane projection of the "3D" object, so yellow corresponds to being closer to the viewer (or camera), while blue corresponds to being father from the viewer. Azimuthal perturbations $m = 1$–3 are shown in this figure, with the $m = 1$ case on top and the $m = 3$ case on the bottom.

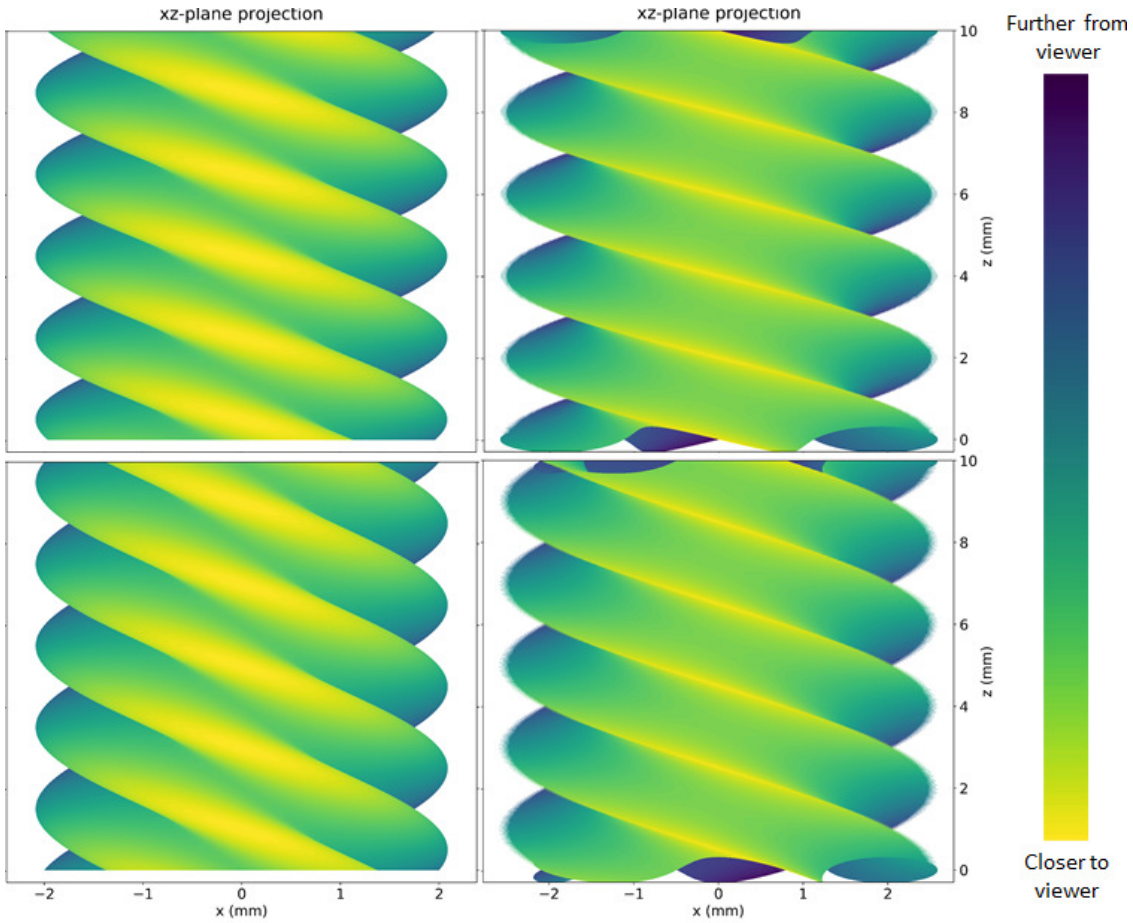

Figure 4.19: Shown here are two sets of liner models, one with sinusoidal perturbations (left) and one with cycloidic perturbations (right). Both sets are the xz-plane projection of the "3D" object, so yellow corresponds to being closer to the viewer (or camera), while blue corresponds to being father from the viewer. Azimuthal perturbations $m = 4$–5 are shown in this figure, with the $m = 4$ case on top and the $m = 5$ case on the bottom.

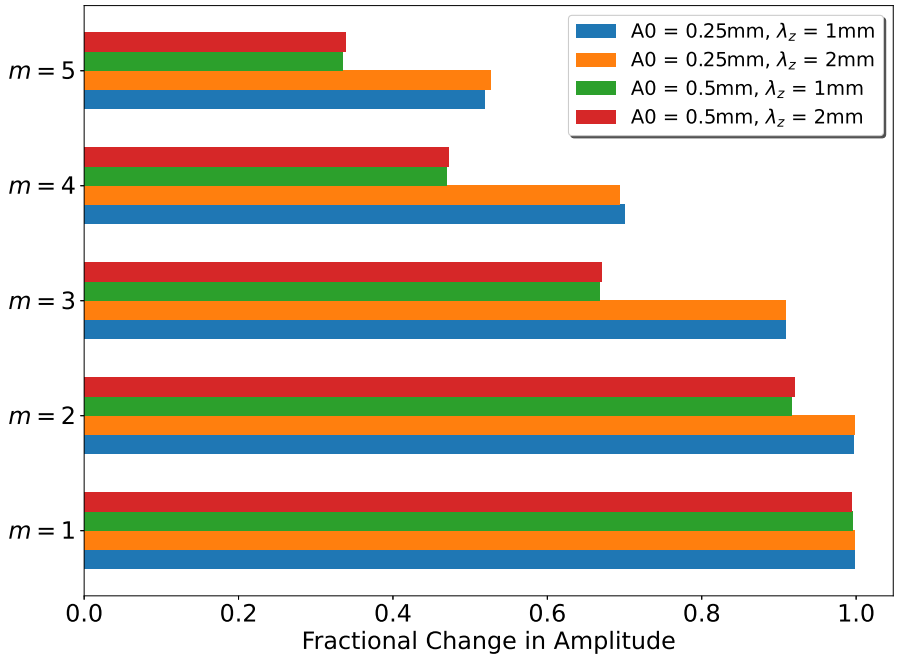

Figure 4.20: A plot of the fractional change in amplitude for four cases for sine wave perturbations. Ideally, there would be no difference in measured amplitude from the true amplitude, so on this plot, smaller numbers are worse.

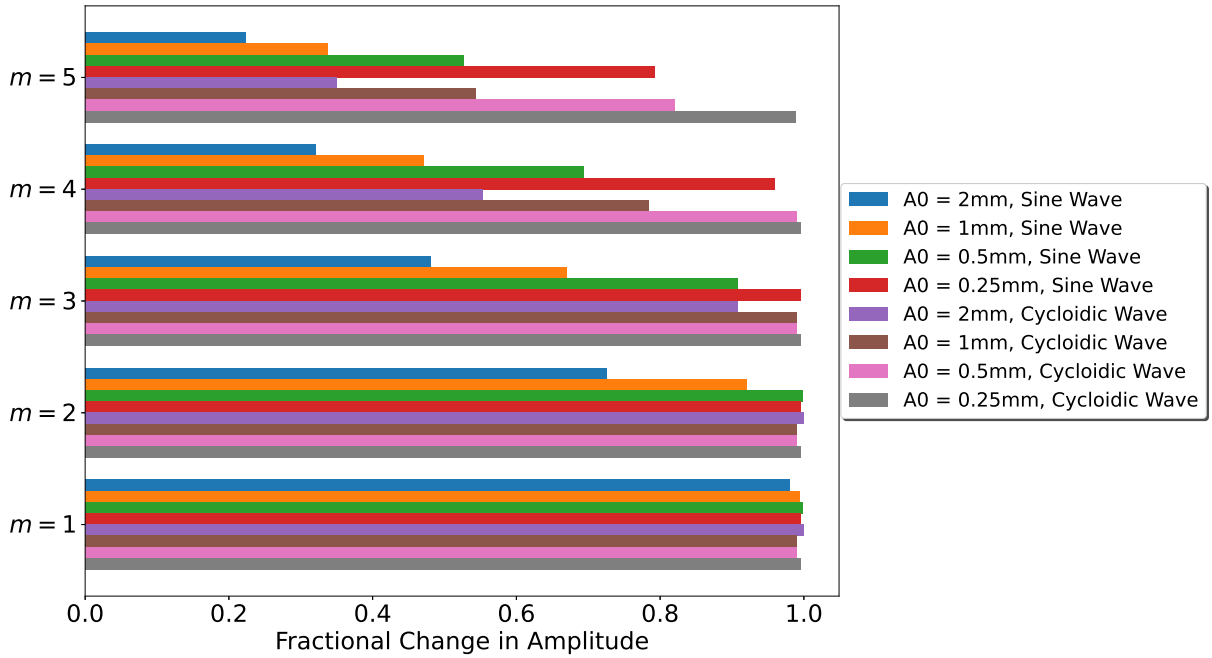

Figure 4.21: A plot of the fractional change in amplitude for four cases for both cycloid and sine wave perturbations. Ideally, there would be no difference in measured amplitude from the true amplitude, so on this plot, smaller numbers are worse.

our experimentally observed $\phi_{\text{plasma}}(t)$. This perturbation was driven by the experimental magnetic field, with a pitch angle that rotates according to $\phi_B(t)$. The perturbation was also allowed to cascade from shorter wavelengths to longer wavelengths, with $\lambda \propto \hat{d}$, as observed in our experiments and others [62]. This means that k_z as well as m cascade from larger values to smaller values, since $m/k_z \approx constant$ for imploding helical structures with constant pitch p. Based on our imaging data for $\hat{d} = 0.5$, we set the final axial wavelengths (λ_{zf}) for the SZP case and for the 2-T, 14-T, and 20-T DSP cases to 1 mm, 1 mm, 1.25 mm, and 1.5 mm, respectively (see Fig. 4.27). The values are from averages of the axial wavelengths on each interface of the liner (right and left), with the error coming from the standard deviation. Note that this analysis does exclude one outlier shot, a mid-field DSP shot (shot 5396), due to its unusually long axial wavelength (it is likely that this is due to a crinkle in the liner). Also note that the axial MRTI wavelengths increase as as the liner implodes. Since we do not know the initial perturbation wavelengths or amplitudes, we used the smallest wavelength observed to maintain a dominant (coherent) perturbation structure (50 µm) [86] and we used the initial amplitude (60 nm) that resulted in a match between theory and experiment for the amplitude growth of the SZP case at $\hat{d} = 0.5$. From the wavelengths, the values for k_z are computed assuming a slope of $(\lambda_f - \lambda_i)/(\hat{d}_f - \hat{d}_i)$. From the values of k_z the azimuthal mode numbers m can be determined from $m = -k_z R_{out,0} \tan \phi_{B,0}$. For the high-field DSP case, this results in an initial azimuthal mode number $m \approx -113$, hence the need for such a large sweep in m in the contour plots. However, in experiment, the largest azimuthal mode numbers m observed were in the mid-single digits, due to diagnostic limitations and the time periods targeted. We then applied these same initial wavelength and amplitude values to the DSP cases to evaluate the relative stabilization (see Fig. 4.28). At $\hat{d} = 0.5$, the resulting amplitudes for the SZP case and for the 2-T, 14-T, and 20-T DSP cases were, respectively, 1.27 mm (by construction), 1.27 mm (i.e., no significant stabilization), 0.60 mm, and 0.34 mm. These results agree well with the results presented in Fig. 4.16; however, it is important to note that these results depend on the λ_{zf} values chosen and on the shell thickness chosen (for which we used 250 µm, based on the exploding thin-foil studies presented in Refs. [70, 71]). Moreover, we are using a linear perturbation theory to describe a fundamentally nonlinear process (i.e., a wavelength cascade due to mode merger events).

When using constant m and k_z values instead of evolving the mode numbers, we find that the amplitudes are changed as shown in Fig. 4.29. In the case where the final wavelength and azimuthal mode numbers from the evolution of $\phi_{plasma}(t)$ are used, the resulting predicted amplitudes exhibit slightly smaller differences between the SZP and DSP cases than in the experiment, but yet they still agree reasonably well with the model where m and k_z are allowed to evolve. When using the initial wavelength and azimuthal mode numbers from the

evolution of $\phi_{plasma}(t)$, the differences between the SZP and DSP cases becomes very large and no longer closely reflect the trends captured in the experiment. Next, we can compare to a simpler model of instability growth. We start with Eq. 2.2 to determine the growth rate γ from the wavenumber k_z and the liner's effective gravity g. From this, an assumed exponential growth (linear perturbation theory) produces the plot shown in Fig. 4.30. Using this method results in comparable differences in the SZP and DSP cases to the differences that were observed in the experiment. These simpler models, with one exception, recreated the original model's theoretical growth plot fairly accurately, again capturing the relative stabilization seen in the experimental data, with the SZP case having the largest instability amplitude at stagnation and the high-field DSP case having the smallest instability amplitude at stagnation. Like in the experiment, this difference in instability amplitude at stagnation will only become more prominent as the convergence ratio increases.

The results presented in Fig. 4.30 (using Eq. 2.2) suggest that the stabilization has less to do with the rotation of the magnetic pitch angle (and the counter rotating plasma pitch angle) and more to do with the fact that the DSP cases resulted in larger final wavelengths than the SZP case. However, it may still be the case that the DSP stabilization is due to the counter rotating pitch angles, as predicted when applying the theory of [7], if our puffed-out shell thickness is large. Use of very thick shells (> 500 µm) resulted in the relative stabilization of the theory matching well with experiments even when the same initial and final λ values are used across all SZP and DSP cases (see Fig. 4.31). In order to answer this, a good measurement of the puffed out shell thickness (perhaps from penetrating X-pinch radiography) is needed. This question will need to be addressed in future work.

The overall implosion convergence observed in these experiments ($C_r = 2$) is relatively small, compared to the MagLIF program, which is interested in maintaining stability up to $C_r = 4$–10 (for the liner's outer surface). However, the relative stabilization obtained using the DSP configurations is only expected to increase with further increases to C_r and $\hat{d}$ [67]. The trends in the data are clear, increasing the ratio of magnetic field strengths, B_z/B_θ, decreases the instability amplitude at stagnation. Moreover, if we extrapolate to higher convergence ratios, these differences in the instability amplitudes from one return-current case to the next are expected to increase even further. The results presented are an extreme case, since the thin-foil liners are so unstable to begin with ($A_{r0} \approx 4,900$ for these thin-foil liners versus $A_{r0} \approx 6$ for MagLIF).

This huge difference in aspect ratio, which was discussed in Chapter 3, calls into question how relevant these experiments are to MagLIF, or any thick-shelled liner experiment. Again we note that experiments in the high-aspect-ratio/thin-foil regime have already demonstrated relevancy to the low-aspect-ratio regime that MagLIF operates in. Thin-foil experiments at

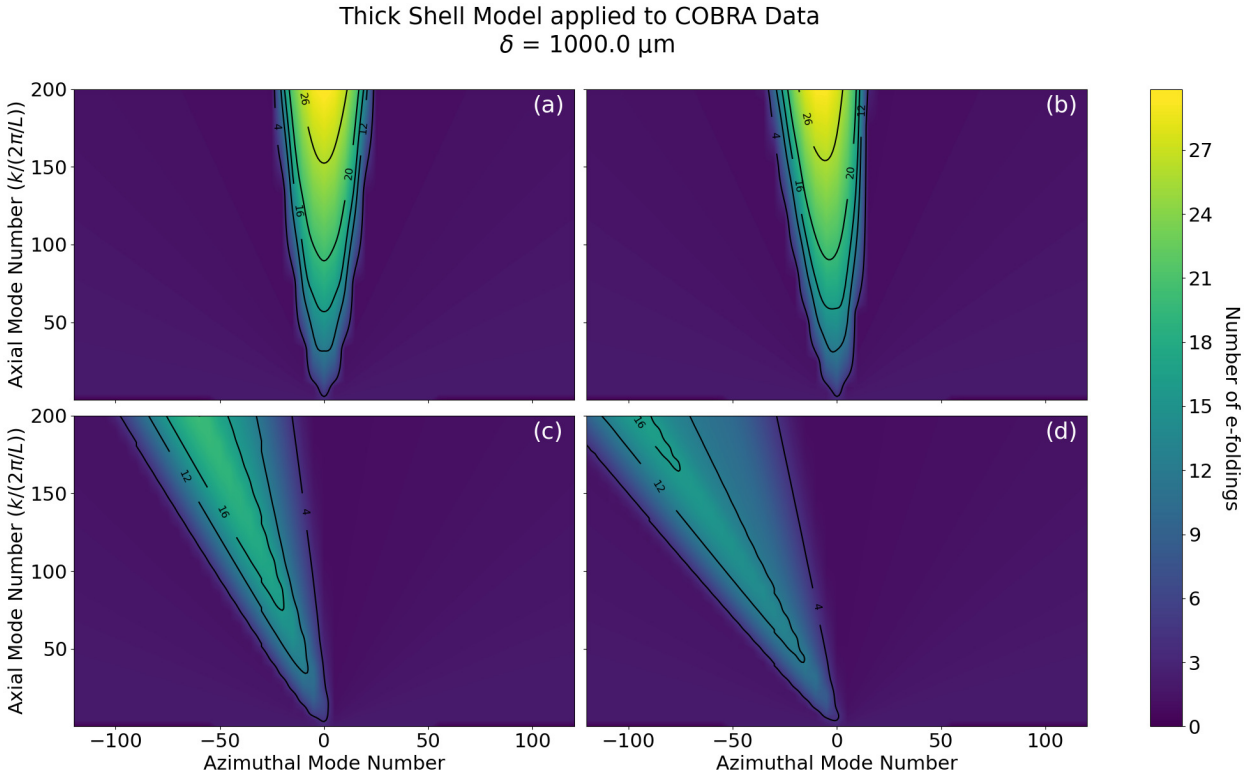

Figure 4.22: Contour plots of the cumulative instability growth, Γ (number of e-foldings), for the four experimental cases tested, assuming a liner thickness of 1000 µm. The e-foldings are calculated the using thick-shell Velikovich and Schmit theory [7] across a wide range of azimuthal mode numbers, m, and normalized axial wave numbers, $\hat{k} = k_z/(2\pi/L)$, where L is the axial length of the liner (1 cm). (a) The SZP case. (b) The low-field DSP case. (c) The mid-field DSP case. (d) The high-field DSP case.

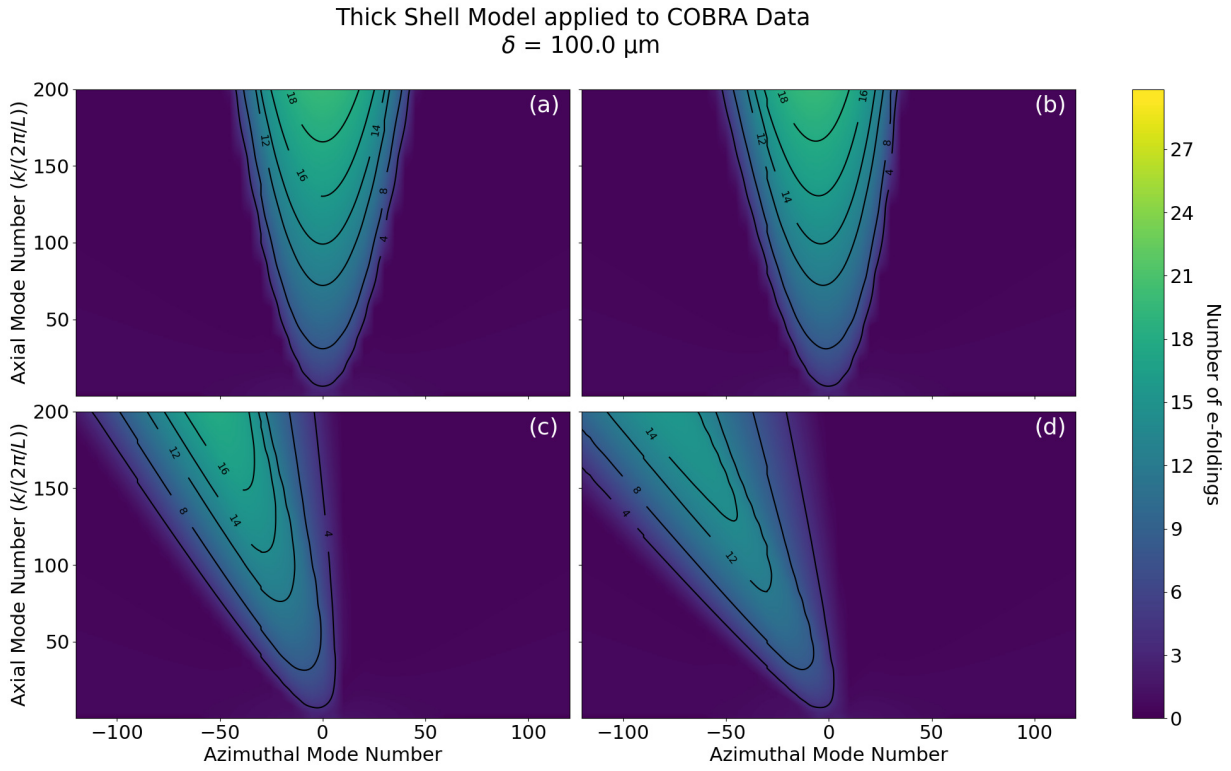

Figure 4.23: Contour plots of the cumulative instability growth, Γ (number of e-foldings), for the four experimental cases tested, assuming a liner thickness of 100 µm. The e-foldings are calculated the using thick-shell Velikovich and Schmit theory [7] across a wide range of azimuthal mode numbers, m, and normalized axial wave numbers, $\hat{k} = k_z/(2\pi/L)$, where L is the axial length of the liner (1 cm). (a) The SZP case. (b) The low-field DSP case. (c) The mid-field DSP case. (d) The high-field DSP case. Note that the color map is scaled the same as in the 1000-µm-thick case.

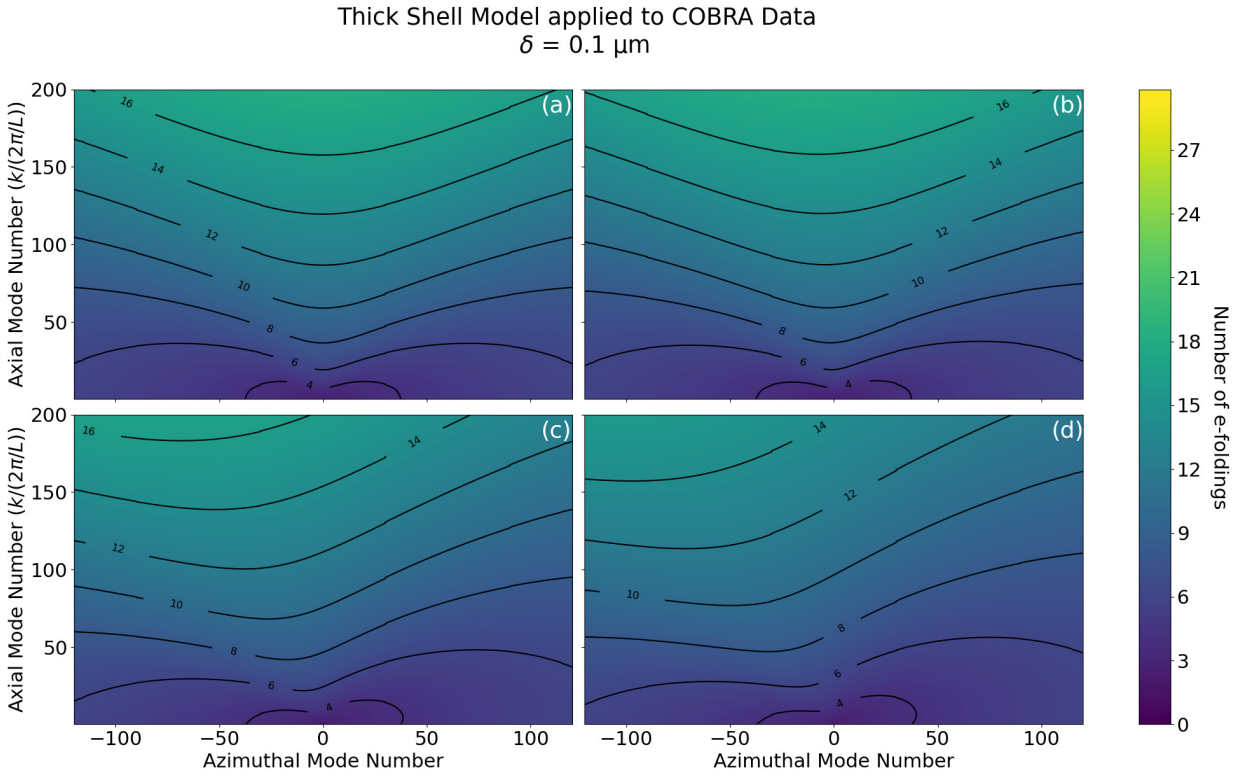

Figure 4.24: Contour plots of the cumulative instability growth, Γ (number of e-foldings), for the four experimental cases tested, assuming a liner thickness of 0.1 µm. The e-foldings are calculated the using thick-shell Velikovich and Schmit theory [7] across a wide range of azimuthal mode numbers, m, and normalized axial wave numbers, $\hat{k} = k_z/(2\pi/L)$, where L is the axial length of the liner (1 cm). (a) The SZP case. (b) The low-field DSP case. (c) The mid-field DSP case. (d) The high-field DSP case. Note that the color map is scaled the same as in the 1000-µm-thick case.

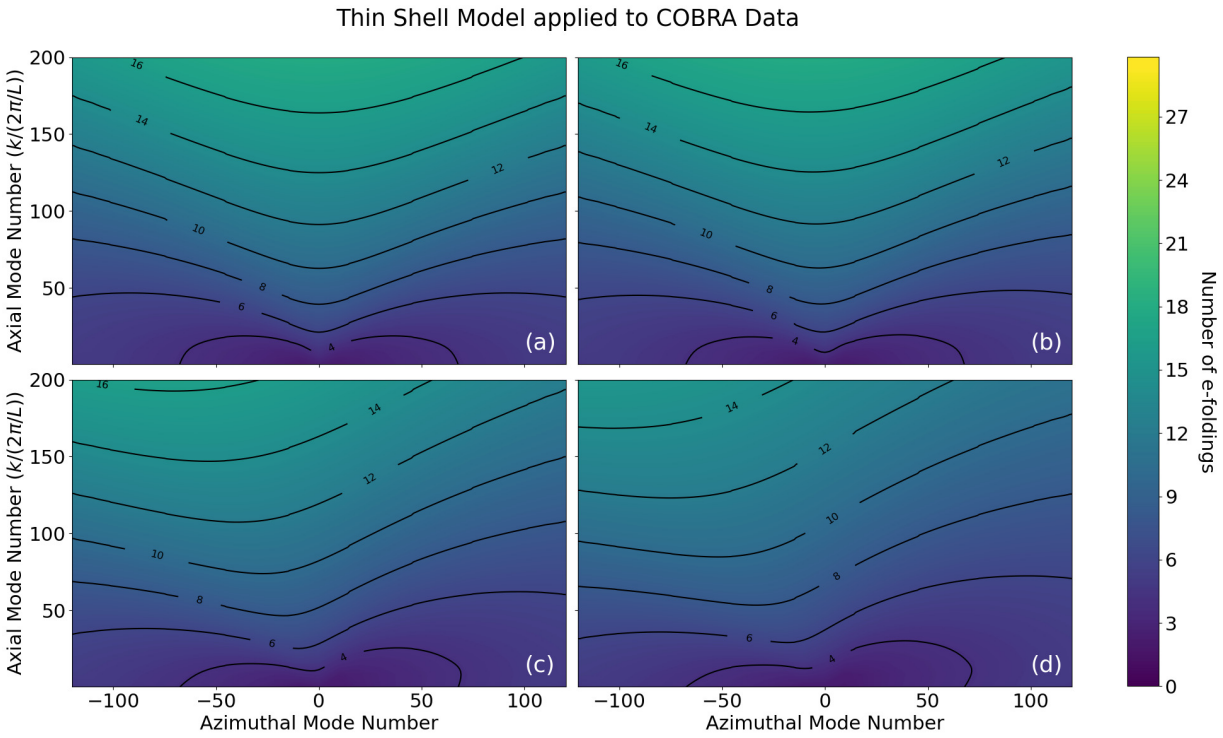

Figure 4.25: Contour plots of the cumulative instability growth, Γ (number of e-foldings), for the four experimental cases tested, assuming an infinitesimally thick liner. The e-foldings are calculated using the thin-shell Velikovich and Schmit theory [7] across a wide range of azimuthal mode numbers, m, and normalized axial wave numbers, $\hat{k} = k_z/(2\pi/L)$, where L is the axial length of the liner (1 cm). (a) The SZP case. (b) The low-field DSP case. (c) The mid-field DSP case. (d) The high-field DSP case. Note that the color map is scaled the same as in the 1000-µm-thick case.

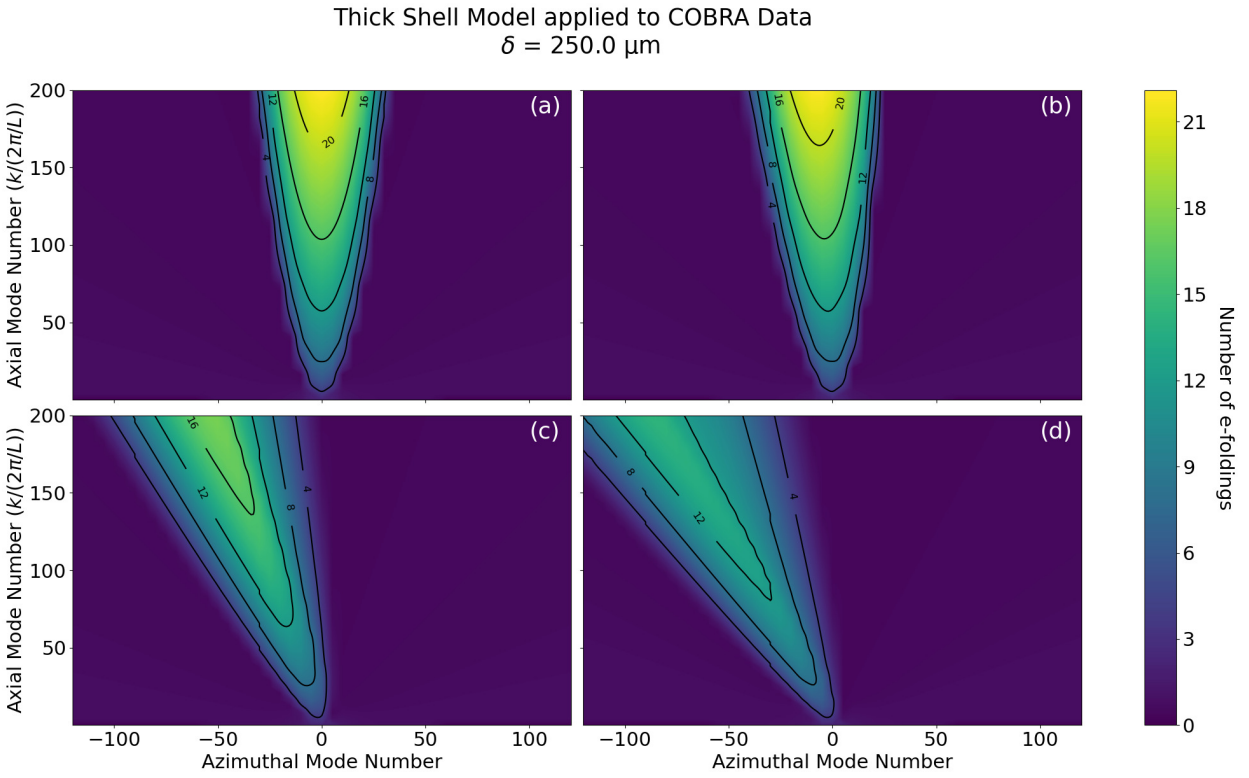

Figure 4.26: Contour plots of the cumulative instability growth, Γ (number of e-foldings), for the four experimental cases tested, assuming a liner thickness of 250 µm. The e-foldings are calculated the using thick-shell Velikovich and Schmit theory [7] across a wide range of azimuthal mode numbers, m, and normalized axial wave numbers, $\hat{k} = k_z/(2\pi/L)$, where L is the axial length of the liner (1 cm). (a) The SZP case. (b) The low-field DSP case. (c) The mid-field DSP case. (d) The high-field DSP case. Note that the color map is rescaled for this case.

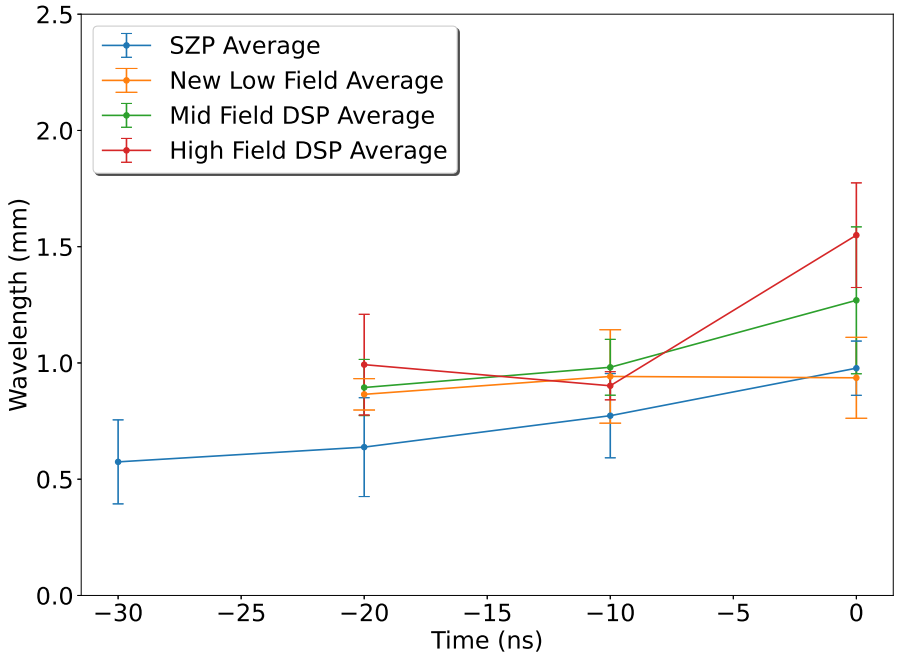

Figure 4.27: A plot of the axial instability wavelength growth as a function of time until liner stagnation (t=0 corresponds to when the liner stagnates).

650 kA have found both $m \approx 0$ instability structures for SZP cases with no applied axial field and more stable $m \approx 2$ helical structures for SZP cases with an externally applied $B_{z0} \approx 2$ T [55, 56]. This is likely due to the fact that MRTI growth is governed primarily by the acceleration history of the implosion [44], so a MagLIF-relevant implosion trajectory should result in MagLIF-relevant MRTI growth, even at drastically different aspect ratios. Finally, recall that with $\delta_0 \sim 500$ nm, these thin foils should be highly susceptible to instability feedthrough ($A_{r0} \sim 6,000$). However, because $\delta_e \gg \delta_0$ (initially), ohmic heating causes the thin foils to rapidly expand to $\delta \sim$ 100–1000 µm prior to the implosion [70, 71], thus lowering the *effective* A_{r0} to 3–30.

Finally we will comment on how both the liner thickness and final wavelength effect the instability growth. As seen in Fig. 4.31, the spread in predicted amplitudes between the four experimental cases increases as the liner thickness increases. When fixing the final instability wavelength (not axial, total) λ_f to 1 mm, this also decreases the spread in predicted amplitudes with respect to the case where the final instability wavelength values are allowed to vary with $\lambda_f \geq 1.0$ mm, as shown in Fig. 4.28. These cases demonstrate the sensitivity of the theory to the choice of these parameters.

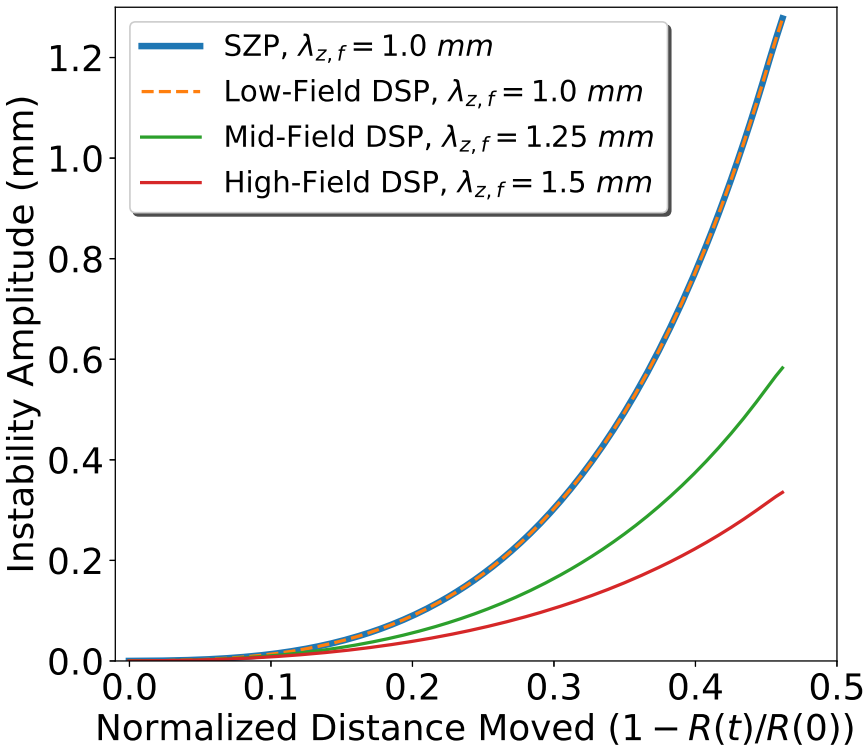

Figure 4.28: A plot of the relative instability amplitude growth of a dominant perturbation structure with a pitch angle that rotates according to our experimentally observed $\phi_{plasma}(t)$. These plots were generated using the thick-shell Velikovich and Schmit theory [7], assuming a liner thickness of 250 µm. In applying the instability growth model, the initial perturbation wavelengths were all set to 50 µm, and the initial perturbation amplitudes were all set to 60 nm.

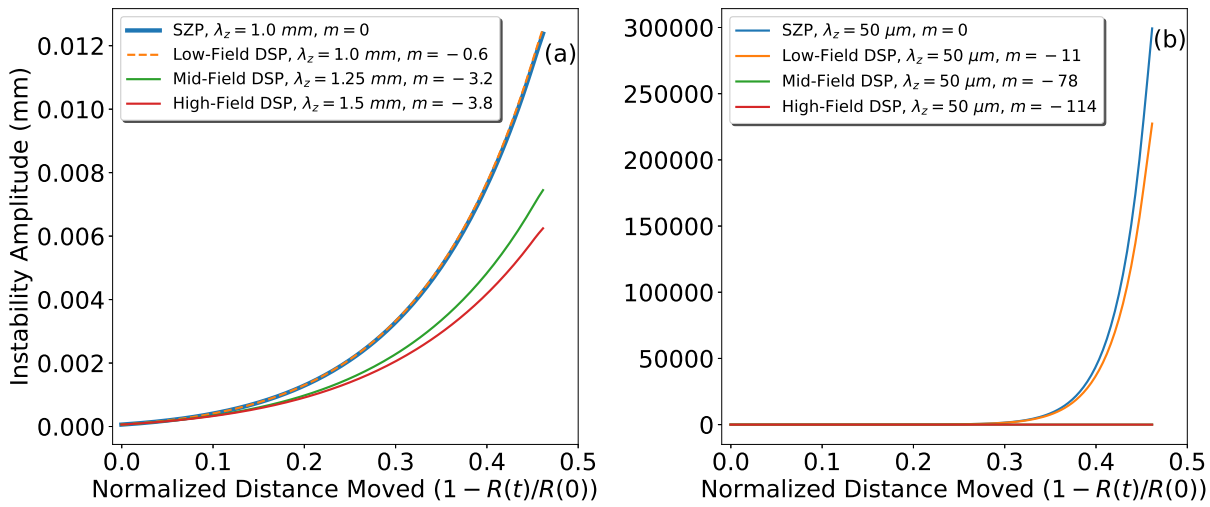

Figure 4.29: Plots of the relative instability amplitude growth of a dominant perturbation structure with constant mode numbers m and k_z taken at the end (a) or start (b) of the plasma pitch angle rotation according to our experimentally observed $\phi_{plasma}(t)$. These plots were generated using the thick-shell Velikovich and Schmit theory [7], assuming a liner thickness of 250 µm. In applying the instability growth model, the initial perturbation wavelengths were all set to 50 µm, and the initial perturbation amplitudes were all set to 60 nm.

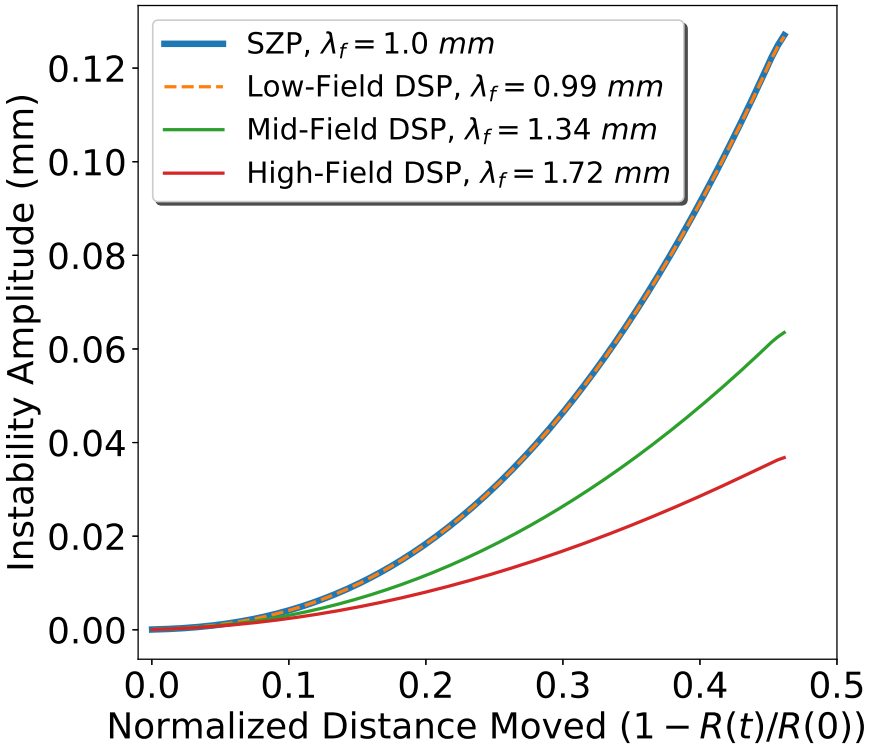

Figure 4.30: A plot of the relative instability amplitude growth of a dominant perturbation structure, calculated using $\gamma = \sqrt{k_z g}$, where the evolving k_z used was the same as that used in our evolving $\phi_{plasma}(t)$ model. In applying this instability growth model, the initial perturbation wavelengths were all set to 50 µm, and the initial perturbation amplitudes were all set to 60 nm.

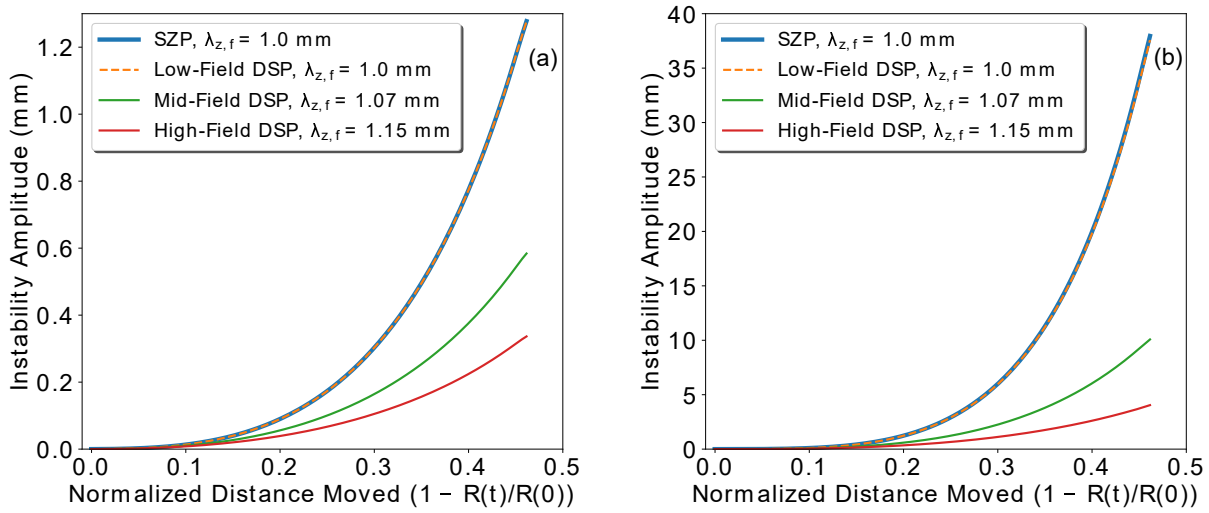

Figure 4.31: Plots of the relative instability amplitude growth of a dominant perturbation structure with constant λ_f values at two different liner thicknesses (a) 250 m and (b) 1000 m. The mode numbers m and k_z still vary according to the pitch angle rotation obtained from our experimentally observed $\phi_{plasma}(t)$. These plots were generated using the thick-shell Velikovich and Schmit theory [7]. In applying the instability growth model, the initial perturbation wavelengths were all set to 50 µm, and the initial perturbation amplitudes were all set to 60 nm.

4.3 Power Flow

Regarding power coupling, we note that when comparing across similar current pulses (e.g., considering only short pulse shots), the DSP cases often stagnated 10–40 ns earlier than the z-pinch cases (see Table 4.3). Simple thin-shell implosion modeling (0-D) indicates that shot-to-shot variations in current delivery ($\sim$10%) can only account for about 5–10 ns of variation in stagnation times. Thus, the earlier stagnation times may indicate increased power coupling, as predicted in Refs. [52, 53]. This is further supported by the fact that the images recorded for the DSP cases were significantly brighter than for the SZP case. This can be seen by comparing the saturated mid-field results with the unsaturated SZP results in Fig. 4.15. Note that the same ICCD gain settings were used throughout Fig. 4.15, but a neutral density filter (ND= 0.6) was added for the low and high-field cases to avoid saturating the ICCD.

When conducting the stagnation time analysis it became clear that the simple thin-shell model (0D) was reaching C_r=2 much earlier than the experiment, by about 70 ns. It was only after turning down the current to about half strength that the stagnation times matched up. This could be happening for a couple of reasons. First, the thin-shell model only accounts for the inward Lorentz force and not for potential sources of back pressure, such as the ablated, coronal "precursor" plasma that is injected into the liner interior prior to the bulk of the liner shell imploding [87]. The precursor plasma also likely carries along with it some of the driving magnetic field [68]. The field that is advected into the liner interior is no longer available to drive the implosion of the bulk of the liner shell; instead, the flux that is advected into the liner interior becomes a source of back pressure on the imploding shell, due to flux compression (i.e., the bulk of the imploding liner shell has to do work on the magnetic field to compress the flux). Second, the experiment might not actually be driving the full 1 MA through the liner. The Rowogiski coil is located in the power feed, so it is possible that there is some current loss between the load and the Rogowski coil. It is also possible that the inner dielectric support rod flashes over and provides a current conduction channel along the surface of the rod. However, even if the rod does not flash over, the injected precursor plasma will eventually accumulate along the surface of the rod and provide a path for axial current conduction along the surface of the rod. The self-generated magnetic field associated with this axial current provides the magnetic back pressure discussed above.

A second observation relevant to power flow dynamics is revealed by the drive-current waveforms from the first COBRA run in Fig. 4.33. For a given configuration, the current waveforms were very reproducible. However, for the SZP case, the Rogowski coil appears to short out (or become shielded by plasma) around 300 ns (as indicated by these time-integrated

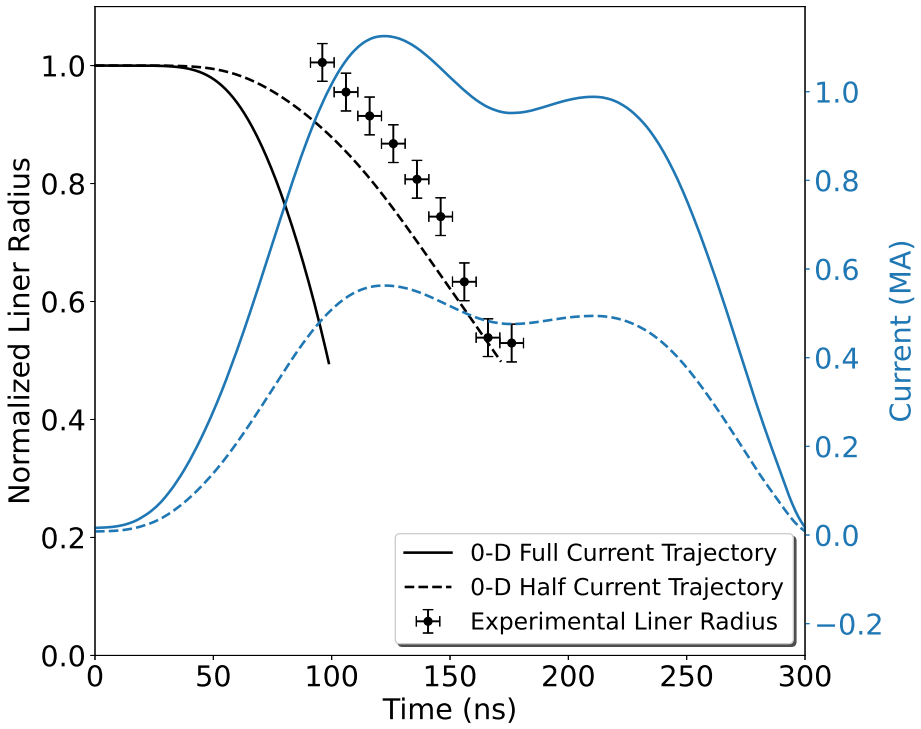

Figure 4.32: A plot the experimental radii from shot 5396, a 14-T DSP shot, along with the trajectories predicted by the simple thin-shell model for the full and half drive currents.

Table 4.3: A comparison of stagnation times between the experimentally observed values and the simple thin-shell model. Note that only short pulse shots from the second experimental run are used for this analysis. We also excluded the low-field DSP shots from this analysis since the effect from its additional axial field component is so small.

Shot No.	Exp. Time (ns)	Model Time (ns)	Model, with B_z Time (ns)
		SZP shots start	
05393	203	106	106
05394	197	100	103
Avg.	200 ± 3	103 ± 3	103 ± 3
		Mid-field DSP shots start	
05396	181	99	68
05397	173	95	63
05400	185	92	61
05402	159	96	65
Avg.	174.5 ± 9.9	95.5 ± 2.5	64.3 ± 2.6
		High-field DSP shots start	
05407	160	90	53

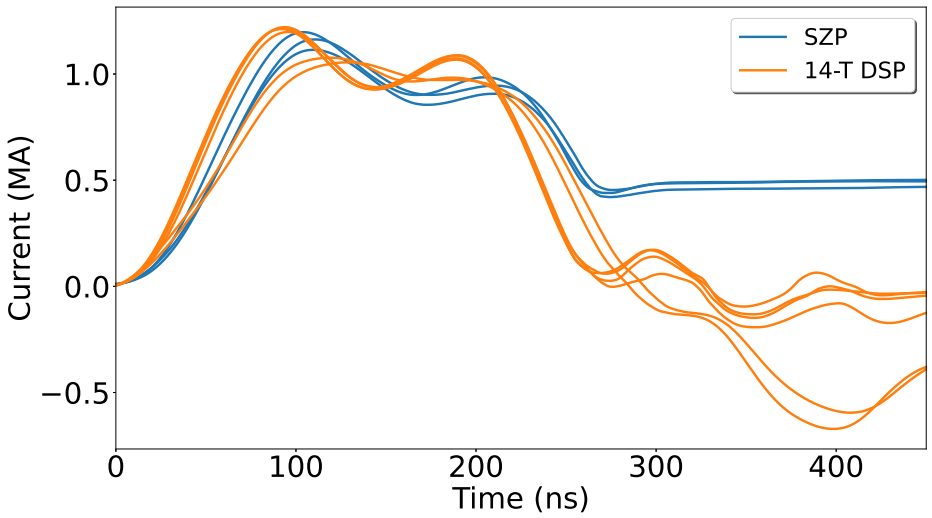

Figure 4.33: A plot of several SZP and mid-field DSP drive currents from the first shot series on COBRA. These plots illustrate the effects that the DSP configuration has on late-time load-current measurements and possibly on power flow after peak current.

signals not returning to zero). One explanation of this behavior [88, 89, 5, 13] is that power flow and low-density plasma flow change direction with voltage reversal (and thus with the reversal of the electric field $\mathbf{E}$), which occurs after peak current in these pulsed inductive systems (see Fig. 4.34). In the SZP case, the direction of $\mathbf{E} \times \mathbf{B}$ drift (which is the same direction as the Poynting vector for describing electromagnetic power flow) after peak current is away from the imploding liner. This drives low-density liner plasma back towards the Rogowski coil, which is located in the power feed a few cm away from the liner. In most of the DSP experiments, however, the Rogowski coil continues to measure the drive current for the duration of the pulse. This may indicate that the DSP configuration prevents low-density liner plasma from moving out into the power feed towards the Rogowski coil.

To further study this phenomena, and to check how accurate our simple picture of the power feed is, electromagnetic simulations in CST EM studio were performed. A geometrically simple power feed was constructed in the simulation using the gap spacings of the COBRA power feed. The simulation drives a prescribed, 1-MA, 100-ns rise time, current pulse through the system at the bottom of the power feed, and is double checked against current and voltage monitors placed throughout the power feed. Open boundary conditions are used at five of the six simulation boundaries. The boundary where the bottom of the power feed sits is kept at ground.

In Fig. 4.35, electromagnetic simulation results are presented for the SZP configuration (straight return current posts). This figure shows snapshots taken at five different times during the current pulse. We see that before peak current is reached, the Poynting vector

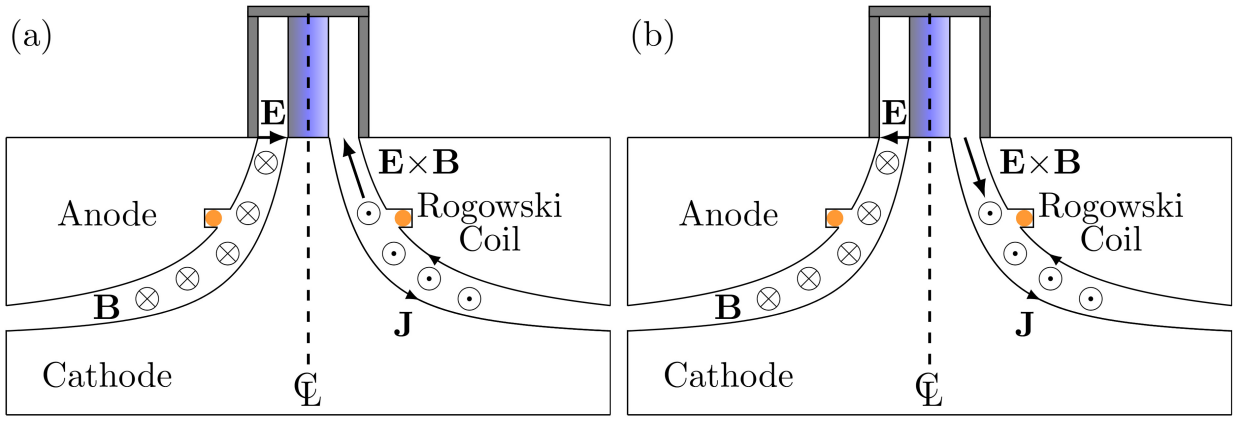

Figure 4.34: Illustrations of the power feed in the SZP case, and the **E**×**B** or Poynting vector at two times during the current pulse. (a) During the current rise, near the top of the swooping power feed, the electric field points radially inward and so **E**×**B** points upwards at this location. (b) During the falling edge of the current pulse (after peak current), the electric field vector has flipped directions and, at the top of the swooping power feed, now points radially outward. Thus, **E**×**B** points down the power feed, towards the Rogowski coil.

points up the power feed toward the load region. After peak current, the direction of the Poynting vector flips and points back down into the power feed. This is consistent with our simple picture of the power feed, but what happens when a DSP return current structure is used?

In Fig. 4.36, electromagnetic simulation results are presented for the mid-field DSP configuration (helical return-current structure). Again, snapshots from five different times during the current pulse are shown. From the simulation, we see very similar behavior to the SZP case. It is not clear that the Ponyting vector is at all perturbed near the mouth of the power feed. One difference is that the DSP return current structure does block a significant amount of area at the mouth of the power feed that was clear in the SZP case.

Next, we add charged particles (electrons) to the simulation to see how they behave. These electrons are initialized with a Maxwellian distribution centered at 10 eV, in a cylindrical shell around the liner, since most of the plasma in our experiments should be sourced from the ablated thin-foil liner. Electrons are added in bunches of a thousand to the simulation every 10 ns, starting at 70 ns, and stopping at 170 ns with a Maxwellian distribution centered at 10 eV. Space-charge effects are included in this simulation but have a negligible effect due to the small number of particles (thousands) in the simulation. For the SZP case, Fig. 4.37 shows snapshots of the PIC simulation at 5 different times. Prior to peak current, we see electrons bunching around the liner region and staying confined to that region. It is not until 160 ns into the simulation that we see a drift in the electron bunch. As the simulation continues, all of the electrons pour down into the power feed.

Simulations for the mid-field DSP case are shown in Fig. 4.38. Interestingly, no matter what time during the simulation we look at, electrons are continuously ejected radially outward from the load region. It appears that if the electrons move too far away from the liner, the fields in between the helical return current posts move the particles out, and away from the power feed. At later times, we see very few particles make their way into the power feed.

We now look at the drive-current waveforms from the second COBRA run in Fig. 4.39. Again, we see the current traces in the SZP case flatlining, but at later times than in the first shot series (by roughly 50 ns; Fig. 4.33). One reason this could be occurring is if the power feed hardware was for any reason cleaner during the second run than the first, less feed plasma would be generated in the power feed and lead to the shielding of the Rogowski coil. Another potential reason is that the hardware was slightly modified in between experimental runs. A spacer was used during the second experimental run to raise the height of the return-current structures. This was done to move the experiment into the center of diagnostic's viewing region (so that the diagnostics were not being used at the end of their adjustable range). This additional height changed the distance the plasma sourced at the load region had to travel in order to make it to the Rogowski coil.

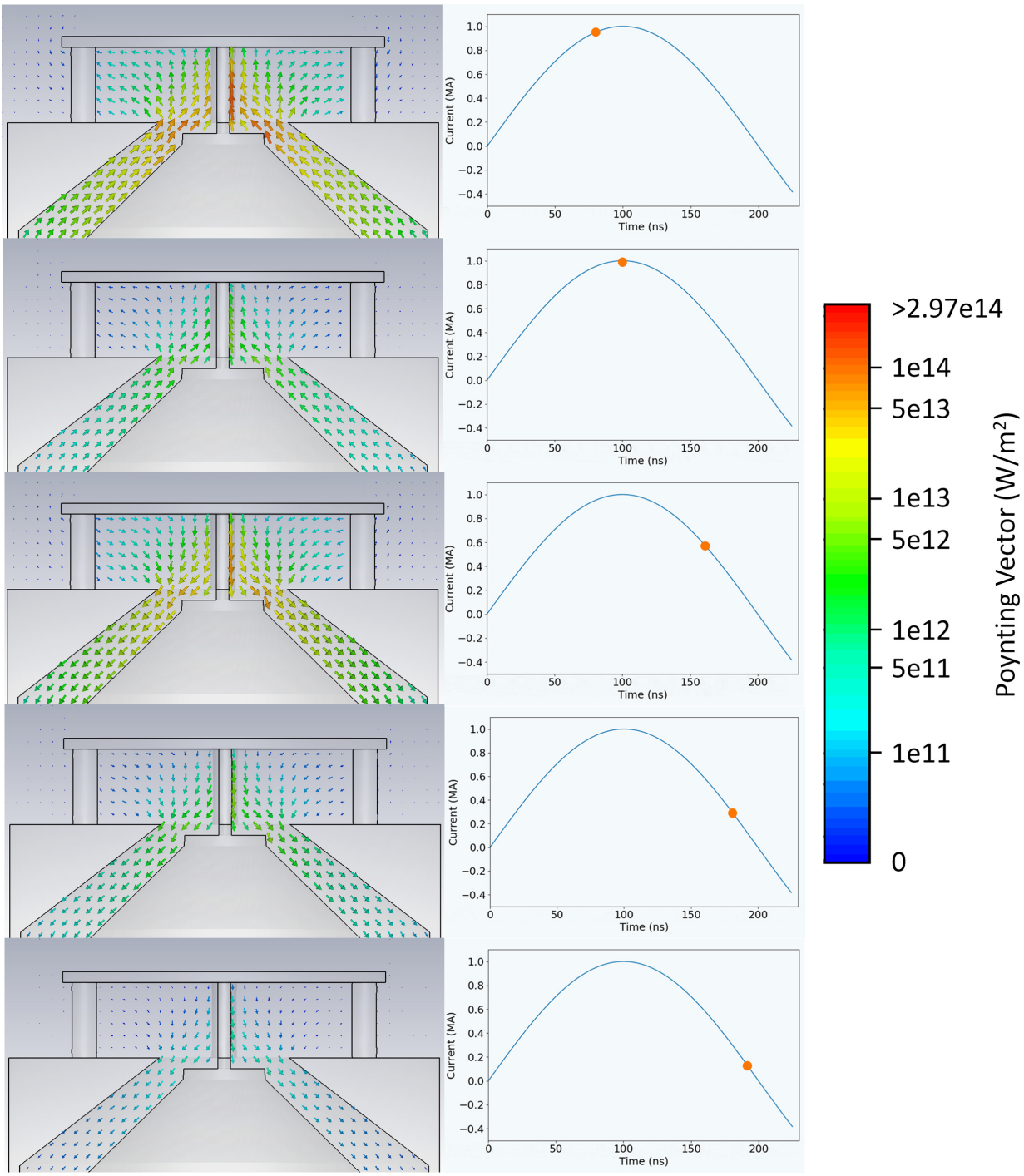

Figure 4.35: Screen shots of an electromagnetic simulation of a power feed with a standard, straight-post, return-current structure on top (SZP case) and the simulation's driving current pulse. The arrows show the orientation of the Poynting vectors, as projected onto the cross-sectional plane. They point up the power feed towards the load before peak current, while after peak current, they have flipped direction and point down the power feed (towards where the Rogowski coil would be located in a COBRA experiment).

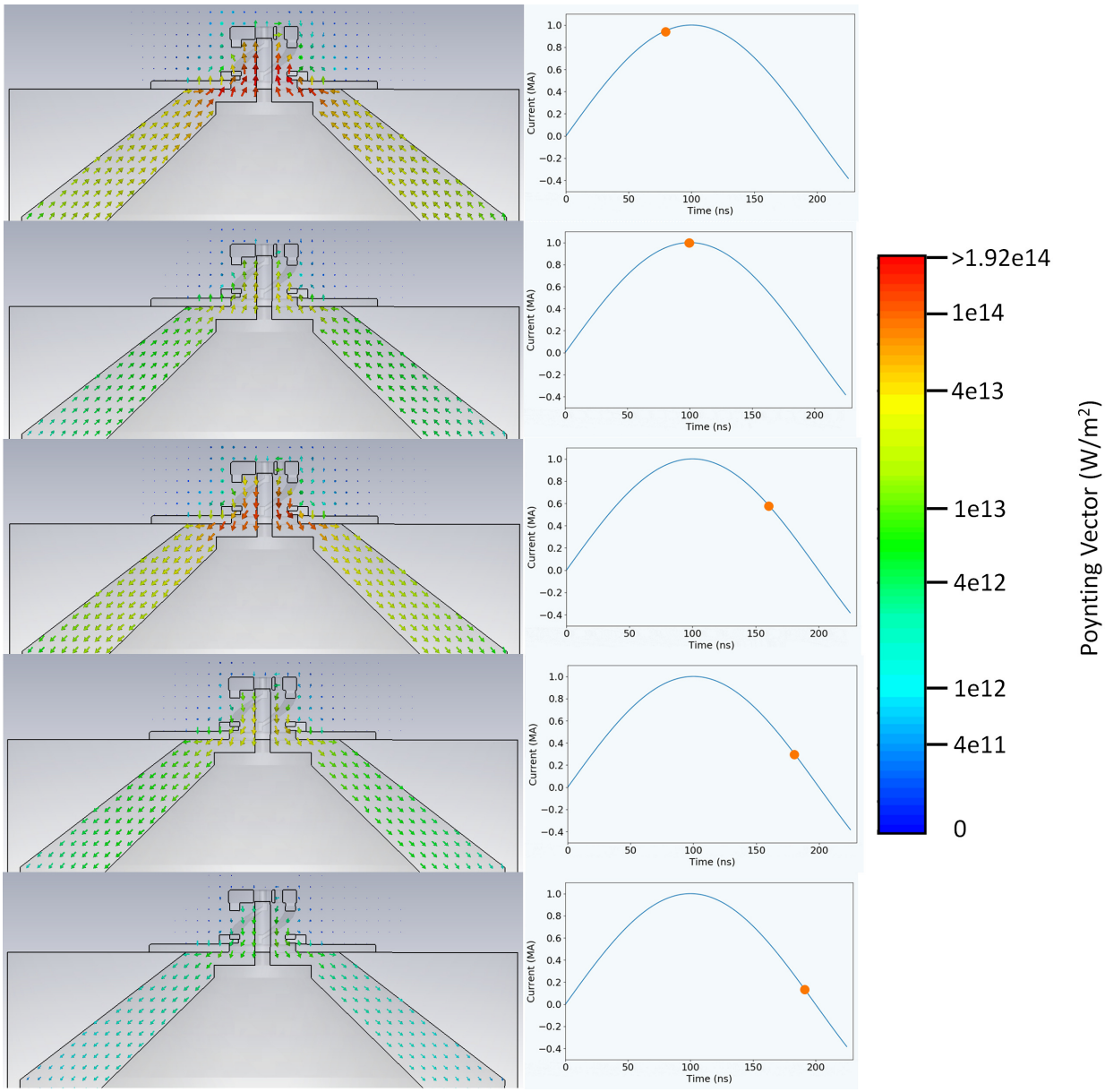

Figure 4.36: Screen shots of an electromagnetic simulation of a power feed with the mid-field DSP return-current structure on top and the simulation's driving current pulse. The arrows show the orientation of the Poynting vectors, as projected onto the cross-sectional plane. They point up the power feed towards the load before peak current, while after peak current, they have flipped direction and point down the power feed (towards where the Rogowski coil would be located in a COBRA experiment). In this case many of the arrows point into the part of the return-current structure that juts out over the power feed's gap.

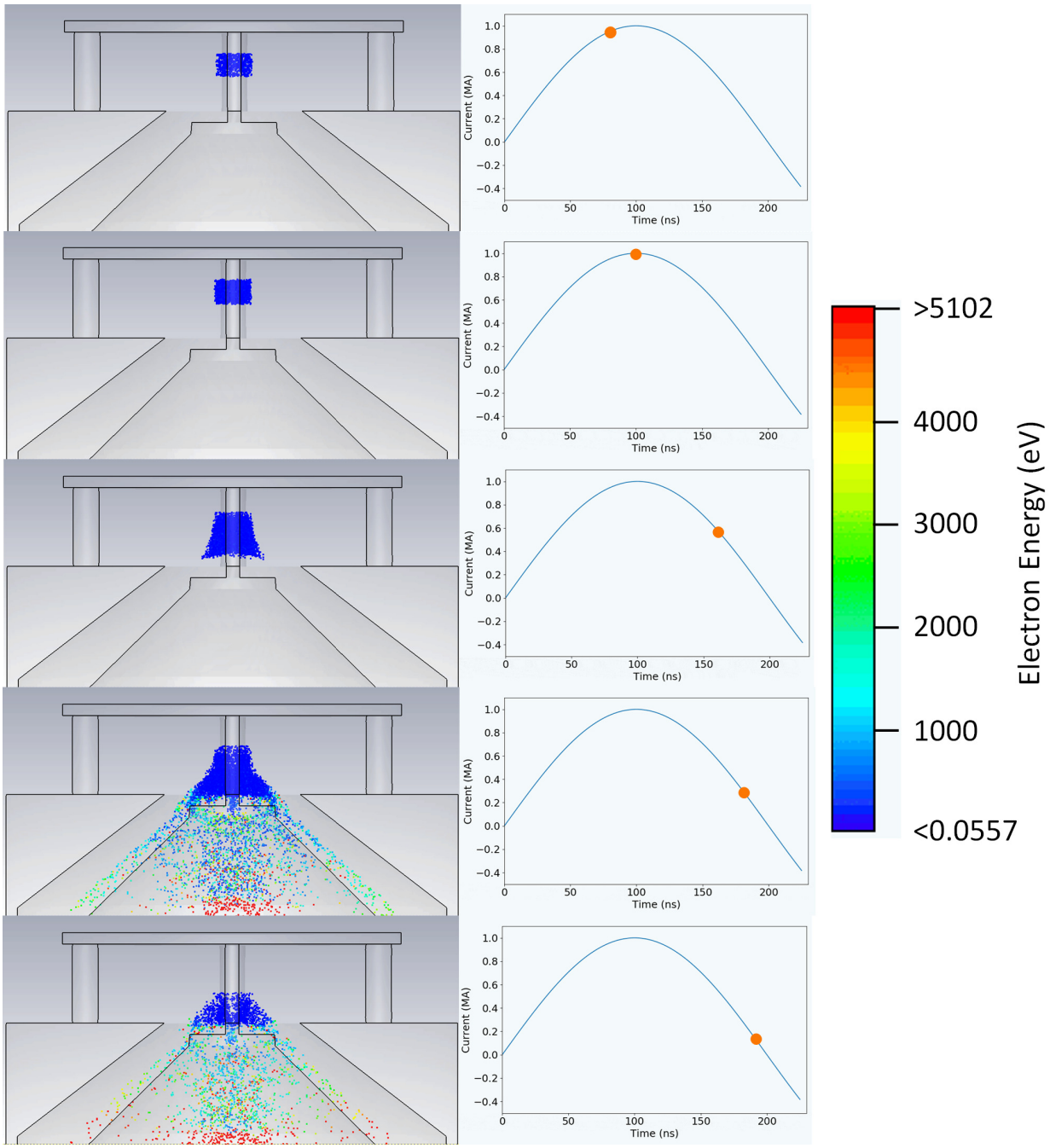

Figure 4.37: Screen shots of a particle-in-cell (PIC) simulation of a power feed with a standard, straight-post, return-current structure on top (SZP case) and the simulation's driving current pulse. The colored dots represent electrons, which are initialized with a Maxwellian distribution centered at 10 eV, in a cylindrical shell around the liner. During the current rise, these electrons remain confined near their initial positions, but after voltage reversal, they begin to be forced down the power feed (towards where the Rogowski coil would be located in a COBRA experiment).

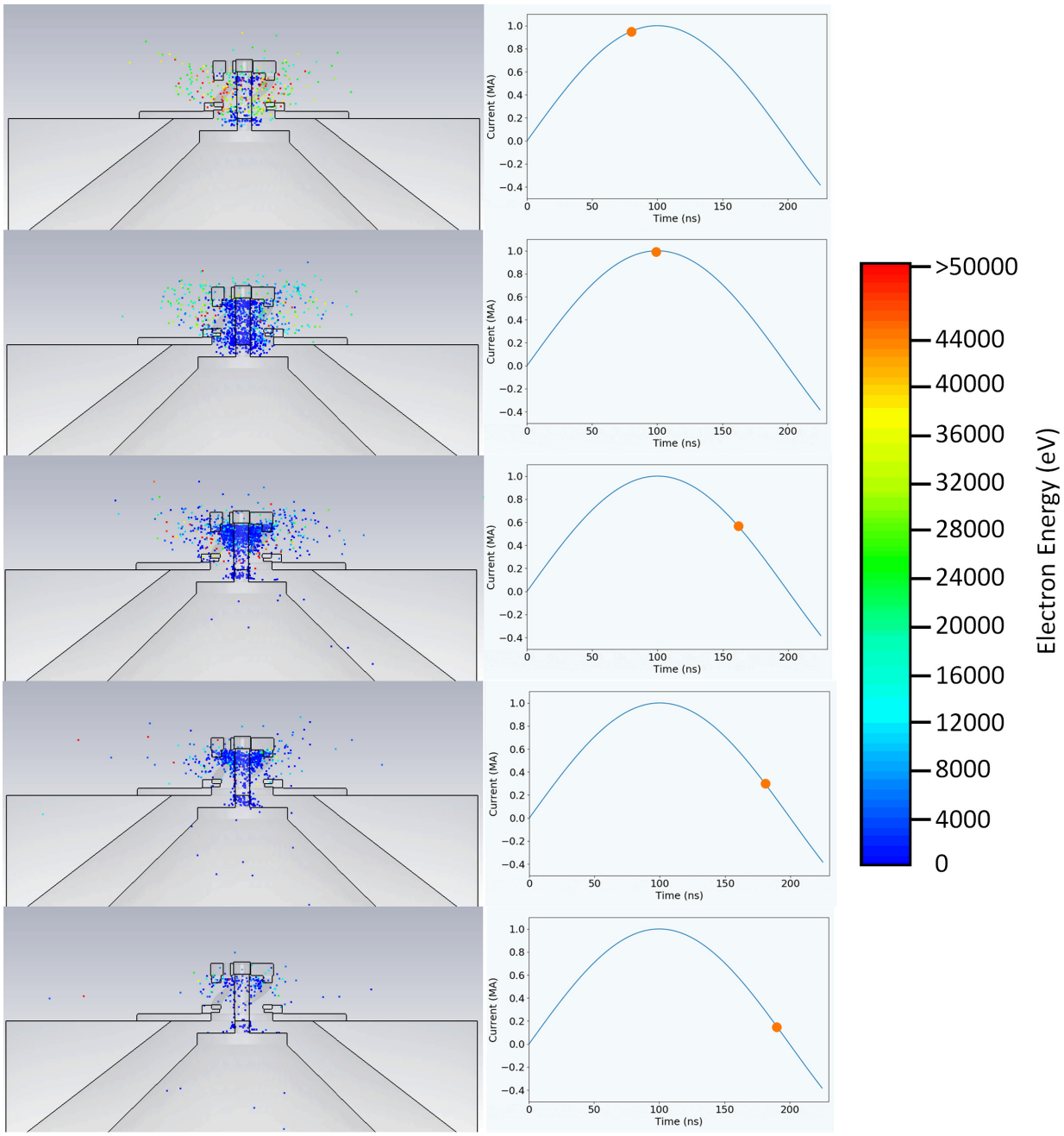

Figure 4.38: Screen shots of a particle-in-cell (PIC) simulation of a power feed with the mid-field DSP return-current structure on top and the simulation's driving current pulse. The colored dots represent electrons, which are initialized with a Maxwellian distribution centered at 10 eV, in a cylindrical shell around the liner. During both the current rise and fall, the particles are continuously ejected out of the load region, through the gaps in the return current structure, with very few electrons making their way into the power (where the Rogowski coil would be located in a COBRA experiment).

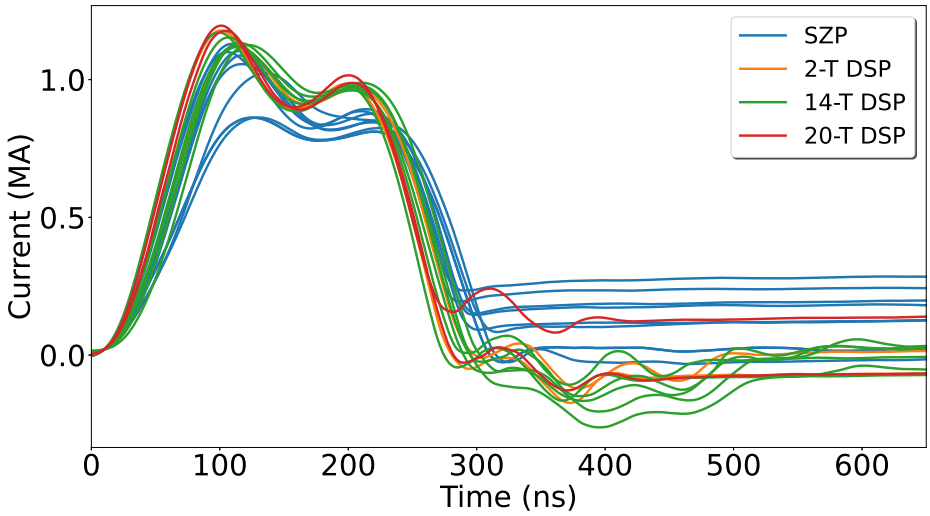

Figure 4.39: A plot of several SZP and DSP drive currents from the second shot series on COBRA. These plots illustrate the effects that the DSP configuration has on late-time load-current measurements and possibly on power flow after peak current.

CHAPTER 5

Conclusions

The first experimental tests of the dynamic screw pinch, presented in this dissertation, have demonstrated enhanced stability in ultra-thin liner implosions. These results (the degree of relative stabilization from one SZP/DSP case to the next) agree reasonably well with the Velikovich and Schmit theory [7], and in the strongest DSP case tested, showed a factor of three reduction in instability amplitude at a convergence ratio of 2. Specifically, at $\hat{d} = 0.5$ ($C_r = 2$), the MRTI amplitudes for the SZP case and for the 14-T and 20-T DSP cases were, respectively, 1.1±0.3 mm, 0.7±0.2 mm, and 0.3±0.1 mm. While the convergence ratio of the experiments was low, relative to other imploding liner experiments, the trends in the data were clear; when the DSP generates stronger axial magnetic fields, the instability amplitude decreases. This trend should continue in cases where the liner implodes past a convergence ratio of two, and amplify the stabilizing effects of the DSP further.

Micro B-dot probe measurements showed that the return-current structures in the DSP cases generated axial magnetic field values line with the values predicted by electromagnetic simulations in CST. Measurements taken inside the liners themselves showed a significant amount of flux injection and compression. Based on previous probe failure signatures, it is unlikely that the micro B-dot probes failed early in the implosion and read erroneous amounts of flux compression. A model using the time when the liner shifts from a diffusive to advective regime, along with an estimate of the position of the liner's inner surface, underpredicted the measured values. While we can be fairly confident that we are indeed measuring flux compression, more detailed models, or further experimentation, will be needed to confirm the accuracy of the measurement.

Analysis of the stagnation times and current waveforms from short-pulse shots on COBRA demonstrated that the small difference in current delivery was not enough to account for the measured differences in stagnation time. It is likely that the the mid-field and high-field DSP shots imploded faster due to the added magnetic pressure from the DSP. Analyzing the currents further showed that the type of return-current structure used affected the way the Rogowski coil measured current. Electromagnetic simulations of the power feed confirmed

the direction of the Poynting vector during both the current rise and fall but, did not help illuminate why the Rogowski coil might produce a difference signal in the DSP case versus the SZP case. Preliminary PIC simulations showed that the mid-field DSP return-current structure ejected electrons radially outward resulting in a minute number of electrons making their way into the power feed. The SZP case showed substantial amounts of electrons being pulled down into the power feed. This behavior likely causes the Rogowski coil to be shielded in the SZP case leading to the flatlined signal that is absent in the DSP case.

Our experiments on COBRA have demonstrated that the DSP configuration is a relevant concept for liner stabilization. We have also confirmed the preliminary simulation and theory work done by Schmit et al. [52] and Velikovich and Schmit [7]. While MagLIF was the motivation behind the development of this concept, any liner implosion experiment needing more stable interfaces could benefit. Additionally, the power flow and magnetic flux compression results might be of interest to non-fusion-related z-pinch research. The effects that the DSP has on liner implosions are profound, and hopefully this work will be a foundation for further exploration into the uses of the DSP. At the time of this writing two DSP shots have been fielded on the Z machine, and the published results are eagerly awaited.

CHAPTER 6

Future Work

Much simulation work is needed to help understand the physics of the DSP. Primarily, high-resolution, 3-D, MHD simulations are needed to compliment the linear perturbation theory analysis currently available. In addition to furthering the understanding of the instability growth, these simulations could help with interpretation of the flux compression results. While some simulation work has been done to explore how quickly magnetic field lines are transported across both ultra-thin foil liners [64] and thick-walled liners [68, 54], the simulations done in ALEGRA by [67] and in PERSEUS [54] do not agree on how quickly this process should happen. It is unclear whether this difference arises from the fact that one code uses resistive MHD equations (ALEGRA) while the other uses extended MHD equations (PERSEUS), or from any number of differences between the codes. Understanding the mechanisms that facilitate flux compression will be key for the MagLIF concept if, as suggested in Ref. [54],the premagnetization step in MagLIF may no longer be needed, since field lines are transported sufficiently quickly when a DSP is used.

These simulations would be the fastest way to quantify and study the nonlinear instability growth observed in our experiments, since no robust nonlinear MHDI theory currently exists for the DSP configuration with helical instability structures. Development of such a theory would be ideal for future work, although it is an ambitious undertaking. High-resolution, multi-physics simulations can take thousands of CPU hours to run a single liner implosion. Using an analytic or semi-analytic framework would certainly be a faster way to predict and design experiments as well as making comparisons to experimental data. This is of course in addition to any new understanding of the physics that a new model might contain, such as new scaling laws.

Better PIC simulations are needed in addition to MHD simulations. In order to study the physics of power flow, a code designed to study power flow, like LSP, should be used. In addition to switching to a more robust simulation software, a few changes to the setup of the simulation itself should be added. Ions should be added in addition to the electrons, along with particles sourced not just in the load region, but also in the power feed region. This

combination of changes should provide more accurate modeling of the power feed, further verification of the preliminary simulations already performed for this dissertation, and a new in-depth understanding of the important physics in the power feed.

Due to these experiments being limited to only 1 MA, some less-than-ideal design choices were made, namely the choice of using 650-nm-thick aluminum foil for the liner material. While COBRA is capable of driving slightly more massive liners, the underlying problems of using ultrathin liners remain. First, these foils are delicate, crinkle easily, and are thus full of instability seeds. While this is acceptable for studying the effects of mitigating MHDI instability growth, crinkles could seed random long-wavelength instabilities (long meaning on the order of the length of the liner) that are of less interest, since they do not arise from the inherent micro-physics of the system—e.g., electrothermal instabilities (ETI), which are believed to be the seed for MRTI in metal liner implosions, as well as current redistribution in metal liners due to resistive inclusions in the liner material, which can exacerbate ETI development [48, 90, 39]. In addition to potentially seeding unintended instabilities, the thin-foil liners are not massive enough to support themselves, so a support structure is needed. While the support structure could be redesigned to move the supporting dielectric rods outside the liner, this would lead to a whole new host of problems such as larger load inductances. The simpler solution to this problem is to just run the experiment with a more powerful pulsed power driver. An increase in current to 3–5 MA would be enough to field self-supporting liners, with thicknesses in the 10s of microns (for aluminum). This would eliminate the complication of the support rod and help mitigate effects due to the delicate nature of the liners themselves.

In addition to a higher current facility, a more comprehensive array of diagnostics would be key to subsequent experiments. Penetrating radiography would be an excellent addition, since this diagnostic would help assess the puffed out shell thickness, the amount of instability feed through, and the position of the liner's inner surface. New magnetic field diagnostics would also be a nice addition. While the micro B-dot probes used for the preliminary experiments were excellent diagnostics, there is always room for improvement. Fiber-coupled Zeeman spectroscopy [91] could be used to determine axial magnetic field strengths along the entire length of the liner, provided the fiber bundle is long enough, instead of just at a single point. The measurement would likely have to use a UV line, since the spectrum of light is a continuum in the visible region, based on liner temperature estimates. A fiber coupled Faraday rotation setup could provide a very nice measurement of the amount of flux compression inside the liner. While expensive and tricky to implement, in theory, the measurement should be more robust than using a calibrated micro B-dot probe. Finally, like with most experiments in HEDP, more shots to generate better statistics (for things like liner

stagnation time comparisons between SZP and DSP cases) are always helpful.

APPENDIX A

An Overview of the Thin-Shell ("0D") Model

The thin model captures the radial motion of the liner in one equation:

$$\ddot{r} = -\mu_0 h I^2/(4\pi m r) \tag{A.1}$$

where the current I can be either be a sine or sine squared wave (i.e. $I = I_0 \sin(wt)$ or $I_0 \sin^2(wt)$) depending on the machine being used. The current can also be a different shape, but these two are the most common. This is a 2nd-order, nonlinear, ordinary differential equation (ODE). Typically, when numerically solving 2nd order ODEs, the equation needs to be recast as two 1st-order ODEs:

$$\begin{aligned} \dot{r} &= v \\ \dot{v} &= -\mu_0 h I^2/(4\pi m r) \end{aligned} \tag{A.2}$$

When numerically solving differential equations, there is a notion of "stiffness". This refers to how sensitive the ODE solution is to the step sizes the solver takes. While a bit tricky to define, a practical definition stiffness is that if the typical Runga-Kutta solvers fail the differential equation is said to be stiff. This particular ODE does not seem to be stiff since all of the integrators (for real valued ODEs) from the SciPy ODE integration library successfully solved the equation.

These equations so far describe a current driven version of the simple implosion model. Inductance effects can be added, along with equations for voltage and current, to create a voltage-driven version. The inductance equations are:

$$L_{vac} = \frac{\mu_0 h}{2\pi} \ln\left(\frac{r_{rc}}{r}\right), \tag{A.3}$$

$$\dot{L}_{vac} = \frac{-\mu_0 h}{2\pi} \frac{v}{r}, \tag{A.4}$$

and the voltage and current equations are:

$$\dot{I} = \frac{\phi - I\dot{L}}{L_0 + L_{vac}}, \tag{A.5}$$

$$\dot{\phi} = \frac{-I - \phi/R_{loss}}{C}. \tag{A.6}$$

The inductance equations represent the change in in the system inductance as the liner implodes, with r_{rc} being the return-current radius. Note that there are further inductance equations that can be included to add more detail to the model. The voltage and current equations contain the total capacitance C of the pulsed power driver and model the parasitic (shunt) current losses through the quantity R_{loss}.

In the voltage-driven model, the motion of the liner (and its effect on the inductance) can affect the amount of current delivered to the liner. Thus, effects like "inductive dips" in the current pulse can be modeled (note that inductive dips are also observed in implosion experiments). This is convenient when modeling potential experimental loads for a pulsed power machine, since the size and timing of the inductive dip is a good measure of how well suited the load is for the pulsed power machine.

APPENDIX B

The MAIZE LTD

The Michigan Accelerator for Inductive Z-pinch Experiments (MAIZE) is a single stage, 3-meter diameter LTD, at the University of Michigan [16, 92, 93]. While we will not be driving our experiment with the MAIZE LTD we will briefly discuss it here. With minor hardware modifications, the experiments described in this dissertation could easily be run on MAIZE. Additionally, while MAIZE does not have as extensive of a diagnostic suite as COBRA does, it does still have the key diagnostics used in these experiments and discussed below in this Chapter. We originally planned to use the MAIZE facility for these experiments, and we did make an initial attempt, but the machine was in need of a switch rebuild and upgrade, which took longer than expected. Thus, while MAIZE was being upgraded, the decision was made to use COBRA instead. Recently, however, the MAIZE upgrade was completed, and science campaigns have resumed. Thus, future DSP experiments on MAIZE are very much a possibility.

MAIZE is capable of delivering a 1-MA current peak, with a 100-ns rise time into a matched load, at a full charge of $\pm$100 kV. Typically, the charge voltage is limited to $\pm$70 kV in order to reduce the voltage reversal on the capacitors, which results in peak currents of roughly 700 kA. A cross sectional view of the LTD is show in Fig. B.1. The building block of the LTD is the "brick", which is made of a capacitor-switch-capacitor series connection, and can be seen on the outer edge of Fig. B.1. MAIZE is made of 40 of bricks. The outputs of the 40 bricks are all connected together electrically in parallel. They reside along an outer ring that surrounds the central vacuum chamber and load region. The energy stored in the bricks is delivered via transmission lines—i.e., the electrical power first passes through the outer coaxial transmission line, then through the radial transmission line, and finally into a conical transmission line that connects to the experimental load hardware and target. Within the LTD, there exists an alternative, parasitic current path in parallel with the desired path to the load. This parasitic path is along the inner surface of the outer case (the dark blue surrounding the bricks in Fig. B.1). The ferromagnetic cores make this path a high-impedance path, thus forcing the bulk of the current to the load as desired. MAIZE is capable of driving

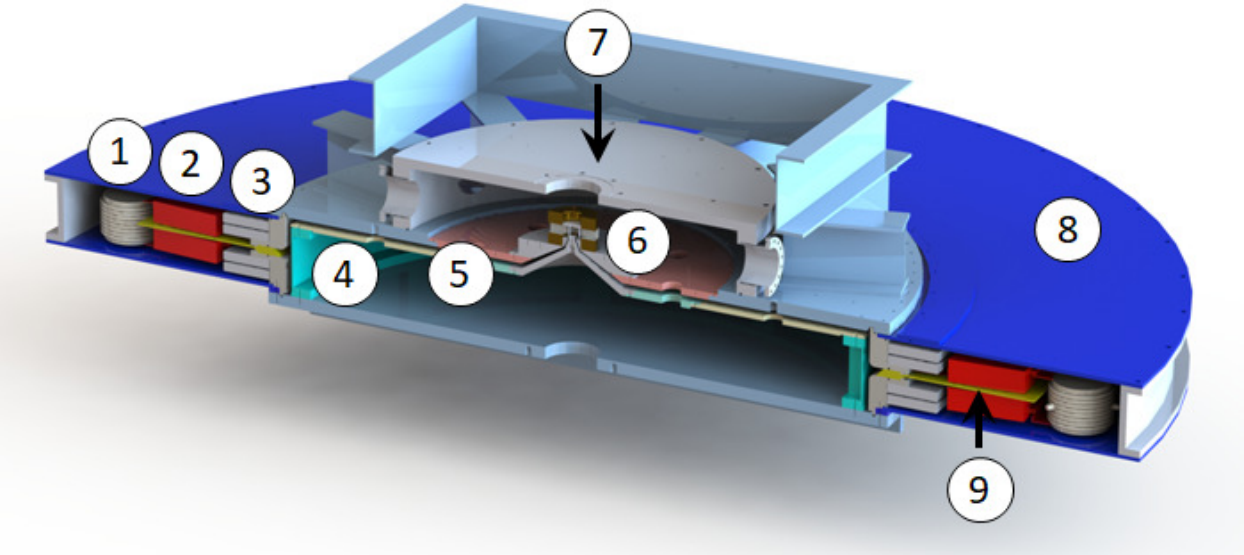

Figure B.1: A cutaway of a 3D CAD model of MAIZE. (1) Spark-gap switch (40 such switches), (2) 40 nF capacitors (80 such capacitors), (3) iron cores (one upper core and one lower core), (4) outer coaxial transmission line section, (5) radial transmission line section, (6) load region, (7) vacuum chamber, (8) oil chamber, (9) high voltage insulator.

loads of 10–20 nH but the rise times are longer (200 ns) and peak currents are smaller (around 700 kA). This is because COBRA is a much stiffer driver than MAZIE, having roughly 5 times the driver impedance.

From Chapter 1 we know that simple LC circuit models can be used to describe the pulses from pulsed-power generators, but we can now add more detail to the picture. Pulsed-power machines, and experimental hardware, have resistances that need to be accounted for; experiments are dynamic and have time-varying inductances. A more complete circuit of an LTD will look something like Fig B.2. In this circuit, we break things into the machine side and the load or experiment side. This is a convenient way of modeling things since the driver parameters are set by the machine one happens to be using; the only knob to turn on this side is the capacitor charge voltage. It's worth noting that in reality, pulsed power machines have many switches, and getting them to trigger synchronously strongly impacts the shape and amplitude of the voltage pulse that is delivered. This can be modeled, but it does not make for an easy-to-read circuit diagram (for example, a single stage LTD can consist of 40 switches), so we'll be living in an ideal world with only one switch to close. We've already made use of this circuit model to estimate thin-shell trajectories in Section 2 and made use of it when analyzing our experimental data. For full details on how this circuit model produces liner trajectory plots, see Appendix A.

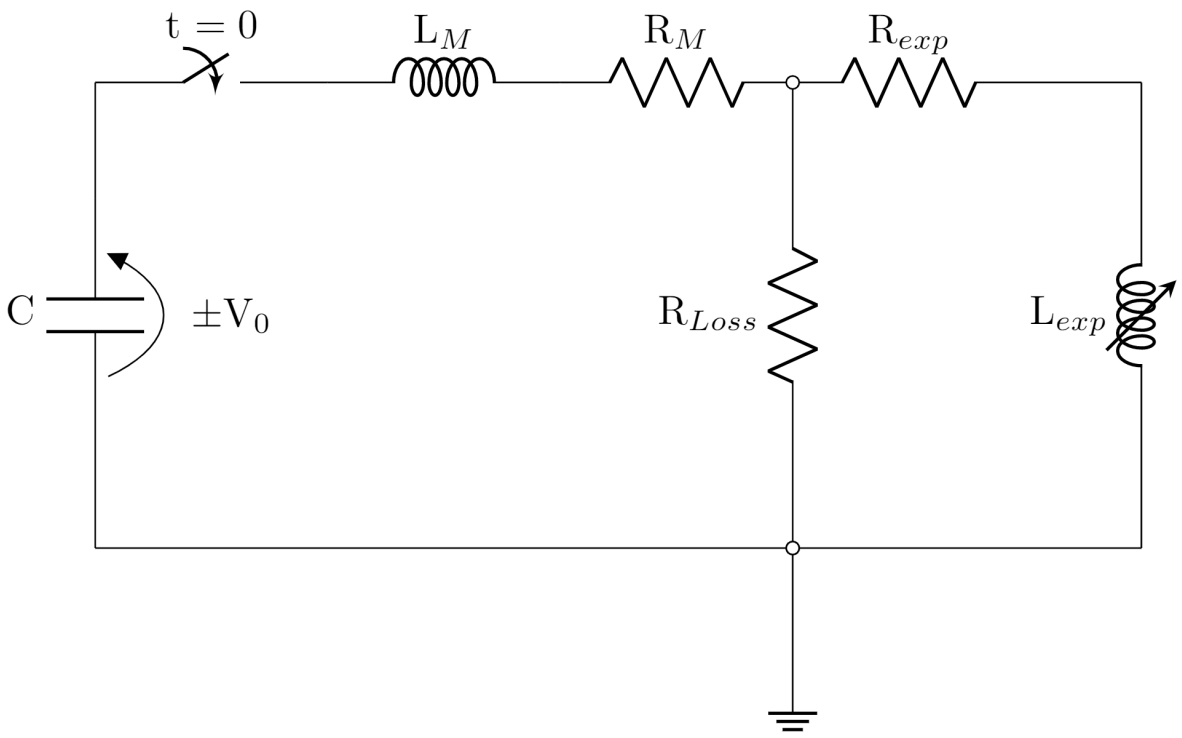

Figure B.2: An LRC circuit representation of a pulsed-power generator. The driver will have some capacitance C, charged to some initial voltage V_0. At time $t = 0$ the machine fires, indicated in the circuit diagram by the closing switch. L_M and R_M represent the driver side inductance and resistance, while L_{exp} and R_{exp} represent the load or experiment side (time varying) inductance and resistance. The R_{loss} in parallel with the load inductance is a way to model shunt current loss in the system [i.e. core losses in an LTD [8], or power flow losses within a magnetically insulated transmission line (MITL)].

APPENDIX C

Self-Emission Images From the 12-Frame, Visible-Light Camera

Here, image sequences (raw, not contrast enhanced) from the fast framing camera are presented. Using these images the plasma/vacuum boundary is tracked. Unfortunately the usual computer vision edge detections methods such as the Canny edge detector fail on these images, even when techniques such as Gaussian blurs are applied to the images. Such a method has reasonable success with the SZP images however the method struggles with the DSP shots due to the return current posts obscuring the liner or being another source of light in the image.

The method used to track the plasma boundary used in this dissertation instead relies on user input. A person clicks on the image where they think the peaks or valleys are. The program then takes a lineout locally near the points selected and looks for the maximum of the slope. The points are then averaged together to get the average liner radius. While this method may sound arbitrary and subjective to where a particular person thinks the boundary is, it is no more arbitrary then that same person coding in a set of conditions to find that boundary. A sample image is presented in Fig. C.1.

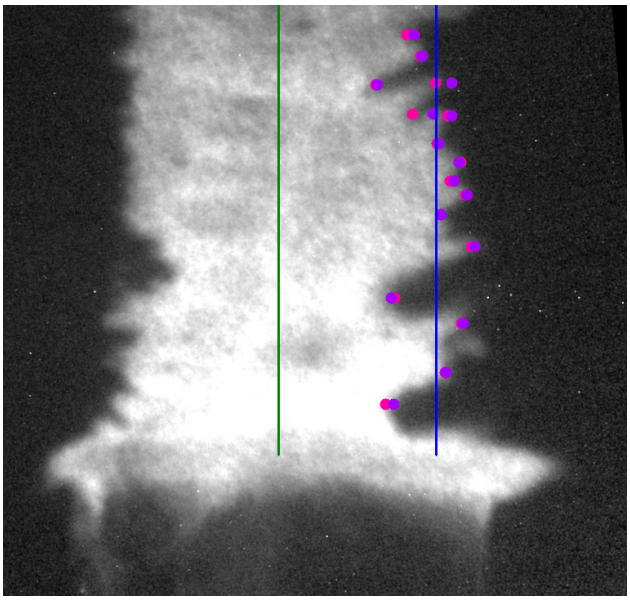

Figure C.1: An example image of how the average liner radius is calculated. The purple dots are the user inputs while the pink dots are the corrections the program makes. The green line represents the center of the liner, or $R = 0$, while the blue line represents the average of the instability spikes and bubbles (the average of the pink dots).

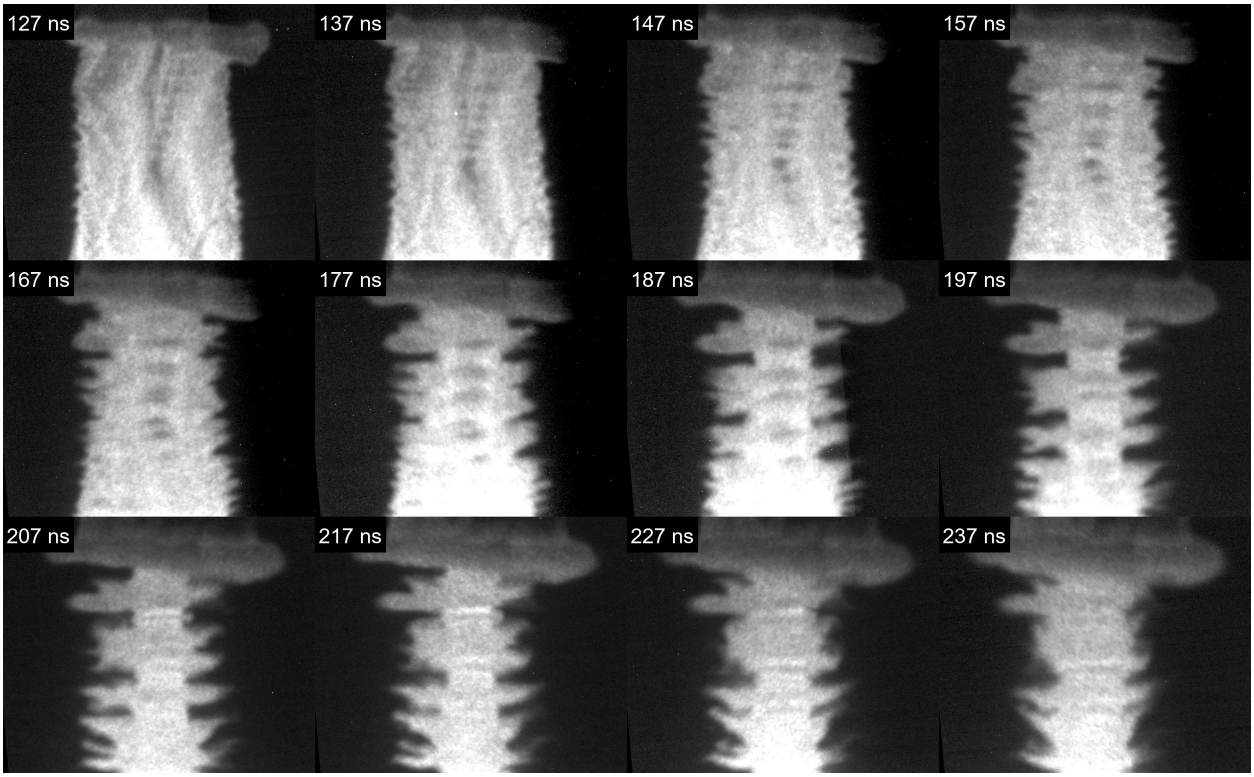

Figure C.2: Framing camera images from shot 5391, an SZP shot.

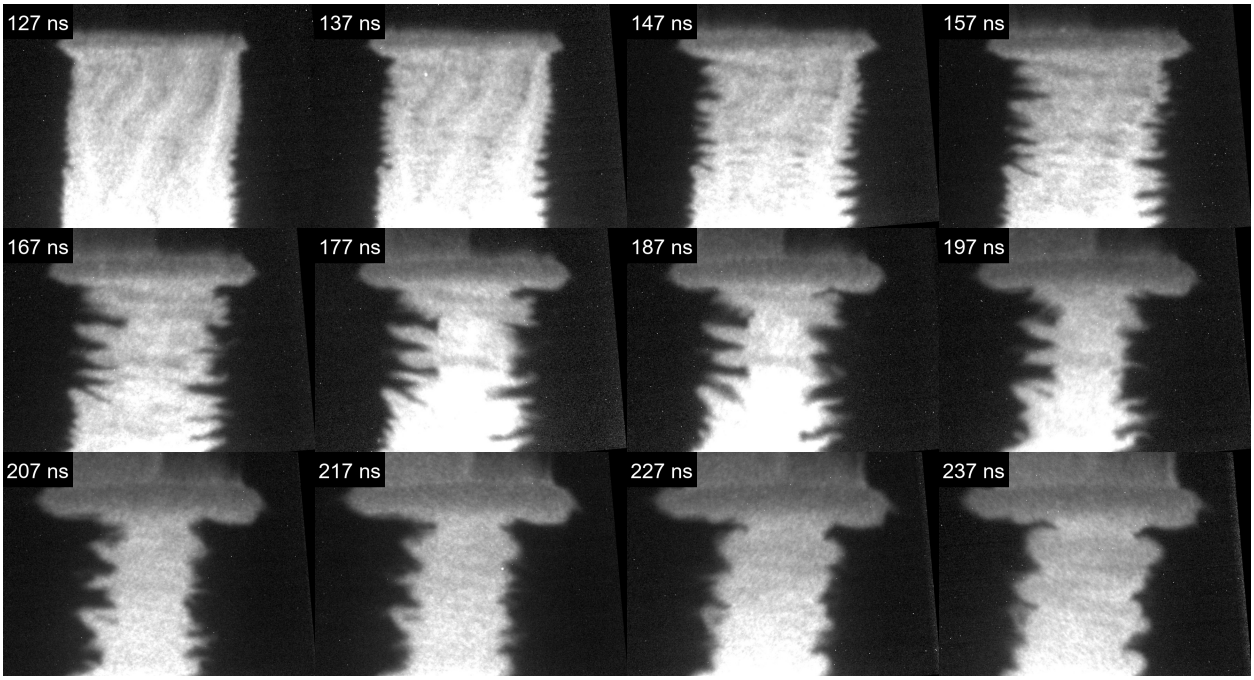

Figure C.3: Framing camera images from shot 5394, an SZP shot.

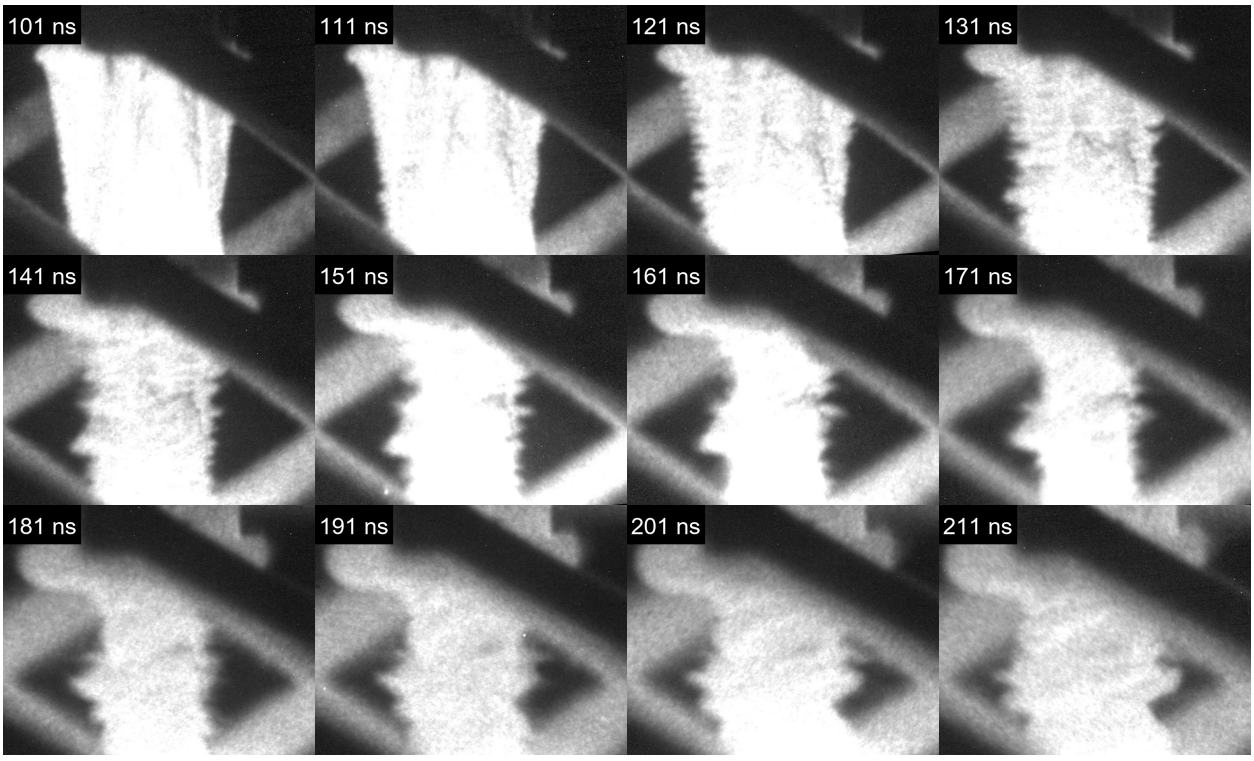

Figure C.4: Framing camera images from shot 5396, a 14-T DSP shot.

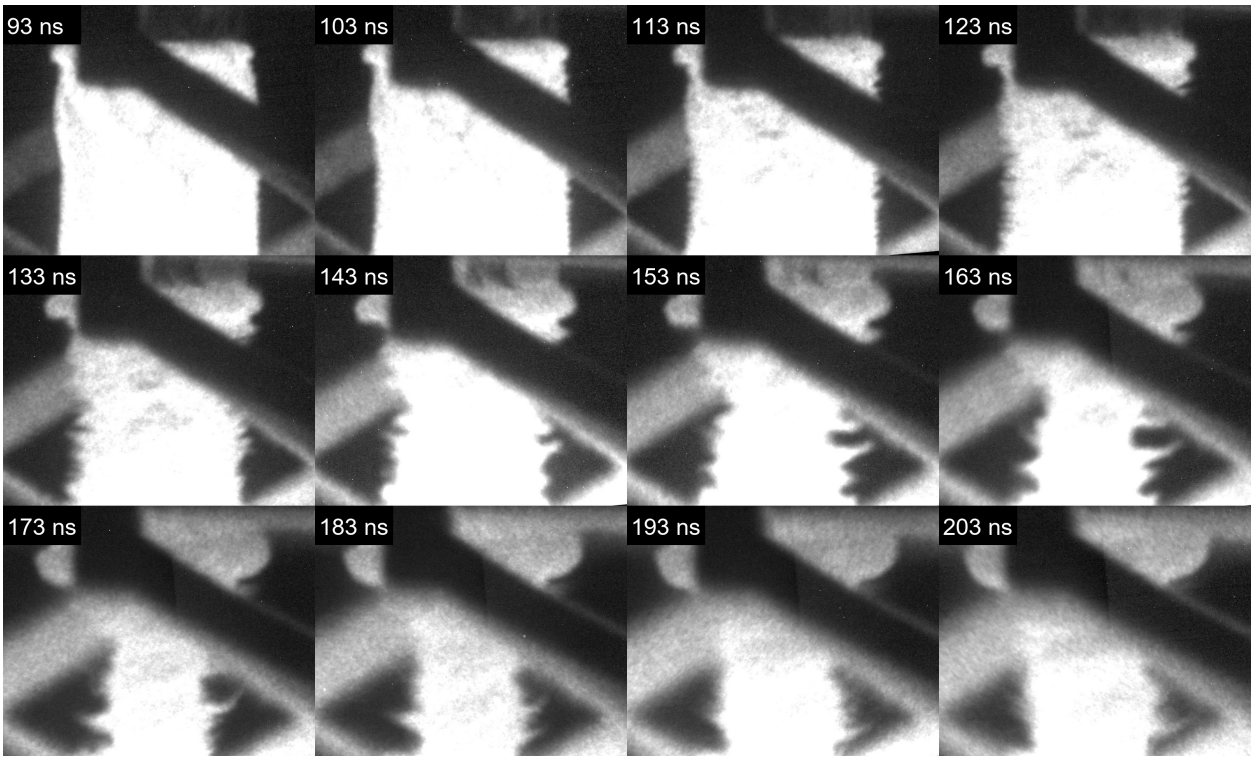

Figure C.5: Framing camera images from shot 5397, a 14-T DSP shot.

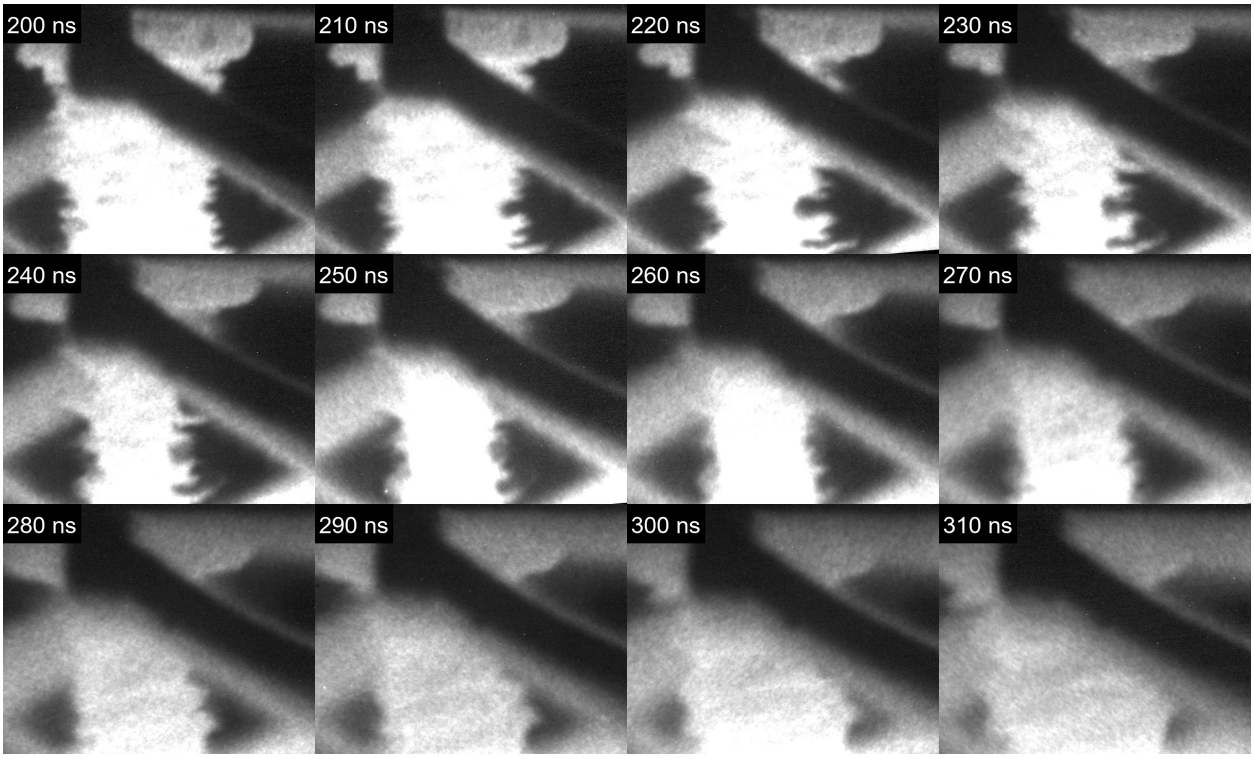

Figure C.6: Framing camera images from shot 5399, a 14-T DSP shot.

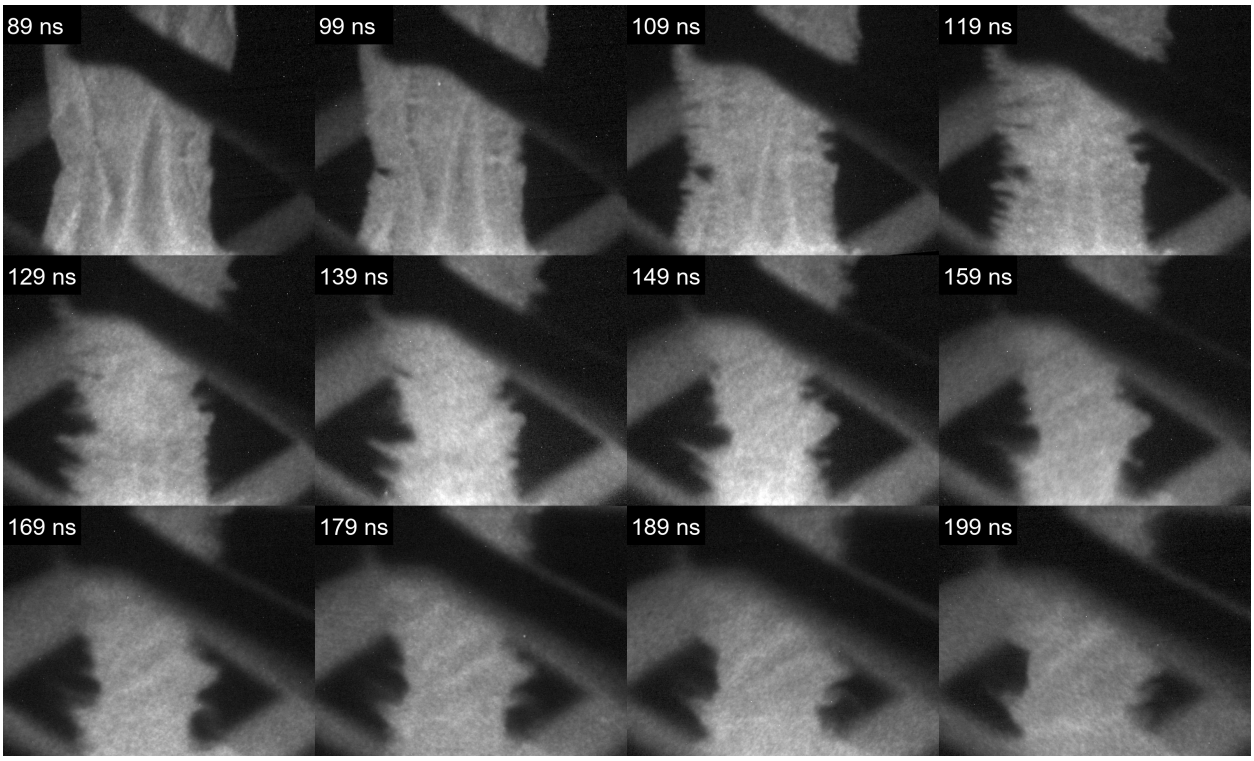

Figure C.7: Framing camera images from shot 5402, a 14-T DSP shot.

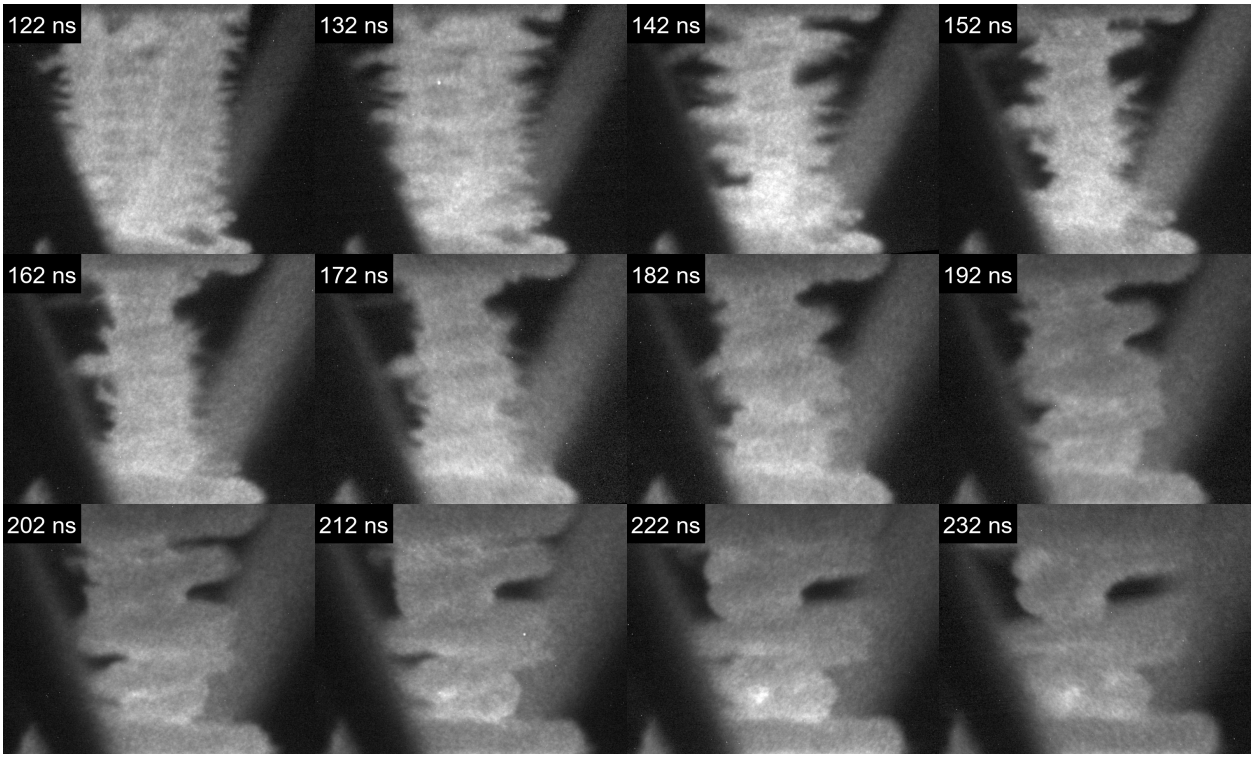

Figure C.8: Framing camera images from shot 5403, a 2-T DSP shot.

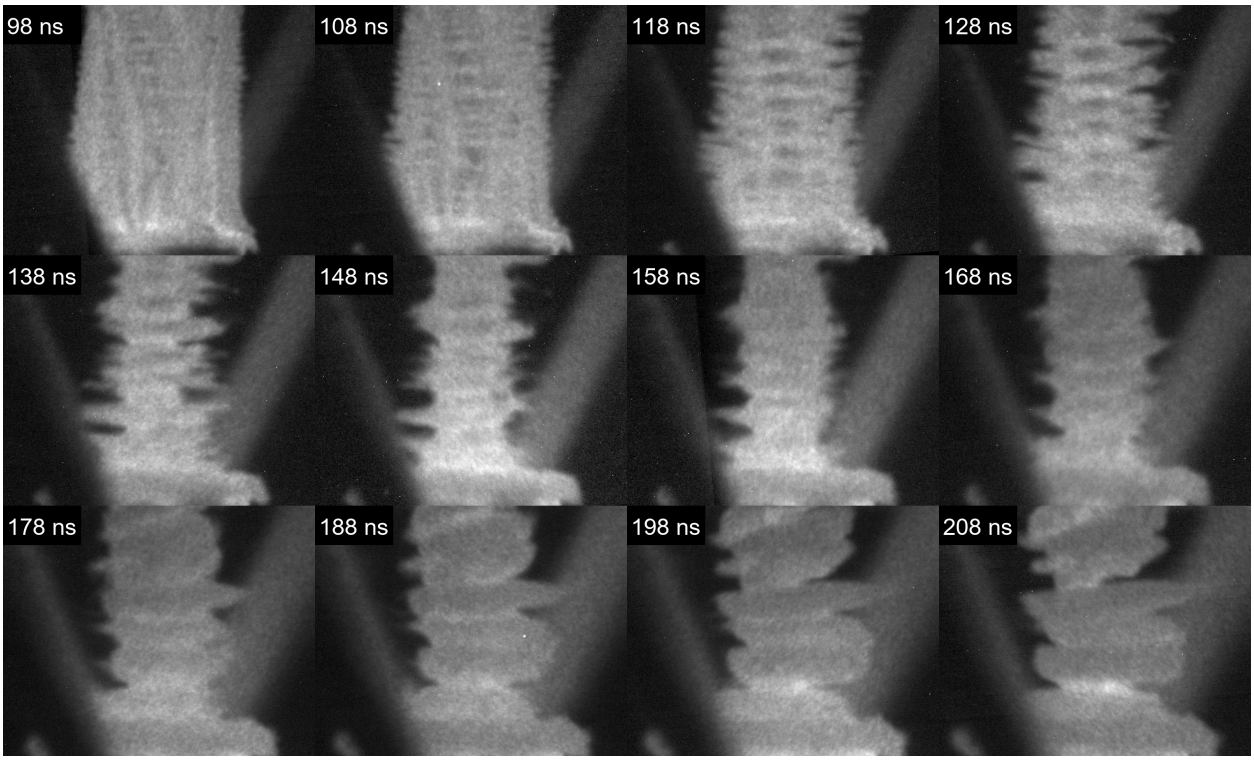

Figure C.9: Framing camera images from shot 5404, a 2-T DSP shot.

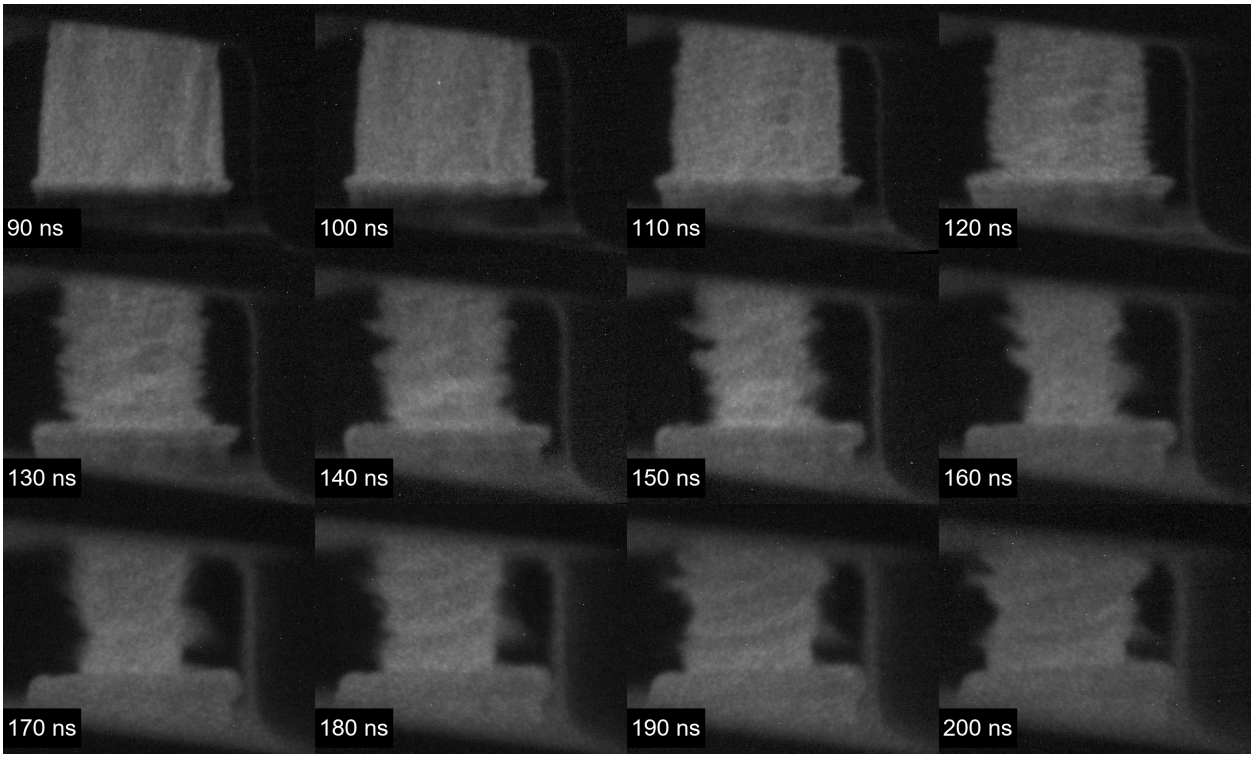

Figure C.10: Framing camera images from shot 5407, a 20-T DSP shot.

APPENDIX D

Self-Emission Images From the XUV Cameras

Here, image sequences (raw, not contrast enhanced) from both of the XUV cameras are presented. Images sequences on the left (or right) are always from the same XUV camera, hence the slightly different shade of green in each set of images.

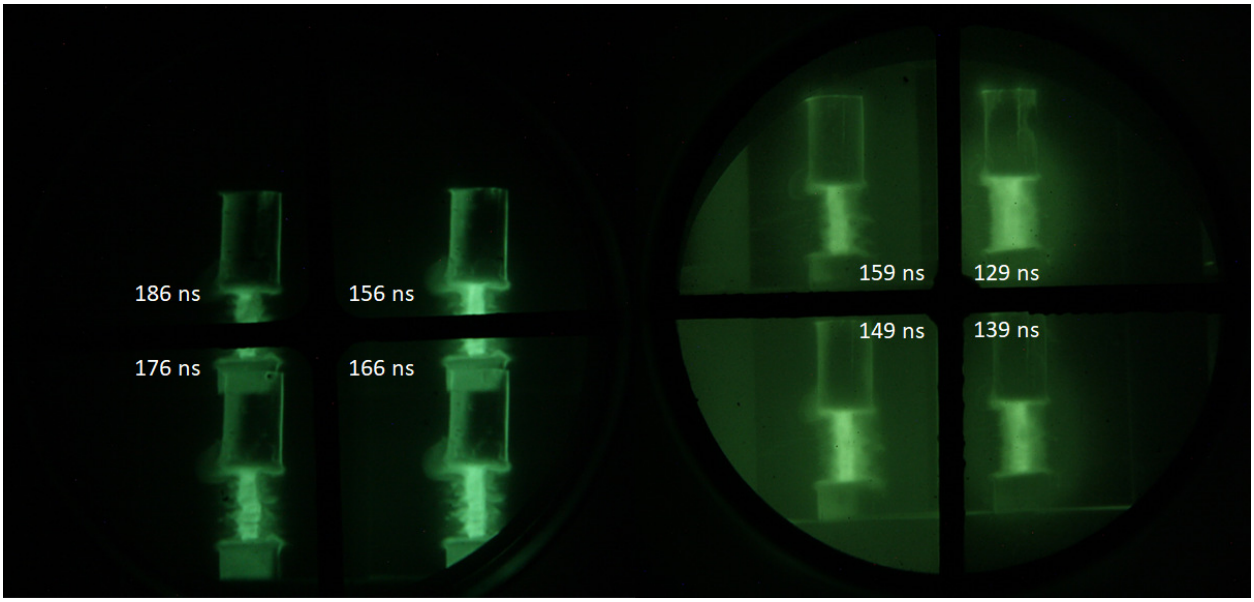

Figure D.1: XUV images from shot 5185, an SZP shot.

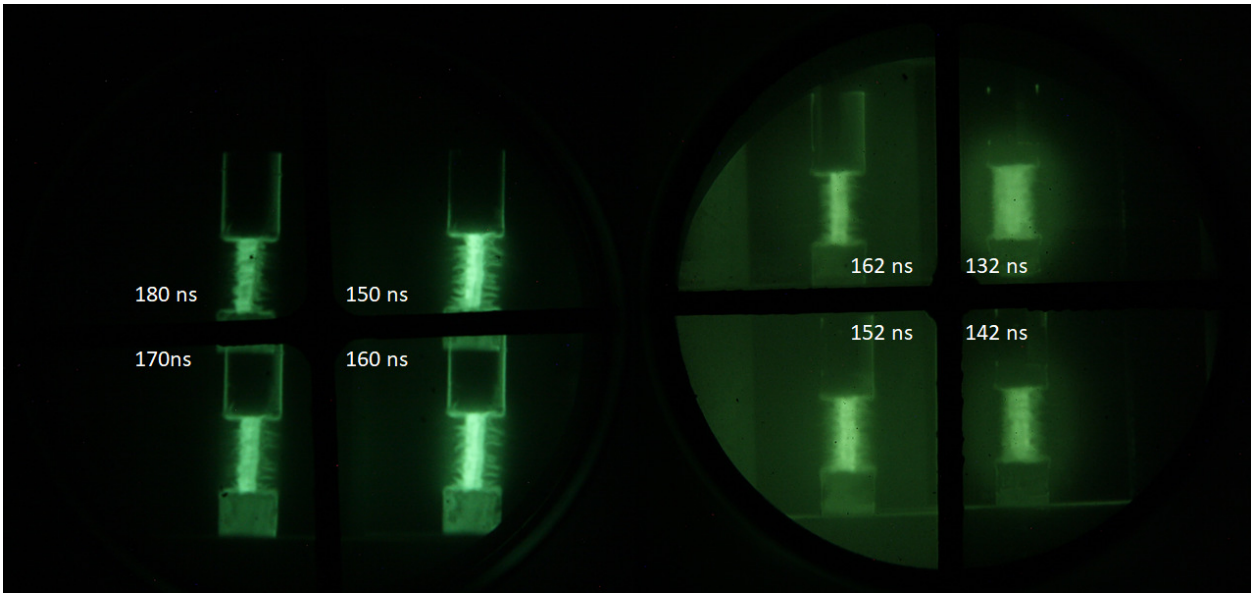

Figure D.2: XUV images from shot 5186, an SZP shot.

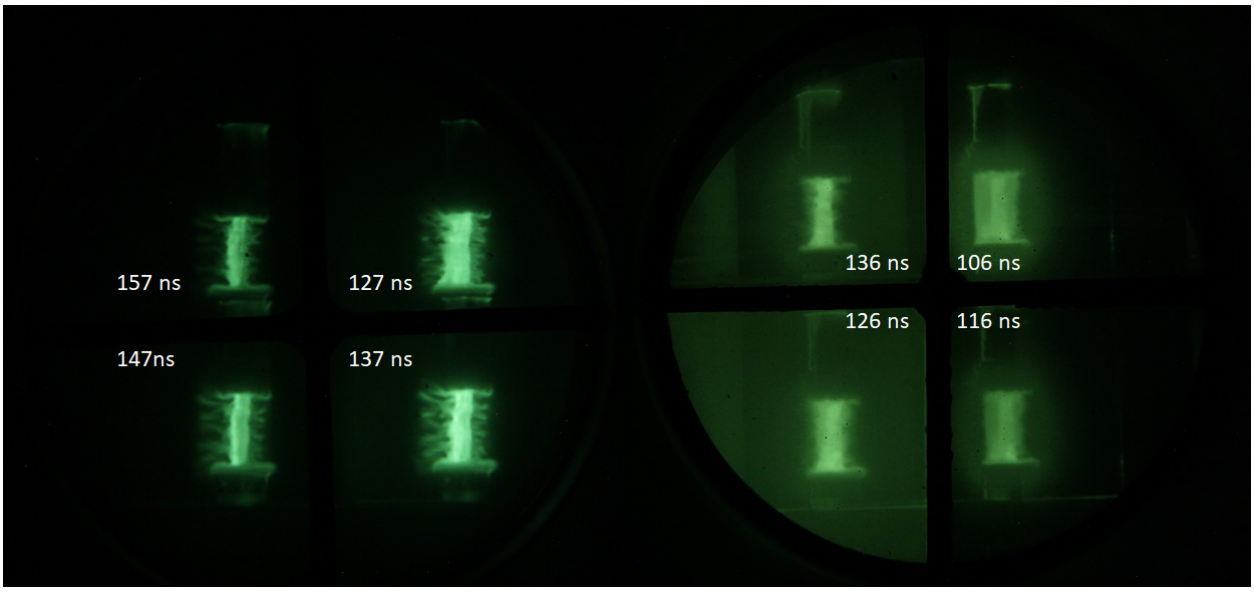

Figure D.3: XUV images from shot 5188, an SZP shot.

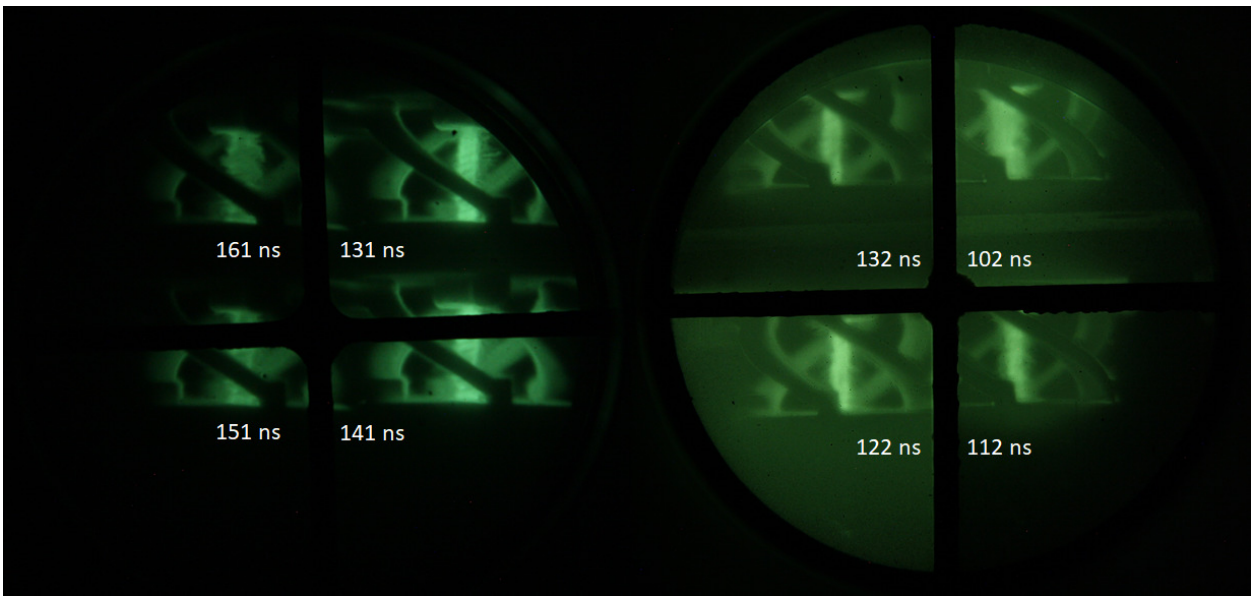

Figure D.4: XUV images from shot 5189, a mid-field DSP shot.

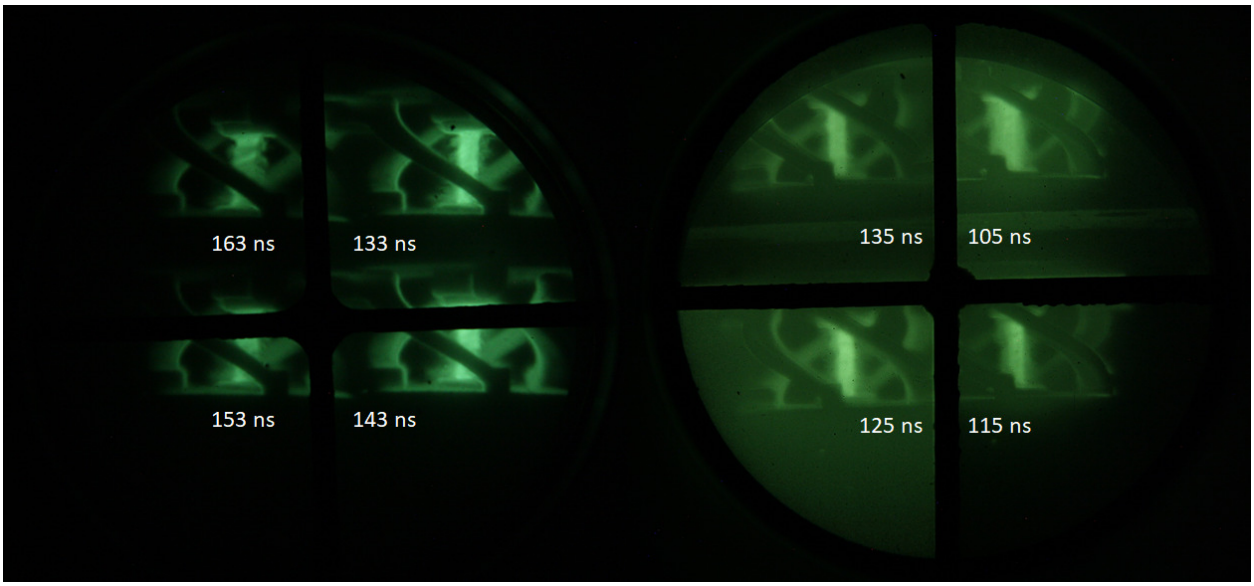

Figure D.5: XUV images from shot 5190, a mid-field DSP shot.

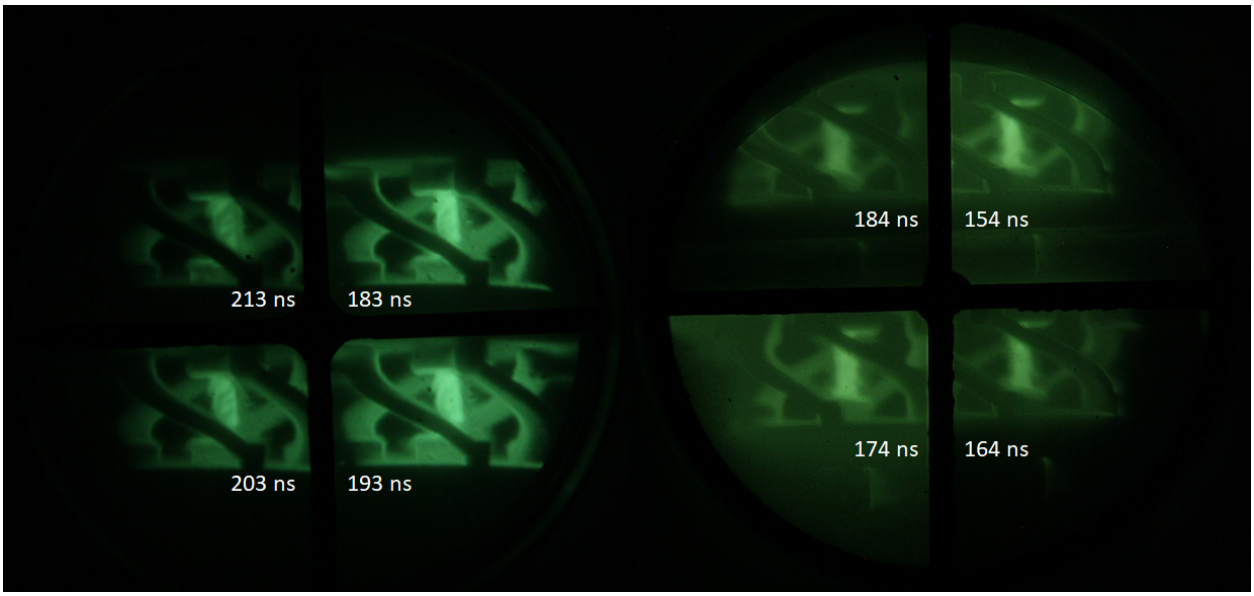

Figure D.6: XUV images from shot 5192, a mid-field DSP shot.

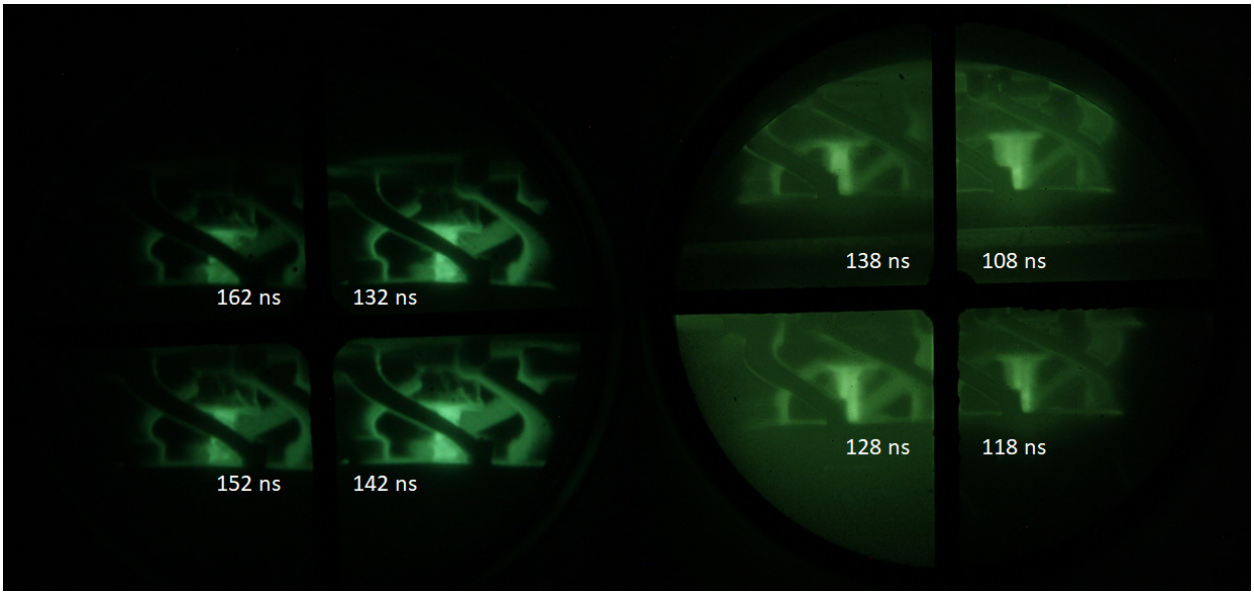

Figure D.7: XUV images from shot 5193, a mid-field DSP shot.

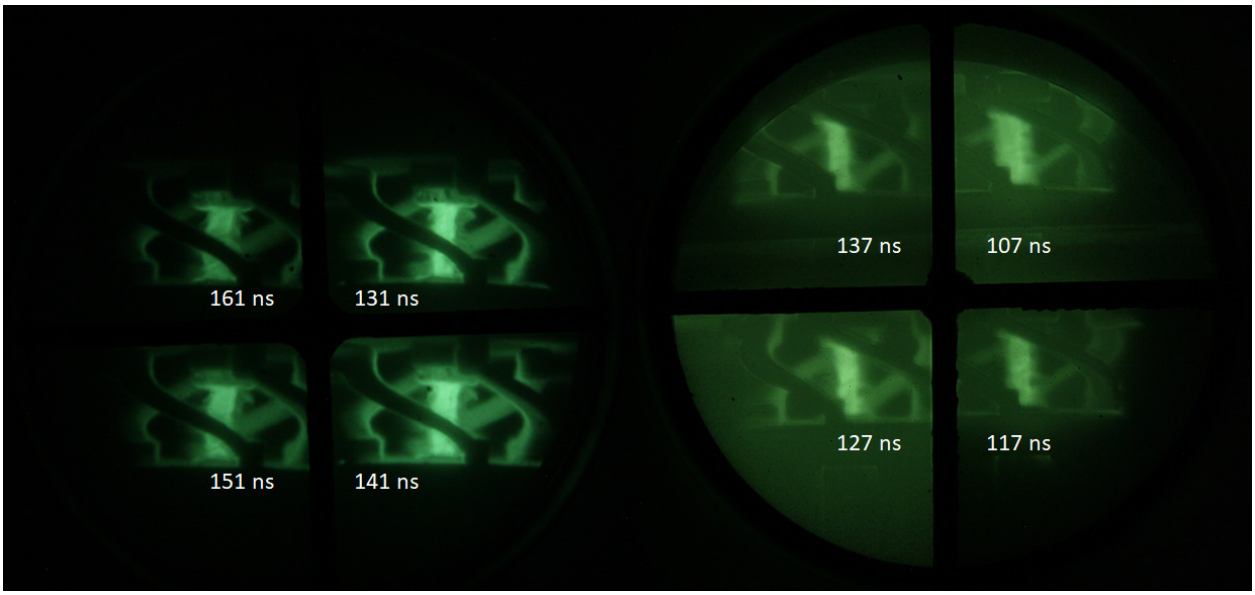

Figure D.8: XUV images from shot 5194, a mid-field DSP shot.

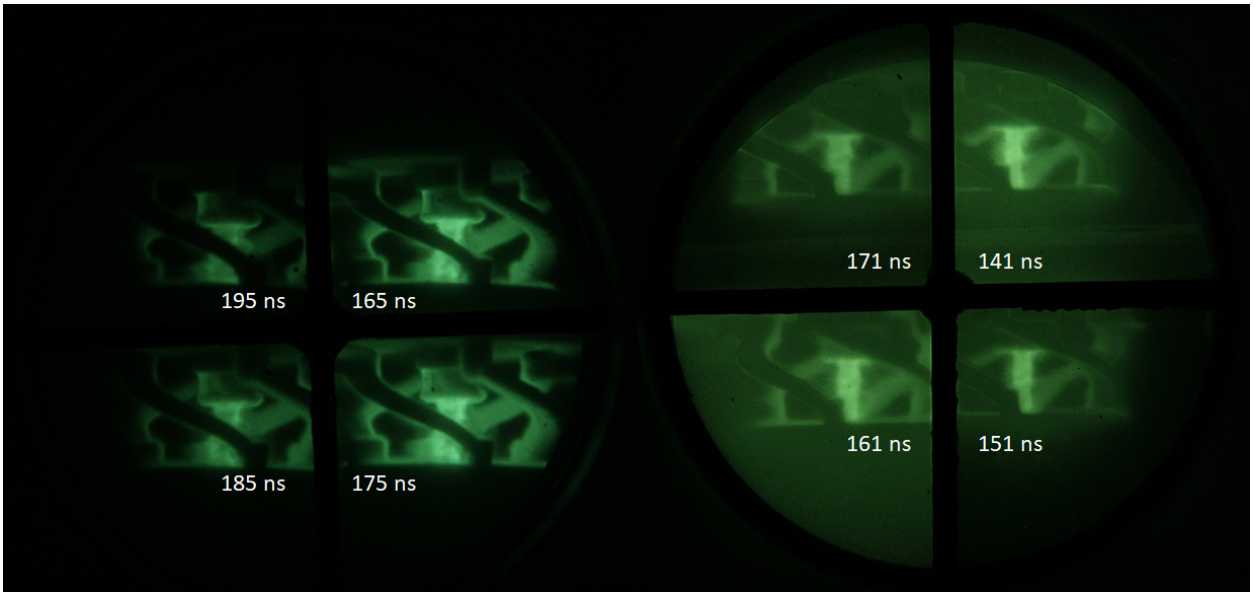

Figure D.9: XUV images from shot 5195, a mid-field DSP shot.

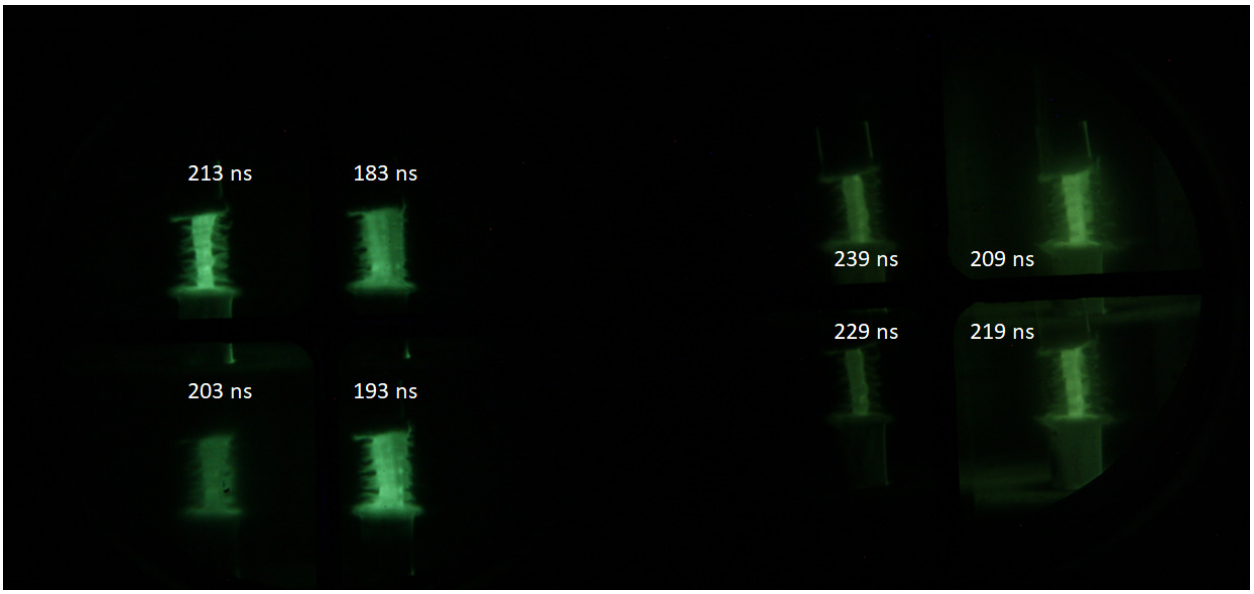

Figure D.10: XUV images from shot 5391, an SZP shot.

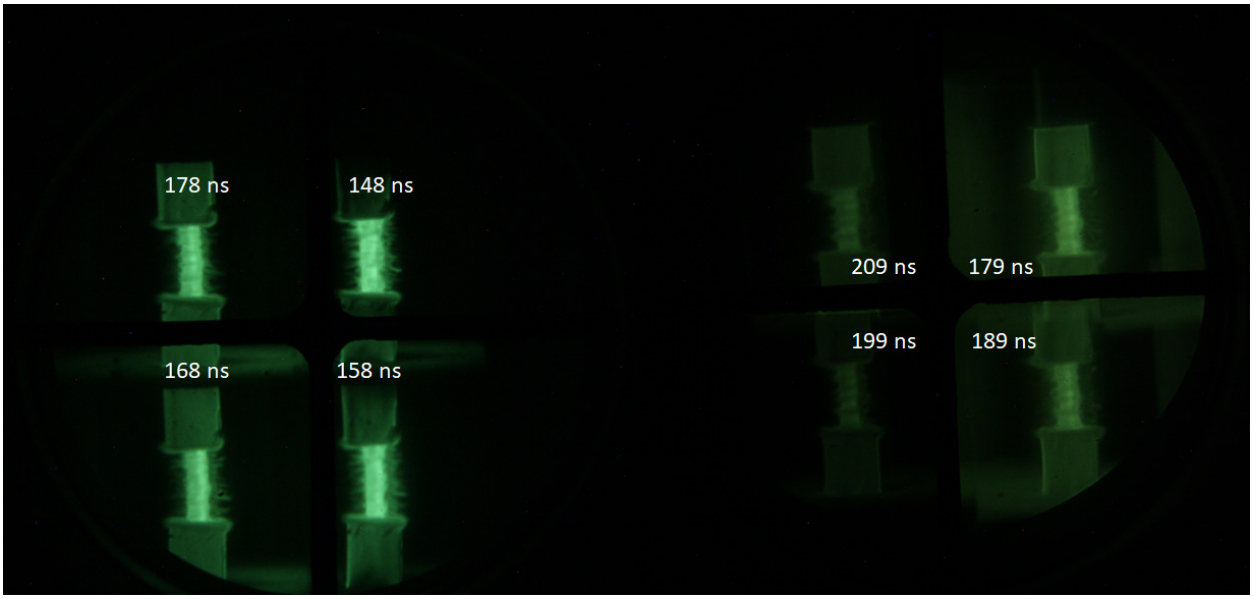

Figure D.11: XUV images from shot 5392, an SZP shot.

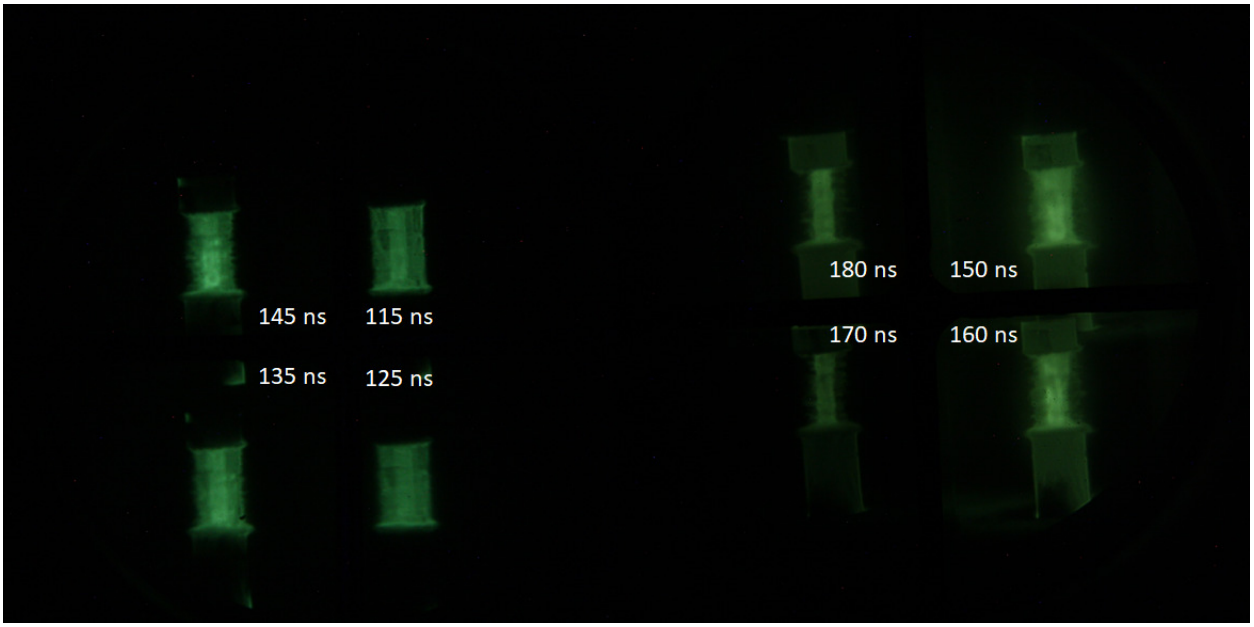

Figure D.12: XUV images from shot 5394, an SZP shot.

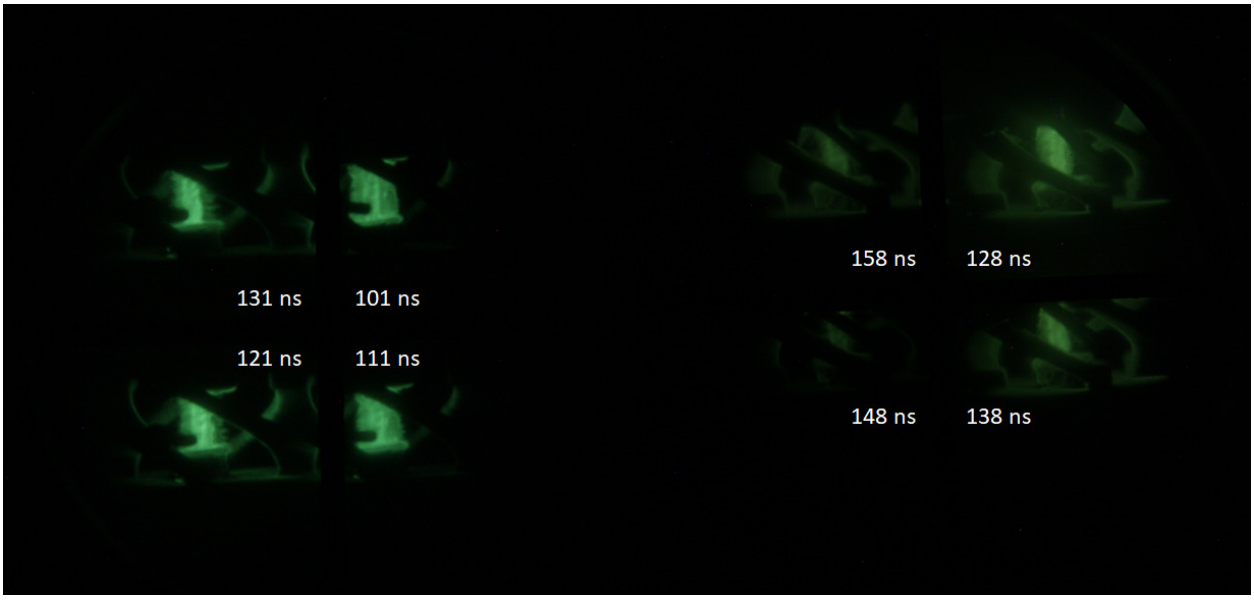

Figure D.13: XUV images from shot 5396, a mid-field DSP shot.

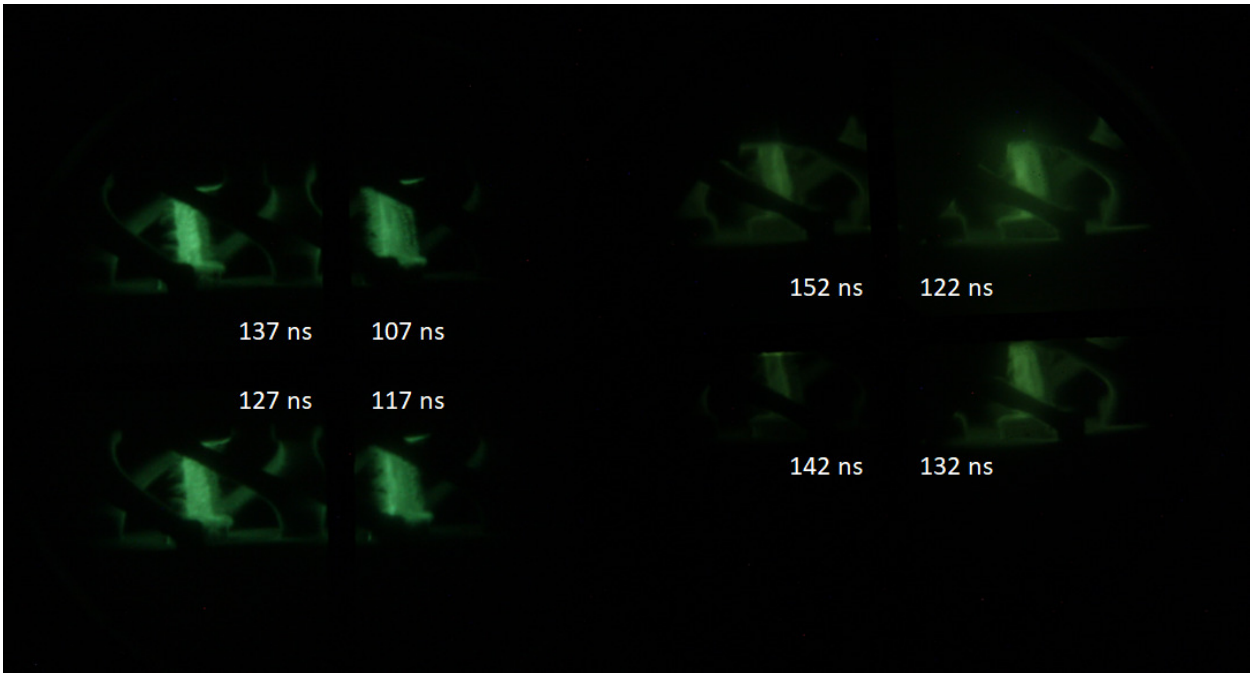

Figure D.14: XUV images from shot 5397, a mid-field DSP shot.

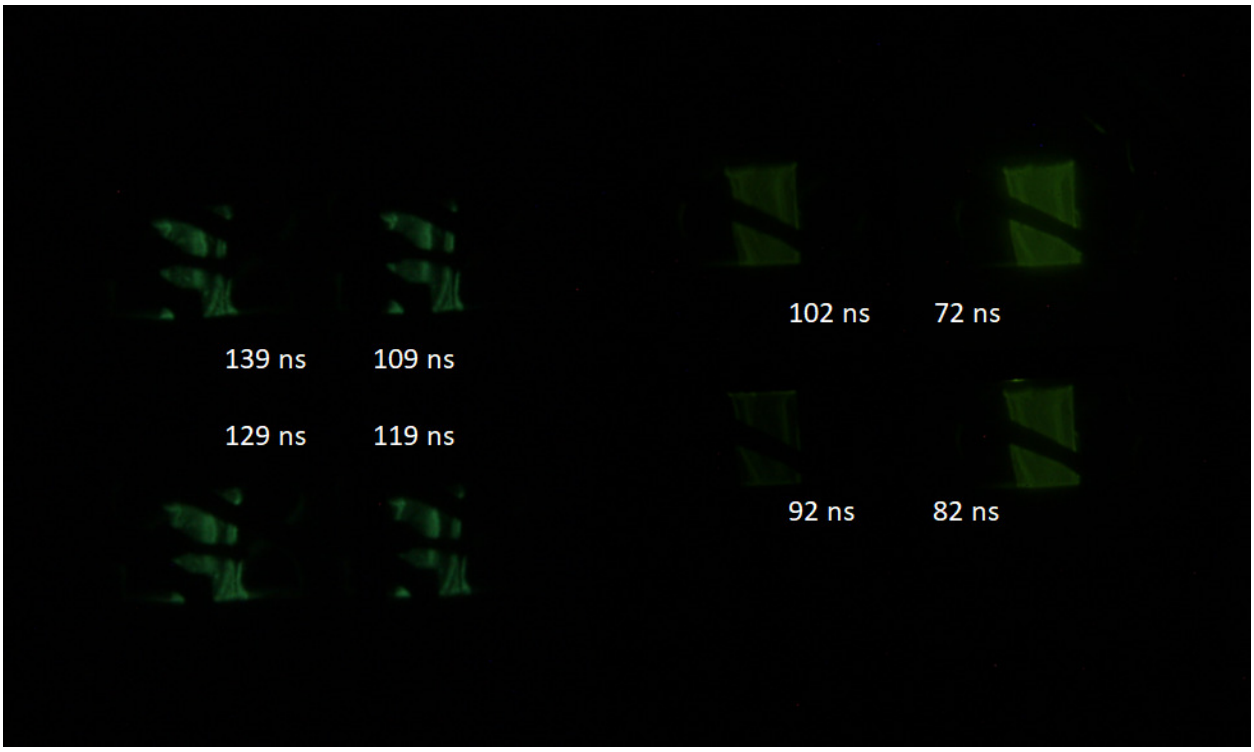

Figure D.15: XUV images from shot 5398, a mid-field DSP shot.

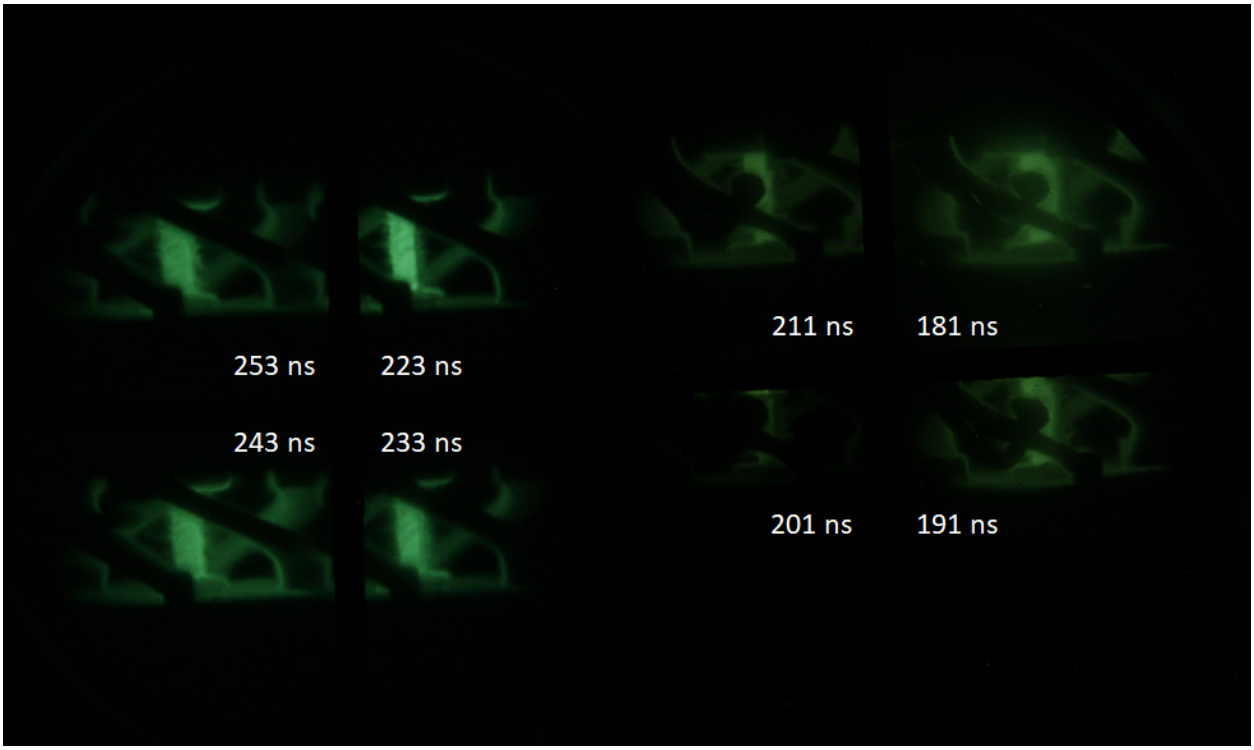

Figure D.16: XUV images from shot 5399, a mid-field DSP shot.

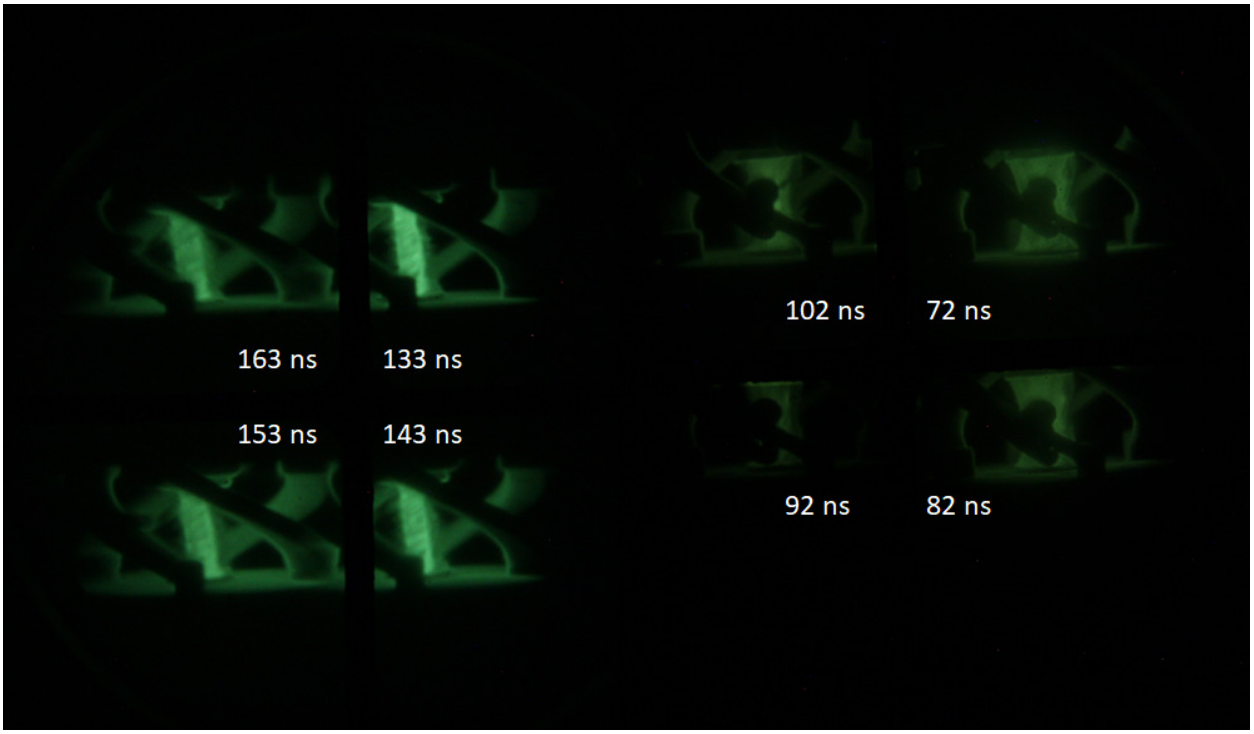

Figure D.17: XUV images from shot 5402, a mid-field DSP shot.

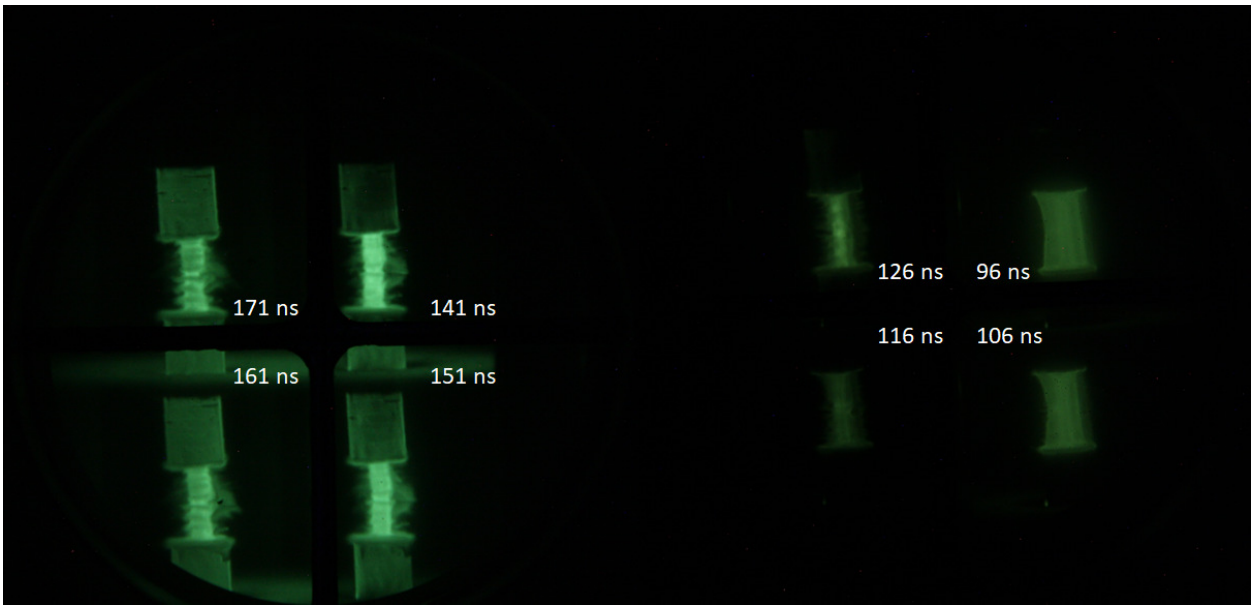

Figure D.18: XUV images from shot 5405, a premagnetized SZP shot.

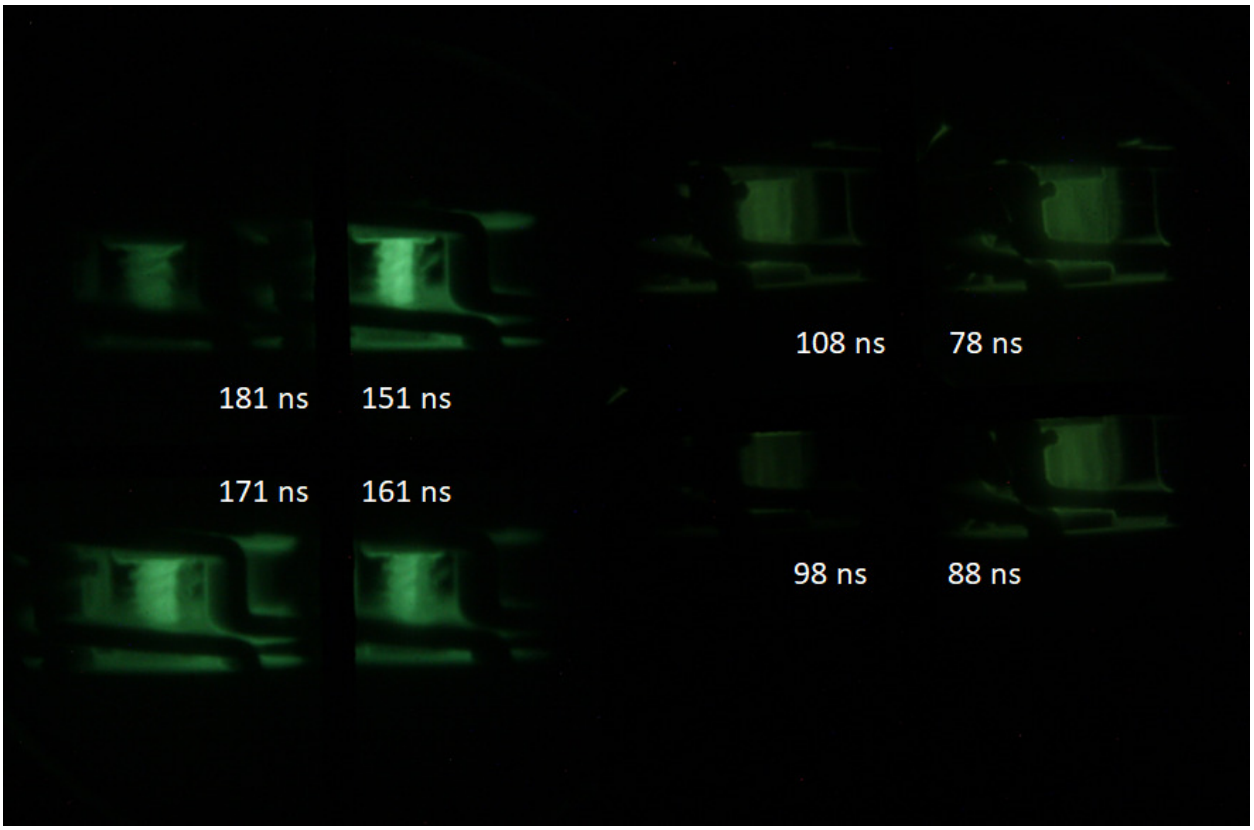

Figure D.19: XUV images from shot 5407, a high-field DSP shot.

BIBLIOGRAPHY

[1] M. R. Gomez, S. A. Slutz, A. B. Sefkow, K. D. Hahn, S. B. Hansen, P. F. Knapp, P. F. Schmit, C. L. Ruiz, D. B. Sinars, E. C. Harding, C. A. Jennings, T. J. Awe, M. Geissel, D. C. Rovang, I. C. Smith, G. A. Chandler, G. W. Cooper, M. E. Cuneo, A. J. Harvey-Thompson, M. C. Herrmann, M. H. Hess, D. C. Lamppa, M. R. Martin, R. D. McBride, K. J. Peterson, J. L. Porter, G. A. Rochau, M. E. Savage, D. G. Schroen, W. A. Stygar, and R. A. Vesey, "Demonstration of thermonuclear conditions in magnetized liner inertial fusion experiments," *Physics of Plasmas*, vol. 22, no. 5, p. 056306, 2015.

[2] M. S. Davies Wykes and S. B. Dalziel, "Efficient mixing in stratified flows: experimental study of a Rayleigh–Taylor unstable interface within an otherwise stable stratification," *Journal of Fluid Mechanics*, vol. 756, p. 1027–1057, 2014.

[3] R. D. McBride and S. A. Slutz, "A semi-analytic model of magnetized liner inertial fusion," *Physics of Plasmas*, vol. 22, no. 5, p. 052708, 2015.

[4] J. B. Greenly, J. D. Douglas, D. A. Hammer, B. R. Kusse, S. C. Glidden, and H. D. Sanders, "A 1ma, variable risetime pulse generator for high energy density plasma research," *Review of Scientific Instruments*, vol. 79, no. 7, p. 073501, 2008.

[5] P. C. Campbell, J. M. Woolstrum, F. Antoulinakis, T. M. Jones, D. A. Yager-Elorriaga, S. M. Miller, N. M. Jordan, Y. Y. Lau, R. M. Gilgenbach, and R. D. Mcbride, "Diagnostic and power feed upgrades to the MAIZE facility," *IEEE Transactions on Plasma Science*, vol. 46, pp. 3973–3981, Nov 2018.

[6] D. A. Yager-Elorriaga, P. Zhang, A. M. Steiner, N. M. Jordan, Y. Y. Lau, and R. M. Gilgenbach, "Seeded and unseeded helical modes in magnetized, non-imploding cylindrical liner-plasmas," *Phys. Plasmas*, vol. 23, no. 10, p. 101205, 2016.

[7] A. L. Velikovich and P. F. Schmit, "Bell-Plesset effects in Rayleigh-Taylor instability of finite-thickness spherical and cylindrical shells," *Physics of Plasmas*, vol. 22, no. 12, p. 122711, 2015.

[8] J. D. Douglass, B. T. Hutsel, J. J. Leckbee, T. D. Mulville, B. S. Stoltzfus, M. L. Wisher, M. E. Savage, W. A. Stygar, E. W. Breden, J. D. Calhoun, M. E. Cuneo, D. J. De Smet, R. J. Focia, R. J. Hohlfelder, D. M. Jaramillo, O. M. Johns, M. C. Jones, A. C. Lombrozo, D. J. Lucero, J. K. Moore, J. L. Porter, S. D. Radovich, S. A. Romero, M. E. Sceiford, M. A. Sullivan, C. A. Walker, J. R. Woodworth, N. T. Yazzie, M. D. Abdalla, M. C.

Skipper, and C. Wagner, "100 GW linear transformer driver cavity: Design, simulations, and performance," *Phys. Rev. Accel. Beams*, vol. 21, p. 120401, Dec 2018.

[9] E. Marx, "Versuche über die prüfung von isolatoren mit spanningsstößen [experiments on the testing of insulators using high voltage pulses]," *Elektrotechnische Zeitschrift (in German)*, vol. 45, pp. 652–654, 1924.

[10] M. E. Savage, K. R. LeChien, M. R. Lopez, B. S. Stoltzfus, W. A. Stygar, D. S. Artery, J. A. Lott, and P. A. Corcoran, "Status of the Z pulsed power driver," in *2011 IEEE Pulsed Power Conference*, pp. 983–990, 2011.

[11] D. V. Rose, D. R. Welch, E. A. Madrid, C. L. Miller, R. E. Clark, W. A. Stygar, M. E. Savage, G. A. Rochau, J. E. Bailey, T. J. Nash, M. E. Sceiford, K. W. Struve, P. A. Corcoran, and B. A. Whitney, "Three-dimensional electromagnetic model of the pulsed-power z-pinch accelerator," *Phys. Rev. ST Accel. Beams*, vol. 13, p. 010402, Jan 2010.

[12] D. B. Sinars, M. A. Sweeney, C. S. Alexander, D. J. Ampleford, T. Ao, J. P. Apruzese, C. Aragon, D. J. Armstrong, K. N. Austin, T. J. Awe, A. D. Baczewski, J. E. Bailey, K. L. Baker, C. R. Ball, H. T. Barclay, S. Beatty, K. Beckwith, K. S. Bell, J. F. Benage, N. L. Bennett, K. Blaha, D. E. Bliss, J. J. Boerner, C. J. Bourdon, B. A. Branch, J. L. Brown, E. M. Campbell, R. B. Campbell, D. G. Chacon, G. A. Chandler, K. Chandler, P. J. Christenson, M. D. Christison, E. B. Christner, R. C. Clay, K. R. Cochrane, A. P. Colombo, B. M. Cook, C. A. Coverdale, M. E. Cuneo, J. S. Custer, A. Dasgupta, J.-P. Davis, M. P. Desjarlais, D. H. Dolan, J. D. Douglass, G. S. Dunham, S. Duwal, A. D. Edens, M. J. Edwards, E. G. Evstatiev, B. G. Farfan, J. R. Fein, E. S. Field, J. A. Fisher, T. M. Flanagan, D. G. Flicker, M. D. Furnish, B. R. Galloway, P. D. Gard, T. A. Gardiner, M. Geissel, J. L. Giuliani, M. E. Glinsky, M. R. Gomez, T. Gomez, G. P. Grim, K. D. Hahn, T. A. Haill, N. D. Hamlin, J. H. Hammer, S, "Review of pulsed power-driven high energy density physics research on z at sandia," *Physics of Plasmas*, vol. 27, no. 7, p. 070501, 2020.

[13] R. D. McBride, W. A. Stygar, M. E. Cuneo, D. B. Sinars, M. G. Mazarakis, J. J. Leckbee, M. E. Savage, B. T. Hutsel, J. D. Douglass, M. L. Kiefer, B. V. Oliver, G. R. Laity, M. R. Gomez, D. A. Yager-Elorriaga, S. G. Patel, B. M. Kovalchuk, A. A. Kim, P. . Gourdain, S. N. Bland, S. Portillo, S. C. Bott-Suzuki, F. N. Beg, Y. Maron, R. B. Spielman, D. V. Rose, D. R. Welch, J. C. Zier, J. W. Schumer, J. B. Greenly, A. M. Covington, A. M. Steiner, P. C. Campbell, S. M. Miller, J. M. Woolstrum, N. B. Ramey, A. P. Shah, B. J. Sporer, N. M. Jordan, Y. Y. Lau, and R. M. Gilgenbach, "A primer on pulsed power and linear transformer drivers for high energy density physics applications," *IEEE Transactions on Plasma Science*, vol. 46, no. 11, pp. 3928–3967, 2018.

[14] B. M. Koval'chuk, V. A. Vizir', A. A. Kim, E. V. Kumpyak, S. V. Loginov, A. N. Bastrikov, V. V. Chervyakov, N. V. Tsoi, P. Monjaux, and D. Kh'yui, "Fast primary storage device utilizing a linear pulse transformer," *Russian Physics Journal*, vol. 40, pp. 1142–1153, Dec 1997.

[15] A. A. Kim, B. M. Kovalchuk, E. V. Kumpjak, and N. V. Zoi, "0.75 ma, 400 ns rise time ltd stage," in *Digest of Technical Papers. 12th IEEE International Pulsed Power Conference. (Cat. No.99CH36358)*, vol. 2, pp. 955–958 vol.2, 1999.

[16] R. M. Gilgenbach, M. R. Gomez, J. C. Zier, W. W. Tang, D. M. French, Y. Y. Lau, M. G. Mazarakis, M. E. Cuneo, M. D. Johnston, B. V. Oliver, T. A. Mehlhorn, A. A. Kim, and V. A. Sinebryukhov, "MAIZE: a 1 MA LTD-Driven z-pinch at The University of Michigan," *AIP Conference Proceedings*, vol. 1088, no. 1, pp. 259–262, 2009.

[17] J. E. Bailey, T. Nagayama, G. P. Loisel, G. A. Rochau, C. Blancard, J. Colgan, P. Cosse, G. Faussurier, C. J. Fontes, F. Gilleron, I. Golovkin, S. B. Hansen, C. A. Iglesias, D. P. Kilcrease, J. J. MacFarlane, R. C. Mancini, S. N. Nahar, C. Orban, J.-C. Pain, A. K. Pradhan, M. Sherrill, and B. G. Wilson, "A higher-than-predicted measurement of iron opacity at solar interior temperatures," *Nature*, vol. 517, pp. 56–59, Jan 2015.

[18] G. A. Rochau, J. E. Bailey, R. E. Falcon, G. P. Loisel, T. Nagayama, R. C. Mancini, I. Hall, D. E. Winget, M. H. Montgomery, and D. A. Liedahl, "ZAPP: The Z Astrophysical Plasma Properties collaboration," *Phys. Plasmas*, vol. 21, no. 5, p. 056308, 2014.

[19] S. Root, J. P. Townsend, E. Davies, R. W. Lemke, D. E. Bliss, D. E. Fratanduono, R. G. Kraus, M. Millot, D. K. Spaulding, L. Shulenburger, S. T. Stewart, and S. B. Jacobsen, "The Principal Hugoniot of Forsterite to 950 GPa," *Geophysical Research Letters*, vol. 45, no. 9, pp. 3865–3872, 2018.

[20] M. R. Martin, R. W. Lemke, R. D. McBride, J. P. Davis, D. H. Dolan, M. D. Knudson, K. R. Cochrane, D. B. Sinars, I. C. Smith, M. Savage, W. A. Stygar, K. Killebrew, D. G. Flicker, and M. C. Herrmann, "Solid liner implosions on Z for producing multi-megabar, shockless compressions," *Phys. Plasmas*, vol. 19, no. 5, p. 056310, 2012.

[21] R. W. Lemke, D. H. Dolan, D. G. Dalton, J. L. Brown, K. Tomlinson, G. R. Robertson, M. D. Knudson, E. Harding, A. E. Mattsson, J. H. Carpenter, R. R. Drake, K. Cochrane, B. E. Blue, A. C. Robinson, and T. R. Mattsson, "Probing off-Hugoniot states in Ta, Cu, and Al to 1000 GPa compression with magnetically driven liner implosions," *J. Appl. Phys.*, vol. 119, no. 1, p. 015904, 2016.

[22] G. A. Rochau, J. E. Bailey, G. A. Chandler, G. Cooper, G. S. Dunham, P. W. Lake, R. J. Leeper, R. W. Lemke, T. A. Mehlhorn, A. Nikroo, K. J. Peterson, C. L. Ruiz, D. G. Schroen, S. A. Slutz, D. Steinman, W. A. Stygar, and W. Varnum, "High performance capsule implosions driven by the Z-pinch dynamic hohlraum," *Plasma Physics and Controlled Fusion*, vol. 49, no. 12B, p. B591, 2007.

[23] D. J. Ampleford, B. Jones, C. A. Jennings, S. B. Hansen, M. E. Cuneo, A. J. Harvey-Thompson, G. A. Rochau, C. A. Coverdale, A. R. Laspe, T. M. Flanagan, N. W. Moore, D. B. Sinars, D. C. Lamppa, E. C. Harding, J. W. Thornhill, J. L. Giuliani, Y.-K. Chong, J. P. Apruzese, A. L. Velikovich, A. Dasgupta, N. Ouart, W. A. Sygar, M. E. Savage, J. K. Moore, R. Focia, T. C. Wagoner, K. L. Killebrew, A. D. Edens, G. S. Dunham, M. C. Jones, P. W. Lake, D. S. Nielsen, M. Wu, A. L. Carlson, M. D. Kernahan, C. R.

Ball, R. D. Scharberg, T. D. Mulville, E. W. Breden, C. S. Speas, G. Olivas, M. A. Sullivan, A. J. York, D. W. Justus, J. C. Cisneros, T. Strizic, J. Reneker, M. Cleveland, M. P. Vigil, G. Robertson, D. Sandoval, C. Cox, A. J. Maurer, D. A. Graham, N. B. Huynh, S. Toledo, L. P. Molina, M. R. Lopez, F. W. Long, G. R. McKee, J. L. Porter, and M. C. Herrmann, "Contrasting physics in wire array z pinch sources of 1-20 keV emission on the Z facility," *Physics of Plasmas*, vol. 21, no. 5, p. 056708, 2014.

[24] S. A. Slutz, M. C. Herrmann, R. A. Vesey, A. B. Sefkow, D. B. Sinars, D. C. Rovang, K. J. Peterson, and M. E. Cuneo, "Pulsed-power-driven cylindrical liner implosions of laser preheated fuel magnetized with an axial field," *Physics of Plasmas*, vol. 17, no. 5, p. 056303, 2010.

[25] S. A. Slutz and R. A. Vesey, "High-Gain Magnetized Inertial Fusion," *Phys. Rev. Lett.*, vol. 108, p. 025003, Jan 2012.

[26] M. E. Cuneo, M. C. Herrmann, D. B. Sinars, S. A. Slutz, W. A. Stygar, R. A. Vesey, A. B. Sefkow, G. A. Rochau, G. A. Chandler, J. E. Bailey, J. L. Porter, R. D. McBride, D. C. Rovang, M. G. Mazarakis, E. P. Yu, D. C. Lamppa, K. J. Peterson, C. Nakhleh, S. B. Hansen, A. J. Lopez, M. E. Savage, C. A. Jennings, M. R. Martin, R. W. Lemke, B. W. Atherton, I. C. Smith, P. K. Rambo, M. Jones, M. R. Lopez, P. J. Christenson, M. A. Sweeney, B. Jones, L. A. McPherson, E. Harding, M. R. Gomez, P. F. Knapp, T. J. Awe, R. J. Leeper, C. L. Ruiz, G. W. Cooper, K. D. Hahn, J. McKenney, A. C. Owen, G. R. McKee, G. T. Leifeste, D. J. Ampleford, E. M. Waisman, A. Harvey-Thompson, R. J. Kaye, M. H. Hess, S. E. Rosenthal, and M. K. Matzen, "Magnetically Driven Implosions for Inertial Confinement Fusion at Sandia National Laboratories," *IEEE Transactions on Plasma Science*, vol. 40, no. 12, pp. 3222–3245, 2012.

[27] M. R. Gomez, S. A. Slutz, A. B. Sefkow, D. B. Sinars, K. D. Hahn, S. B. Hansen, E. C. Harding, P. F. Knapp, P. F. Schmit, C. A. Jennings, T. J. Awe, M. Geissel, D. C. Rovang, G. A. Chandler, G. W. Cooper, M. E. Cuneo, A. J. Harvey-Thompson, M. C. Herrmann, M. H. Hess, O. Johns, D. C. Lamppa, M. R. Martin, R. D. McBride, K. J. Peterson, J. L. Porter, G. K. Robertson, G. A. Rochau, C. L. Ruiz, M. E. Savage, I. C. Smith, W. A. Stygar, and R. A. Vesey, "Experimental Demonstration of Fusion-Relevant Conditions in Magnetized Liner Inertial Fusion," *Phys. Rev. Lett.*, vol. 113, p. 155003, Oct 2014.

[28] O. A. Hurricane, D. A. Callahan, D. T. Casey, P. M. Celliers, C. Cerjan, E. L. Dewald, T. R. Dittrich, T. Döppner, D. E. Hinkel, L. F. B. Hopkins, J. L. Kline, S. Le Pape, T. Ma, A. G. MacPhee, J. L. Milovich, A. Pak, H.-S. Park, P. K. Patel, B. A. Remington, J. D. Salmonson, P. T. Springer, and R. Tommasini, "Fuel gain exceeding unity in an inertially confined fusion implosion," *Nature*, vol. 506, pp. 343–348, Feb 2014.

[29] S. A. Slutz, M. R. Gomez, S. B. Hansen, E. C. Harding, B. T. Hutsel, P. F. Knapp, D. C. Lamppa, T. J. Awe, D. J. Ampleford, D. E. Bliss, G. A. Chandler, M. E. Cuneo, M. Geissel, M. E. Glinsky, A. J. Harvey-Thompson, M. H. Hess, C. A. Jennings, B. Jones, G. R. Laity, M. R. Martin, K. J. Peterson, J. L. Porter, P. K. Rambo, G. A. Rochau, C. L. Ruiz, M. E. Savage, J. Schwarz, P. F. Schmit, G. Shipley, D. B. Sinars, I. C. Smith,

R. A. Vesey, and M. R. Weis, "Enhancing performance of magnetized liner inertial fusion at the z facility," *Physics of Plasmas*, vol. 25, no. 11, p. 112706, 2018.

[30] F. F. Chen, *Introduction to Plasma Physics*. Springer US, 1995.

[31] D. R. Nicholson, *Introduction to plasma theory*. Reprint Edition. Kriegre Publishing Company, 1982, c1983.

[32] U. Shumlak and C. W. Hartman, "Sheared flow stabilization of the $m = 1$ kink mode in Z pinches," *Phys. Rev. Lett.*, vol. 75, pp. 3285–3288, Oct 1995.

[33] P. Zhang, Y. Y. Lau, I. M. Rittersdorf, M. R. Weis, R. M. Gilgenbach, D. Chalenski, and S. A. Slutz, "Effects of magnetic shear on magneto-Rayleigh-Taylor instability," *Physics of Plasmas*, vol. 19, no. 2, p. 022703, 2012.

[34] F. L. Cochran and A. E. Robson, "Viscoresistive stabilization of the z pinch," *Physics of Fluids B: Plasma Physics*, vol. 5, no. 8, pp. 2905–2908, 1993.

[35] A. B. Bud'ko, Y. P. Kravchenko, and M. A. Liberman, "Stabilization of sausage and kink instability modes of a plasma pinch by radial oscillations," *Physics of Plasmas*, vol. 2, no. 3, pp. 792–802, 1995.

[36] L. F. Wanex, V. I. Sotnikov, and J. N. Leboeuf, "Linear analysis of magnetic and flow shear stabilization of z-pinch instabilities," *Physics of Plasmas*, vol. 12, no. 4, p. 042101, 2005.

[37] A. L. Velikovich, F. L. Cochran, J. Davis, and Y. K. Chong, "Stabilized radiative z-pinch loads with tailored density profiles," *Physics of Plasmas*, vol. 5, no. 9, pp. 3377–3388, 1998.

[38] A. L. Velikovich and J. Davis, "Implosions, equilibria, and stability of rotating, radiating z-pinch plasmas," *Physics of Plasmas*, vol. 2, no. 12, pp. 4513–4520, 1995.

[39] E. P. Yu, T. J. Awe, K. R. Cochrane, K. C. Yates, T. M. Hutchinson, K. J. Peterson, and B. S. Bauer, "Use of hydrodynamic theory to estimate electrical current redistribution in metals," *Physics of Plasmas*, vol. 27, no. 5, p. 052703, 2020.

[40] Rayleigh, "Investigation of the character of the equilibrium of an incompressible heavy fluid of variable density," *Proceedings of the London Mathematical Society*, vol. s1-14, no. 1, pp. 170–177, 1882.

[41] G. I. Taylor, "The instability of liquid surfaces when accelerated in a direction perpendicular to their planes," *Proceedings of the Royal Society of London. Series A. Mathematical and Physical Sciences*, vol. 201, no. 1065, pp. 192–196, 1950.

[42] C.-Y. Wang and R. A. Chevalier, "Instabilities and clumping in type ia supernova remnants," *The Astrophysical Journal*, vol. 549, pp. 1119–1134, mar 2001.

[43] S. Chandrasekhar, *Hydrodynamic and hydromagnetic stability*. 1961.

[44] E. G. Harris, "Rayleigh-Taylor Instabilities of a Collapsing Cylindrical Shell in a Magnetic Field," *Phys. Fluids*, vol. 5, no. 9, pp. 1057–1062, 1962.

[45] Y. Y. Lau, J. C. Zier, I. M. Rittersdorf, M. R. Weis, and R. M. Gilgenbach, "Anisotropy and feedthrough in magneto-rayleigh-taylor instability," *Phys. Rev. E*, vol. 83, p. 066405, Jun 2011.

[46] M. R. Weis, P. Zhang, Y. Y. Lau, P. F. Schmit, K. J. Peterson, M. Hess, and R. M. Gilgenbach, "Coupling of sausage, kink, and magneto-Rayleigh-Taylor instabilities in a cylindrical liner," *Physics of Plasmas*, vol. 22, no. 3, p. 032706, 2015.

[47] J. D. Pecover and J. P. Chittenden, "Instability growth for magnetized liner inertial fusion seeded by electro-thermal, electro-choric, and material strength effects," *Phys. Plasmas*, vol. 22, no. 10, p. 102701, 2015.

[48] K. J. Peterson, T. J. Awe, E. P. Yu, D. B. Sinars, E. S. Field, M. E. Cuneo, M. C. Herrmann, M. Savage, D. Schroen, K. Tomlinson, and C. Nakhleh, "Electrothermal Instability Mitigation by Using Thick Dielectric Coatings on Magnetically Imploded Conductors," *Phys. Rev. Lett.*, vol. 112, p. 135002, Apr 2014.

[49] T. J. Awe, K. J. Peterson, E. P. Yu, R. D. McBride, D. B. Sinars, M. R. Gomez, C. A. Jennings, M. R. Martin, S. E. Rosenthal, D. G. Schroen, A. B. Sefkow, S. A. Slutz, K. Tomlinson, and R. A. Vesey, "Experimental Demonstration of the Stabilizing Effect of Dielectric Coatings on Magnetically Accelerated Imploding Metallic Liners," *Phys. Rev. Lett.*, vol. 116, p. 065001, Feb 2016.

[50] A. M. Steiner, P. C. Campbell, D. A. Yager-Elorriaga, K. R. Cochrane, T. R. Mattsson, N. M. Jordan, R. D. McBride, Y. Y. Lau, and R. M. Gilgenbach, "The electro-thermal stability of tantalum relative to aluminum and titanium in cylindrical liner ablation experiments at 550 ka," *Physics of Plasmas*, vol. 25, no. 3, p. 032701, 2018.

[51] M. Evans, M. B. Adams, P. C. Campbell, N. M. Jordan, S. M. Miller, N. B. Ramey, R. V. Shapovalov, J. Young, I. West-Abdallah, J. M. Woolstrum, R. D. McBride, and P.-A. Gourdain, "Reduction of ablated surface expansion in pulsed-power-driven experiments using an aerosol dielectric coating," *Physics of Plasmas*, vol. 26, no. 7, p. 070704, 2019.

[52] P. F. Schmit, A. L. Velikovich, R. D. McBride, and G. K. Robertson, "Controlling Rayleigh-Taylor Instabilities in Magnetically Driven Solid Metal Shells by Means of a Dynamic Screw Pinch," *Phys. Rev. Lett.*, vol. 117, p. 205001, Nov 2016.

[53] S. A. Sorokin, "Gas-puff liner implosion in the configuration with helical current return rods," *Plasma Physics Reports*, vol. 39, pp. 139–143, Feb 2013.

[54] P.-A. Gourdain, M. B. Adams, J. R. Davies, and C. E. Seyler, "Axial magnetic field injection in magnetized liner inertial fusion," *Phys. Plasmas*, vol. 24, no. 10, p. 102712, 2017.

[55] D. A. Yager-Elorriaga, P. Zhang, A. M. Steiner, N. M. Jordan, P. C. Campbell, Y. Y. Lau, and R. M. Gilgenbach, "Discrete helical modes in imploding and exploding cylindrical, magnetized liners," *Phys. Plasmas*, vol. 23, no. 12, p. 124502, 2016.

[56] D. A. Yager-Elorriaga, Y. Y. Lau, P. Zhang, P. C. Campbell, A. M. Steiner, N. M. Jordan, R. D. McBride, and R. M. Gilgenbach, "Evolution of sausage and helical modes in magnetized thin-foil cylindrical liners driven by a Z-pinch," *Physics of Plasmas*, vol. 25, no. 5, p. 056307, 2018.

[57] E. Ott, "Nonlinear evolution of the Rayleigh-Taylor instability of a thin layer," *Phys. Rev. Lett.*, vol. 29, pp. 1429–1432, Nov 1972.

[58] J. W. Jacobs and I. Catton, "Three-dimensional rayleigh-taylor instability part 1. weakly nonlinear theory," *Journal of Fluid Mechanics*, vol. 187, p. 329–352, 1988.

[59] W. H. Liu, L. F. Wang, W. H. Ye, and X. T. He, "Nonlinear saturation amplitudes in classical Rayleigh-Taylor instability at arbitrary Atwood numbers," *Physics of Plasmas*, vol. 19, no. 4, p. 042705, 2012.

[60] L. F. Wang, J. F. Wu, W. H. Ye, W. Y. Zhang, and X. T. He, "Weakly nonlinear incompressible Rayleigh-Taylor instability growth at cylindrically convergent interfaces," *Physics of Plasmas*, vol. 20, no. 4, p. 042708, 2013.

[61] D. E. Ruiz, "On a variational formulation of the weakly nonlinear magnetic rayleigh–taylor instability," *Physics of Plasmas*, vol. 27, no. 2, p. 022121, 2020.

[62] R. D. McBride, S. A. Slutz, C. A. Jennings, D. B. Sinars, M. E. Cuneo, M. C. Herrmann, R. W. Lemke, M. R. Martin, R. A. Vesey, K. J. Peterson, A. B. Sefkow, C. Nakhleh, B. E. Blue, K. Killebrew, D. Schroen, T. J. Rogers, A. Laspe, M. R. Lopez, I. C. Smith, B. W. Atherton, M. Savage, W. A. Stygar, and J. L. Porter, "Penetrating radiography of imploding and stagnating beryllium liners on the Z accelerator," *Phys. Rev. Lett.*, vol. 109, p. 135004, Sep 2012.

[63] P. C. Campbell, T. M. Jones, J. M. Woolstrum, N. M. Jordan, P. F. Schmit, J. B. Greenly, W. M. Potter, E. S. Lavine, B. R. Kusse, D. A. Hammer, and R. D. McBride, "Stabilization of liner implosions via a dynamic screw pinch," *Phys. Rev. Lett.*, vol. 125, p. 035001, Jul 2020.

[64] J. M. Woolstrum, D. A. Yager-Elorriaga, P. C. Campbell, N. M. Jordan, C. E. Seyler, and R. D. McBride, "Extended magnetohydrodynamics simulations of thin-foil z-pinch implosions with comparison to experiments," *Physics of Plasmas*, vol. 27, no. 9, p. 092705, 2020.

[65] T. J. Awe, R. D. McBride, C. A. Jennings, D. C. Lamppa, M. R. Martin, D. C. Rovang, S. A. Slutz, M. E. Cuneo, A. C. Owen, D. B. Sinars, K. Tomlinson, M. R. Gomez, S. B. Hansen, M. C. Herrmann, J. L. McKenney, C. Nakhleh, G. K. Robertson, G. A. Rochau, M. E. Savage, D. G. Schroen, and W. A. Stygar, "Observations of Modified Three-Dimensional Instability Structure for Imploding z-Pinch Liners that are Premagnetized with an Axial Field," *Phys. Rev. Lett.*, vol. 111, p. 235005, Dec 2013.

[66] T. A. Shelkovenko and D. A. Chalenski and K. M. Chandler and J. D. Douglass and J. B. Greenly and D. A. Hammer and B. R. Kusse and R. D. McBride and S. A. Pikuz, "Diagnostics on the cobra pulsed power generator," *Review of Scientific Instruments*, vol. 77, no. 10, p. 10F521, 2006.

[67] G. A. Shipley, C. A. Jennings, and P. F. Schmit, "Design of dynamic screw pinch experiments for magnetized liner inertial fusion," *Physics of Plasmas*, vol. 26, no. 10, p. 102702, 2019.

[68] R. D. McBride, M. R. Martin, R. W. Lemke, J. B. Greenly, C. A. Jennings, D. C. Rovang, D. B. Sinars, M. E. Cuneo, M. C. Herrmann, S. A. Slutz, C. W. Nakhleh, D. D. Ryutov, J.-P. Davis, D. G. Flicker, B. E. Blue, K. Tomlinson, D. Schroen, R. M. Stamm, G. E. Smith, J. K. Moore, T. J. Rogers, G. K. Robertson, R. J. Kamm, I. C. Smith, M. Savage, W. A. Stygar, G. A. Rochau, M. Jones, M. R. Lopez, J. L. Porter, and M. K. Matzen, "Beryllium liner implosion experiments on the z accelerator in preparation for magnetized liner inertial fusion," *Physics of Plasmas*, vol. 20, no. 5, p. 056309, 2013.

[69] D. A. Yager-Elorriaga, A. M. Steiner, S. G. Patel, N. M. Jordan, Y. Y. Lau, and R. M. Gilgenbach, "Technique for fabrication of ultrathin foils in cylindrical geometry for liner-plasma implosion experiments with sub-megaampere currents," *Review of Scientific Instruments*, vol. 86, no. 11, p. 113506, 2015.

[70] J. C. Zier, R. M. Gilgenbach, D. A. Chalenski, Y. Y. Lau, D. M. French, M. R. Gomez, S. G. Patel, I. M. Rittersdorf, A. M. Steiner, M. Weis, P. Zhang, M. Mazarakis, M. E. Cuneo, and M. Lopez, "Magneto-Rayleigh-Taylor experiments on a MegaAmpere linear transformer driver," *Phys. Plasmas*, vol. 19, no. 3, p. 032701, 2012.

[71] M. R. Weis, *Magneto-Rayleigh-Taylor Instability: Theory and Simulation in Planar and Cylindrical Pulsed Power Targets*. PhD thesis, University of Michigan, 2015.

[72] R. H. Huddlestone and S. L. Leonard, *Plasma Diagnostic Techniques Pure and Applied Physics 21*. New York, Academic Press, 1965.

[73] A. Gerrard and J. M. Burch, *Introduction to Matrix Methods in Optics*. Dover Publishers, reprint edition ed., 2012.

[74] S. M. Miller, S. A. Slutz, S. N. Bland, S. R. Klein, P. C. Campbell, J. M. Woolstrum, C. C. Kuranz, M. R. Gomez, N. M. Jordan, and R. D. McBride, "A pulsed-power implementation of "laser gate" for increasing laser energy coupling and fusion yield in magnetized liner inertial fusion (maglif)," *Review of Scientific Instruments*, vol. 91, no. 6, p. 063507, 2020.

[75] S. N. Bland, D. J. Ampleford, S. C. Bott, S. V. Lebedev, J. B. A. Palmer, S. A. Pikuz, and T. A. Shelkovenko, "Extreme ultraviolet imaging of wire array z-pinch experiments," *Review of Scientific Instruments*, vol. 75, pp. 3941–3943, Oct 2004.

[76] J. Greenly, M. Martin, I. Blesener, D. Chalenski, P. Knapp, and R. McBride, "The Role of Flux Advection in the Development of the Ablation Streams and Precursors of Wire Array Z-pinches," *AIP Conference Proceedings*, vol. 1088, no. 1, pp. 53–56, 2009.

[77] R. S. Cohen, L. Spitzer, and P. M. Routly, "The electrical conductivity of an ionized gas," *Phys. Rev.*, vol. 80, pp. 230–238, Oct 1950.

[78] L. Spitzer and R. Härm, "Transport phenomena in a completely ionized gas," *Phys. Rev.*, vol. 89, pp. 977–981, Mar 1953.

[79] Y. T. Lee and R. M. More, "An electron conductivity model for dense plasmas," *The Physics of Fluids*, vol. 27, no. 5, pp. 1273–1286, 1984.

[80] M. Desjarlais, "Practical improvements to the lee-more conductivity near the metal-insulator transition," *Contributions to Plasma Physics*, vol. 41, no. 2-3, pp. 267–270, 2001.

[81] M. P. Desjarlais, J. D. Kress, and L. A. Collins, "Electrical conductivity for warm, dense aluminum plasmas and liquids," *Phys. Rev. E*, vol. 66, p. 025401, Aug 2002.

[82] C. E. Seyler and M. R. Martin, "Relaxation model for extended magnetohydrodynamics: Comparison to magnetohydrodynamics for dense z-pinches," *Physics of Plasmas*, vol. 18, no. 1, p. 012703, 2011.

[83] A. Kramida, Yu. Ralchenko, J. Reader, and and NIST ASD Team. NIST Atomic Spectra Database (ver. 5.7.1), [Online]. Available: `https://physics.nist.gov/asd` [2020, June 11]. National Institute of Standards and Technology, Gaithersburg, MD., 2019.

[84] L. Atoyan, D. A. Hammer, B. R. Kusse, T. Byvank, A. D. Cahill, J. B. Greenly, S. A. Pikuz, and T. A. Shelkovenko, "Helical plasma striations in liners in the presence of an external axial magnetic field," *Physics of Plasmas*, vol. 23, no. 2, p. 022708, 2016.

[85] D. D. Ryutov and M. A. Dorf, "Evolution of helical perturbations in a thin-shell model of an imploding liner," *Physics of Plasmas*, vol. 21, no. 11, p. 112704, 2014.

[86] D. B. Sinars, S. A. Slutz, M. C. Herrmann, R. D. McBride, M. E. Cuneo, K. J. Peterson, R. A. Vesey, C. Nakhleh, B. E. Blue, K. Killebrew, D. Schroen, K. Tomlinson, A. D. Edens, M. R. Lopez, I. C. Smith, J. Shores, V. Bigman, G. R. Bennett, B. W. Atherton, M. Savage, W. A. Stygar, G. T. Leifeste, and J. L. Porter, "Measurements of Magneto-Rayleigh-Taylor Instability Growth during the Implosion of Initially Solid Al Tubes Driven by the 20-MA, 100-ns Z Facility," *Phys. Rev. Lett.*, vol. 105, p. 185001, Oct 2010.

[87] G. C. Burdiak, S. V. Lebedev, F. Suzuki-Vidal, G. F. Swadling, S. N. Bland, N. Niasse, L. Suttle, M. Bennet, J. Hare, M. Weinwurm, and et al., "Cylindrical liner z-pinch experiments for fusion research and high-energy-density physics," *Journal of Plasma Physics*, vol. 81, no. 3, p. 365810301, 2015.

[88] M. G. Haines, "The Inverse Skin Effect," *Proceedings of the Physical Society*, vol. 74, no. 5, p. 576, 1959.

[89] J. Greenly, C. Seyler, and X. Zhao, "Pulsed-power driven reconnection and the inverse skin effect," *Paper JP8 97, Bull. Am. Phys. Soc.*, vol. 59, p. 133, 2014.

[90] T. J. Awe, E. P. Yu, K. C. Yates, W. G. Yelton, B. S. Bauer, T. M. Hutchinson, S. Fuelling, and B. B. Mckenzie, "On the evolution from micrometer-scale inhomogeneity to global overheated structure during the intense joule heating of a z-pinch rod," *IEEE Transactions on Plasma Science*, vol. 45, no. 4, pp. 584–589, 2017.

[91] R. Doron, D. Mikitchuk, C. Stollberg, G. Rosenzweig, E. Stambulchik, E. Kroupp, Y. Maron, and D. A. Hammer, "Determination of magnetic fields based on the Zeeman effect in regimes inaccessible by Zeeman-splitting spectroscopy," *High Energy Density Phys.*, vol. 10, pp. 56–60, 2014.

[92] A. A. Kim, M. G. Mazarakis, V. A. Sinebryukhov, B. M. Kovalchuk, V. A. Visir, S. N. Volkov, F. Bayol, A. N. Bastrikov, V. G. Durakov, S. V. Frolov, V. M. Alexeenko, D. H. McDaniel, W. E. Fowler, K. LeChien, C. Olson, W. A. Stygar, K. W. Struve, J. Porter, and R. M. Gilgenbach, "Development and tests of fast 1-MA linear transformer driver stages," *Phys. Rev. ST Accel. Beams*, vol. 12, p. 050402, May 2009.

[93] M. G. Mazarakis, W. E. Fowler, K. L. LeChien, F. W. Long, M. K. Matzen, D. H. McDaniel, R. G. McKee, C. L. Olson, J. L. Porter, S. T. Rogowski, K. W. Struve, W. A. Stygar, J. R. Woodworth, A. A. Kim, V. A. Sinebryukhov, R. M. Gilgenbach, M. R. Gomez, D. M. French, Y. Y. Lau, J. C. Zier, D. M. VanDevalde, R. A. Sharpe, and K. Ward, "High-current linear transformer driver development at Sandia National Laboratories," *IEEE Transactions on Plasma Science*, vol. 38, no. 4, pp. 704–713, 2010.